SPINTRONICS IN CLUSTER-ASSEMBLED NANOSTRUCTURES

Simón Oyarzún

N° d'ordre 166-2013 Année 2013

THESE DE L'UNIVERSITE DE LYON

Délivrée par

L'UNIVERSITE CLAUDE BERNARD LYON 1

ECOLE DOCTORALE DE PHYSIQUE ET ASTROPHYSIQUE

DIPLOME DE DOCTORAT
(arrêté du 7 aout 2006)

soutenue publiquement le 15 octobre 2013

par

Simón OYARZÚN MEDINA

SPINTRONICS IN CLUSTER-ASSEMBLED NANOSTRUCTURES

Directrice de Thèse: Véronique Dupuis
Co-directeur de Thèse: Matthias Hillenkamp

JURY

Mme. Catherine Journet-Gautier	Présidente du Jury
M. Wolfgang Harbich	Examinateur
M. Robert Morel	Rapporteur
M. Julian Carrey	Rapporteur
M. Matthias Hillenkamp	Co-directeur de Thèse
Mme. Véronique Dupuis	Directrice de Thèse

UNIVERSITE CLAUDE BERNARD - LYON 1

Président de l'Université	**M. François-Noël GILLY**
Vice-président du Conseil d'Administration	M. le Professeur Hamda BEN HADID
Vice-président du Conseil des Etudes et de la Vie Universitaire	M. le Professeur Philippe LALLE
Vice-président du Conseil Scientifique	M. le Professeur Germain GILLET
Secrétaire Général	M. Alain HELLEU

COMPOSANTES SANTE

Faculté de Médecine Lyon Est – Claude Bernard	Directeur : M. le Professeur J. ETIENNE
Faculté de Médecine et de Maïeutique Lyon Sud – Charles Mérieux	Administrateur provisoire : M. le Professeur G. KIRKORIAN
UFR d'Odontologie	Directeur : M. le Professeur D. BOURGEOIS
Institut des Sciences Pharmaceutiques et Biologiques	Directeur : Mme la Professeure C. VINCIGUERRA.
Institut des Sciences et Techniques de la Réadaptation	Directeur : M. le Professeur Y. MATILLON
Département de formation et Centre de Recherche en Biologie Humaine	Directeur : M. le Professeur P. FARGE

COMPOSANTES ET DEPARTEMENTS DE SCIENCES ET TECHNOLOGIE

Faculté des Sciences et Technologies	Directeur : M. le Professeur F. De MARCHI
Département Biologie	Directeur : M. le Professeur F. FLEURY
Département Chimie Biochimie	Directeur : Mme le Professeur H. PARROT
Département GEP	Directeur : M. N. SIAUVE
Département Informatique	Directeur : M. le Professeur S. AKKOUCHE
Département Mathématiques	Directeur : M. le Professeur A. GOLDMAN
Département Mécanique	Directeur : M. le Professeur H. BEN HADID
Département Physique	Directeur : Mme S. FLECK
Département Sciences de la Terre	Directeur : Mme la Professeure I. DANIEL
UFR Sciences et Techniques des Activités Physiques et Sportives	Directeur : M. C. COLLIGNON
Observatoire de Lyon	Directeur : M. B. GUIDERDONI
Polytech Lyon	Directeur : M. P. FOURNIER
Ecole Supérieure de Chimie Physique Electronique	Directeur : M. G. PIGNAULT
Institut Universitaire de Technologie de Lyon 1	Directeur : M. C. VITON
Institut Universitaire de Formation des Maîtres	Directeur : M. R. BERNARD
Institut de Science Financière et d'Assurances	Directeur : Mme la Professeure V. MAUME-DESCHAMPS

ACKNOWLEDGMENTS

After three years of hard work I would like to express my acknowledgment to everyone that was involved in this thesis by his or her support, scientific and technical contribution.

I want to thank to all members of the jury, starting by Catherine Journet-Gautier for having accepted preside the commission, to Julian Carrey, Robert Morel and Wolfgang Harbich for having read this thesis and their important remarks and valuable criticism doing possible this final version.

In the beginning the first step was to improve and make that the *source* worked. This process would not have been possible without the help and dedication of the technical and scientific staff, for that I want to thank to Olivier Boisron, Clément Albin, Guillaume Suteau, Alexis Mosset, Emmanuel Cottancin and Christian Clavier.

I thank to the current and old ph.d students: Dimitri Hapiuk, Lucas Piot, José Flores, Abraao Torres, Artur Domingues and Arnaud Hillion to make this stay much more friendly. To Sabastien Linas and Chandra Shekhar Pati Tripathi to share a cup coffee each morning. To the administrative staff; Christelle Macheboeuf, Delphine Kervella and Geneviéve Carasco for their invaluable help and availability.

I would like to thank specially to all members of the Groupe Nanostructures magnétiques, to Julliette Tuaillon-Combes, Laurent Bardotti and Estela Bernstein for their warm welcome. To Alexandre and Florent for the fruitful discussions and advices. Good luck Ghassan Khadra with your thesis. I would to like express my gratitude to my two supervisors Véronique Dupuis and Matthias Hillenkamp. Véronique worried of me from my arrival and at the end of the thesis she pulled me out of the laboratory in order to write and show the physics behind this work. To Matthias and his family for their warm welcome and support, and for the many discussions and advices to make me a better scientific.

I want to thank to my family Julio, Alicia, Leandro and Natalia that from to the distance always were present.

To Heidy where now, we appear two of us holding the hands of Mariana...

TITRE : SPINTRONIQUE DANS DES ASSEMBLÉES DE NANOPARTICULES

RÉSUMÉ : Dans les dernières années, la miniaturisation progressive des dispositifs de stockage magnétique a rendu nécessaire de comprendre comment les propriétés physiques sont modifiées par rapport à l'état massif lorsque les dimensions sont réduites à l'échelle nanométrique. Pour cette raison, une méthode précise de préparation et caractérisation de nanostructures est extrêmement importante. Ce travail se concentre sur les propriétés magnétiques et de transport de nanoparticules de cobalt incorporées dans des matrices de cuivre. Notre dispositif experimental nous permet de contrôler indépendamment la taille moyenne des agrégats, la concentration et la composition chimique. La production des agrégats de cobalt est basée sur la pulvérisation cathodique et l'agrégation dans la phase gazeuse. Cette source permet de produire des agrégats dans une large gamme de taille, de un à plusieurs milliers d'atomes. Dans un premier temps, nous avons étudié le rôle des interactions entre particules dans les propriétés de transport et magnétiques, en augmentant la concentration des nanoparticules de cobalt (à partir de 0.5 % à 2.5 % et 5 %). Nos résultats démontrent les précautions nécessaires et constituent une base solide pour de futures études sur les propriétés spintroniques des systèmes granulaires. Dans le but de décrire les propriétés magnétiques intrinsèques d'agrégats, nous avons préparé des échantillons fortement dilués ($\leqslant$0.5%) pour différents diamètres d'agrégats de 1.9 nm à 5.5 nm. Nous avons constaté que les propriétés magnétiques sont dépendantes de la taille. L'utilisation d'une caractérisation magnètique complète, sensible à la variation de l'anisotropie magnétique efficace, nous montre que l'anisotropie magnétique est dominée par les contributions de la surface ou de la forme des nanoparticules.

MOT-CLÉS : nanoparticule, superparamagnétisme, anisotropie magnétique, surface, forme, spintronique, transport, magnétorésistance, concentration, interactions.

DISCIPLINE : Physique

INTITULÉ ET ADRESSE DU LABORATOIRE:

Institut Lumière Matière
UMR 5306 Université Lyon 1-CNRS
Bât. Léon Brillouin, 6 rue Ada Byron
F-69622 Villeurbanne cedex

TITLE : SPINTRONICS IN CLUSTER-ASSEMBLED NANOSTRUCTURES

ABSTRACT: In the last years, the progressive miniaturization of magnetic storage devices has imposed the necessity to understand how the physical properties are modified with respect to the bulk when the dimensions are reduced at the nanometric scale. For this reason an accurate method of preparation and characterization of nanostructures is extremely important. This work focuses on the magnetic and transport properties of cluster-assembled nanostructures, namely cobalt nanoparticles embedded in copper matrices. Our setup allows us to independently control the mean cluster size, the concentration and the chemical composition. The cobalt cluster production is based on magnetron sputtering and gas phase aggregation. The performance of the source permits a wide range of cluster masses, from one to several thousand atoms. As a first step we studied the role of inter-particle interactions in the transport and magnetic properties, increasing the cobalt nanoparticle concentration (from 0.5% to 2.5% and 5%). Our results demonstrate the necessary precautions and constitute a solid basis for further studies of the spintronic properties of granular systems. Finally, in order to describe the intrinsic magnetic properties of cluster-assembled nanostructures, we prepared strongly diluted samples ($\leqslant$0.5%) for different cluster sizes from 1.9 nm to 5.5 nm. We found that the magnetic properties are size-dependent. Using a complete magnetic characterization, sensitive to the change in the effective magnetic anisotropy, we show that the magnetic anisotropy is dominated by the contributions of the surface or of the shape of the nanoparticles.

KEY WORDS : nanoparticle, superparamagnetism, magnetic anisotropy, surface, shape, spintronics, transport, magnetoresistance, concentration, interactions.

DISCIPLINE : Physics

NAME AND ADDRESS OF THE LABORATORY:

Institut Lumière Matière
UMR 5306 Université Lyon 1-CNRS
Bât. Léon Brillouin, 6 rue Ada Byron
F-69622 Villeurbanne cedex

Table of Contents

List of Tables

List of Figures

Introduction

Magnetic properties are modified with respect to the bulk when the dimensions of the structures are reduced to the nanometer scale. The resulting magnetic behavior is due to the competition of different magnetic energies and the scale length associated to the structure. Magnetic nanostructures whose dimensions are in the nanometric scale have interesting properties and their potential applications in high density magnetic recording data depend strongly on the particles size. For example, reducing the cluster size the fraction of the atoms at the surface increases and the influence in the magnetic properties becomes more and more important. The effect of the surface will be more important for small particles and almost negligible for bigger ones.

On the one hand granular systems correspond to magnetic nanoparticles embedded in non magnetic matrices nowadays offer the possibility to vary the physical properties via different parameters such as the mean cluster size or the cluster concentration. Spintronics in the other hand has become an important research subject for fundamental studies and different applications have been developed such as magnetic recording head in hard drives using GMR effect and the central idea is to study and use the interaction between the conduction electrons with the localized magnetic moments by spin-dependent scattering.

In order to extract the magnetic information from the nanoparticles it is mandatory to perform a complete magnetic characterization whose results must be contrasted with different experimental techniques allowing to have a solid base without ambiguity and thus go further to study for example the influence of the cluster surface, shape or concentration on the magnetic properties.

chapter I

Experimental setup

I.1 INTRODUCTION

The sample production is oriented to do fundamental studies in magnetism, optics and electrical transport properties in granular systems. In particular the main idea is to understand how these physical properties are modified with respect to the bulk when the dimensions of the structure are reduced at nanometric scale. To achieve this goal it is imperative to work with well defined samples, with independent control over the cluster size, concentration and chemical composition.

To face this challenge we have used an experimental setup [36], where the cluster production offers the possibility to vary the cluster size from 1 atom up to around 10000 atoms corresponding to ∼6 nm. The cluster source produces an intense and continuous beam of charged clusters that can be guided and filtered using electric fields. Together with the wide range of cluster sizes produced, this setup offers very narrow size distributions, which represents an important advantage to study size effects in physical properties.

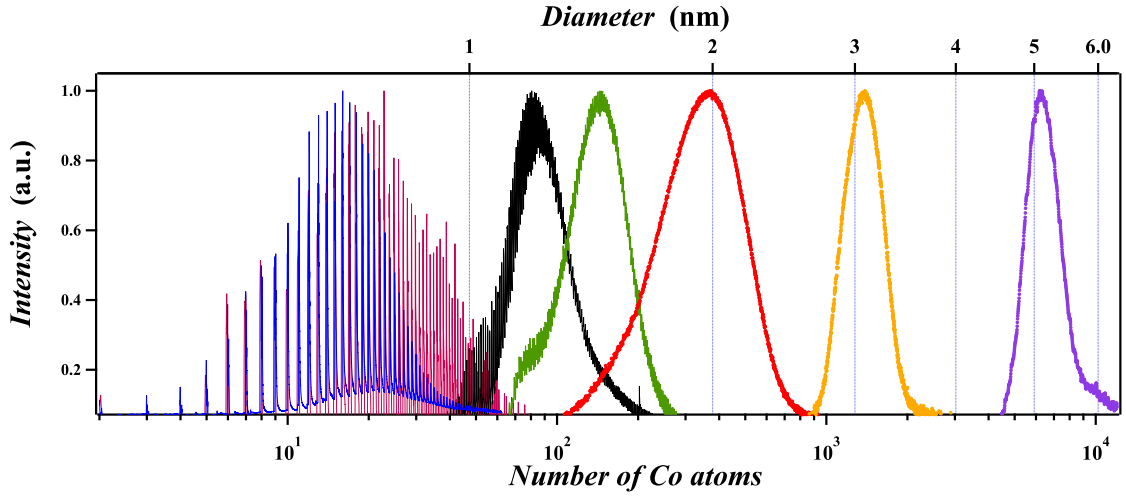

FIG. 1: *Mass spectra of cobalt clusters at different source conditions. The cluster source offers the possibility to vary the cluster size from 1 atom up to around 10000 atoms corresponding to ∼6 nm.*

The sample preparation is based on the simultaneous deposition of the cluster beam and metallic, insulating or semiconducting matrices, in which the nanoparticles are embedded. By varying the relative flux of cluster and matrix the concentration of the cluster will be controlled.

This setup offers the possibility to characterize in real-time the cluster production. The cluster size is determined using in-situ time of flight mass spectrometry

(TOF-MS), in order to adjust the set of parameters in the source to get the desired cluster size. Additionally this setup has several detectors in order to measure the ion current at different points in order to optimize the ion beam in each stage.

I.2 EXPERIMENTAL SETUP

This setup is composed of four main parts: the cluster source, the transfer region, the TOF-MS and the deposition chamber, displayed in the **Fig. 2**.

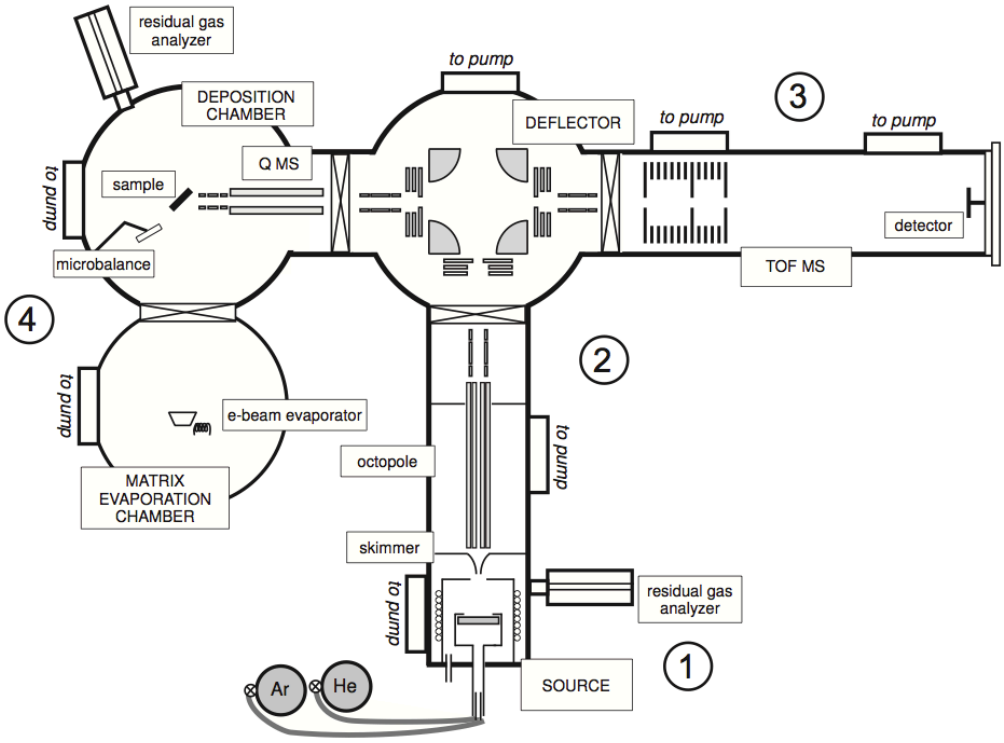

FIG. 2: *Schematic overview of the experimental setup composed of four main parts: the cluster source (1), the transfer region (2), the TOF-MS (3) and the deposition chamber (4).*

The cluster production is based on magnetron sputtering and by tuning a set of parameters in the source such as the gas flow or discharge power the cluster size is controlled. A continuous and intense ion beam is obtained in the aggregation chamber. At the next stage, the transfer region, the beam passes through an electrostatic lens composed of three cylindrical electrodes or an octupole ion guide depending on the desired cluster size. The cluster beam then enters the deviator and an electrostatic

quadrupole deflects the ion beam in 90° to the right side and the cluster size is determined by TOF-MS. Turning the ion beam to the left side the clusters arrive at the deposition chamber at the same time that the atomic beam for the matrix. In order to evaporate the material used for the matrix, an electron gun is placed below the deposition chamber. Finally the sample is prepared when all set of parameters involved in the deposition process are optimized.

I.2.1 Cluster production

The Cluster source was built following the setup developed by Haberland *et al.* [32], using a commercial 2 inch cylindrical magnetron. The cluster production is based on the target vaporization by sputtering using energetic ions in an inert gas atmosphere. The ejected atoms from the target are cooled via successive collisions with the inert gas and the aggregation process starts by single-atom addition. The cluster size will depend on the number of collisions between smaller clusters before exiting from the aggregation region, which is controlled for example by the pressure of the inert gas. In the sputtering process a high number of ions are produced (∼60% including cations and anions) [32], which is an advantage for ion manipulation such as mass selection and mass spectrometry.

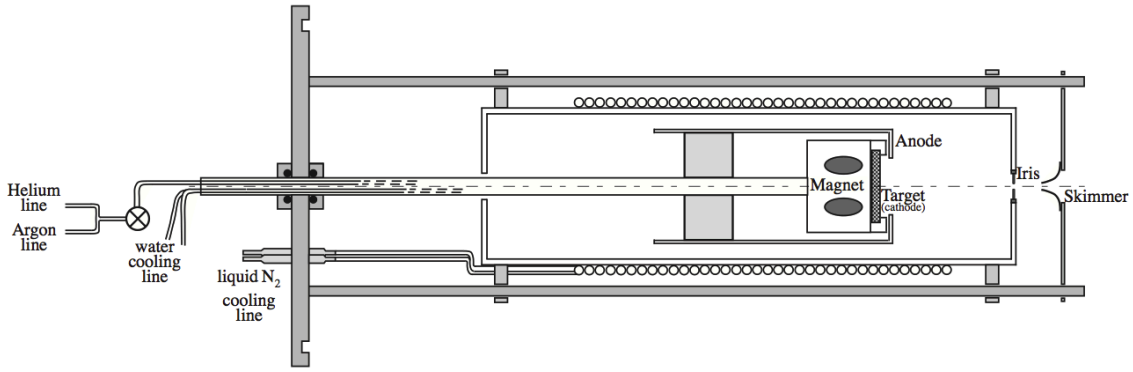

FIG. 3: *Schematic of the source. The cluster production is based on the target vaporization by sputtering using energetic ions in an inert gas atmosphere. The ejected atoms from the target are cooled via successive collisions with the inert gas and the aggregation process starts by single-atom addition.*

The discharge process starts when a dc potential is applied between anode and cathode (the target) and an argon flux flows through a small space between the two electrodes. A glow discharge is obtained forming a stable plasma and the argon

ions are accelerated toward the target surface. The plasma is confined by a toroidal magnetic field using a permanent magnet behind the target. To prevent that the magnet will be damaged due to overheating, a water cooling circuit is used.

During the discharge secondary electrons are produced and by the effect of the magnetic field they will be trapped into closed orbits increasing the ionization efficiency.

The metal atoms sputtered from the target are condensed by the inert gas. If the local thermal energy of the beam is low enough (roughly less than the binding energy of the dimer), then a three-atom collision between two sputtered metal atoms and an inert gas atom can lead to the formation of a dimeric nucleus. In this process the inert gas atom removes excess energy as kinetic energy and assures momentum and angular momentum conservation.

The initially formed cluster nucleus acts as a seed for further cluster growth by single-atom addition. Collisions between smaller clusters can lead to coalescence and the formation of larger clusters [42]. The cluster growth in this super saturated atmosphere, basically depends on the number of the successive collisions that they will undergo in this process.

A set of parameters is involved in the number of the collisions that clusters undergo in order to increase the size. One factor that determines the clusters size is the rare gas composition and pressure, in our case to get bigger cluster up to 6 nm we mix the argon with helium gas. The quantity of gas is optimized by two gas flow controllers, where the maximum flux is up to 200 sccm for helium and 500 sccm for argon. To extract this enormous amount of gas we use a turbo-molecular pump with a nominal pumping power of 1600 l/s. The cleanliness of the gas line is a determinant factor in the cluster production. The first stage for this work was to find and seal every kind of leak in the gas line, and for that we designed a protocol to verify the cleanliness of the source, that will be discuss at the end of this section. The magnetron head is mounted in a sliding system where the distance to the exit of the aggregation chamber can be varied. The distance that particles traverse determines the number of collisions that they experiment at a fixed pressure, thus defining the cluster size.

These two main factors, the pressure and the distance to the exit, control the main range of size for the cluster production. Small modification to the size can be performed by two additional parameters: increasing the discharge power increases the amount of material extracted from the target, increasing the size. And at the

end of the aggregation chamber a small diaphragm is mounted in order to modify the pressure and the flow conditions. This parameter controls the pressure but in a minor grade. The cluster beam is carried by the gas flow to the exit of the chamber where the aggregation process finishes.

This setup has been adapted in order to allow floating at a defined potential the current supply that feeds the discharge. The clusters are generated at this potential and this value will be extremely important in the entire process of beam transfer. The energy of the beam is measured by retarding field analysis (RFA), and the result displayed in **Fig. 4** corresponds to a gaussian distribution centered around the value of the potential applied to the current supply. The exact kinetic energy deviates slightly from the tube voltage due to 1) velocity gained in the inert gas flow and 2) kinetic energy lost in collisions in the high pressure region at the exit of the source tube.

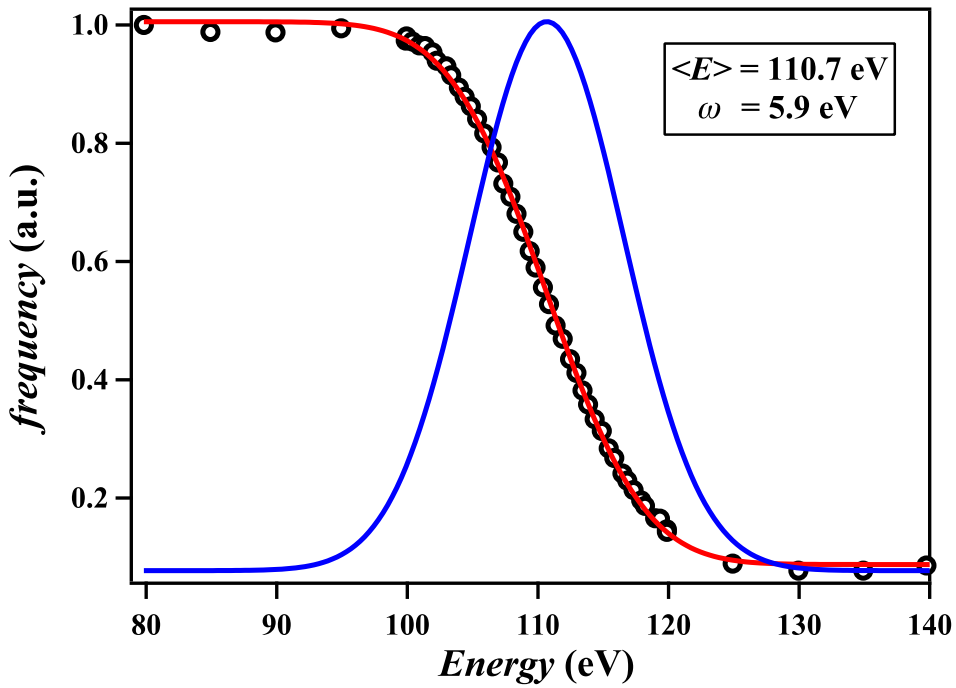

FIG. 4: *Energy spectrum of cobalt clusters with mean size of 2.8 nm of diameter, measured at the exit of the deviator. The applied potential corresponds to 112 V. The circles are the experimental data and the red line is a fit using a sigmoid function. The derivative of the fitting curve correspond to the blue line. The exact kinetic energy deviates slightly from the tube voltage due to 1) velocity gained in the inert gas flow and 2) kinetic energy lost in collisions in the high pressure region at the exit of the source tube.*

I.2.2 Transfer region and Deviator

This stage has two main objectives, to reduce the pressure of the gas coming from the source and to guide the ion beam toward the deviator. The TOF-MS and the deposition chamber are in HV and UHV, respectively, it is necessary to have two differential pumping stages between the source and these chambers.

In order to reduce the pressure, at the enter of the transfer region a mobile skimmer is placed which has by mission to skim off most of the rare gas. The conical shape of the skimmer with a small aperture in the center allows to block the most of the gas coming from the source, and leave to enter the cluster beam into the transfer region. After the skimmer a turbo pump allows to decrease the pressure by three orders of magnitude with respect to the source.

To guide the cluster beam to the transfer region a potential is applied to the skimmer, whose value is normally lower that the voltage applied to the power supply for the source. This drag can significantly increase the transmitted cluster current.

After that the beam is focussed by an electrostatic lens with three cylindrical electrodes, that together with the potential for the source and for the skimmer produce very narrow size distributions. The two first electrodes are connected to independent potentials and the third electrode is connected to ground. The lens is optimized in order to maximize the signal measured in the TOF-MS for the desired size. This process is not simple, but the values applied to the electrodes, to optimize the signal are normally close to the voltage applied to the tube assuring a maximum transference.

A second setup for the transfer region consist of replacing the lens by an octupole ion guide, that allows increasing five times the signal for small cluster with respect to the previous setup. This configuration is optimal to work up to 150 atoms per cluster.

At the end of the transfer region a Faraday detector is mounted onto the gate valve separating transfer and deviator in order to measure the ion current at this point. A similar detector is mounted at the exit of the deviator, and in the sample holder. This set of detectors together with the TOF-MS is an important tool to verify the alignment for all our system. When the alignment is perfect we can maximize the ion current with respect to the initial conditions for the source.

Once the ion beam enters to the deviator it can be deflected to the right or the left side, using an electrostatic quadrupole. Only for particular conditions (large energy dispersion) the deviator acts as a mass filter. Thus in order to ensure same cluster size in the TOF-MS and the deposition chamber sides, it is better adjust all the conditions in the source and the transfer region in order to decrease the energy dispersion and the deviator is only optimized to obtain a higher ion current.

At this point the cluster beam is composed only of positive charges, because the negative were blocked when the beam passes from the source to the skimmer and the neutrals do not feel the effect of the deviator.

I.2.3 Residual Gas Analysis (RGA)

We developed a protocol to assure the cleanliness and stability of the source. Any residual gas present in the source can modify the cluster formation, for example through cluster oxidation. In order to check the cleanliness of the gas line and to discard the presence of leaks in the source, we used a Residual Gas Analyzer (RGA). We measured a spectrum to determine the quantity of residuals, like H_2O, O_2, N_2, CO_2 and CO. The problem is that the absolute values change and it is sometime difficult to quantify the residual gas. In order to counteract the variations we record spectra and normalize them on the mean value I_m. With this data treatment we can quantify the residual gas with respect to main value for each time, to obtain an effective diagnostics of the source state.

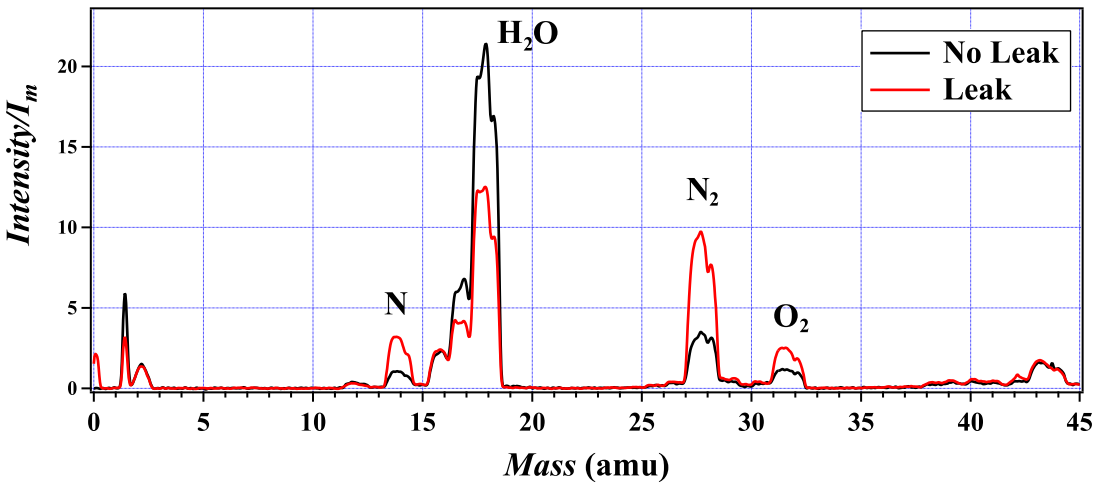

FIG. 5: *Two spectra normalized to their corresponding mean values. We observe that for the spectra recorded in presence of leaks in the gas line, the levels of oxygen and nitrogen are almost three times bigger with respect to the leak-free spectrum.*

In **Fig. 5** are displayed two spectra normalized to their corresponding mean values. We observe that for the spectra recorded in presence of leaks in the gas line, the levels of oxygen and nitrogen are almost three times bigger with respect to the leak-free spectrum. This is an essential point in order to avoid cluster oxidation where the growth process becomes uncontrollable. The quantity of water in aggregation chamber is reduced by pumping and cooling down using a liquid air circuit. By using this protocol for the RGA measurements it is possible to monitor the evolution of level of water as function of time in order to assure a clean environment for the cluster production.

I.3 TIME OF FLIGHT MASS SPECTROMETRY (TOF-MS)

I.3.1 Experimental

The Time of flight mass spectrometer is an important part of this setup, because this technique allows to determine the mass of the clusters in real time, and by tuning different parameters in the source, the cluster size is optimized at the moment of the deposition and verified through out. Additionally the amplitude of the signal measured in the TOF-MS spectra is related with abundance of clusters in the ion beam.

The operating process principle is relatively simple, a particle with a total charge zq and mass m, is accelerated using an electrostatic potential V resulting in a velocity proportional to the ratio of q/m. The central idea is to measure the time t that the particle takes to traverse a distance l. We can describe the time for a ideal case ($z = 1$), when particles with the same mass and charge arrive to the detector by:

$$t = \sqrt{\frac{ml^2}{2qV}} \tag{1}$$

In our case we have an ion beam where the clusters were formed in the gas-phase with a size distribution depending on the source conditions. Assuming that all the particles have the same kinetic energy when accelerate [77], they will have a distribution of velocities where the velocity for each size is proportional to the square root of m/q, that means when the ions reach the detector they are separated into families corresponding to m/q. The group of lightest particles reaches the detector first and is followed by groups of heavier mass.

This TOF-MS configuration was developed by Wiley and MacLaren [77] and optimized by de Heer and Milani [17]. The setup is composed of two main parts; the acceleration region and the field free tube, displayed in **Fig. 6**. The acceleration region consists of two stages separated by a small field free region. At the beginning of each stage a square pulsed electrostatic potential is applied to two plates, the first plate the *repeller* P_1 and the second plate the *extractor* P_2. At the end of the the acceleration region in order to well define the electric field of the exit of the acceleration region a grid P_3 is connected to ground. To each plate a pulsed electrostatic potential is applied independently and both pulses are synchronized.

Finally the signal is collected in the detector and the spectra is recorded in the oscilloscope.

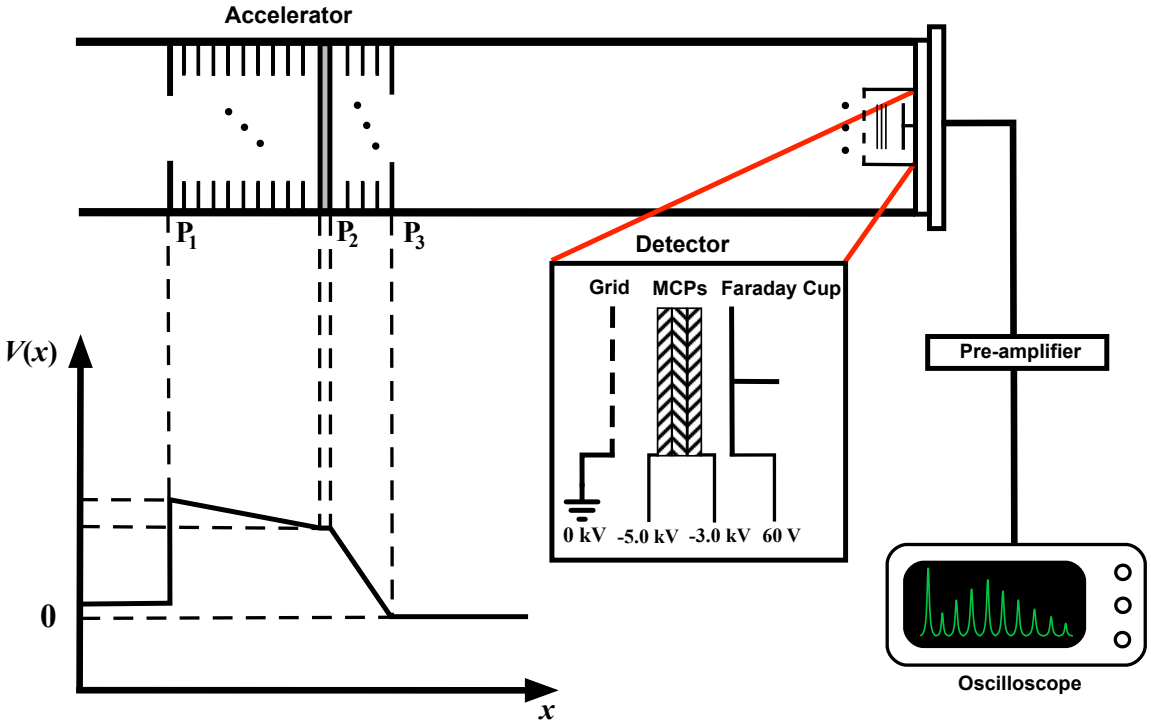

FIG. 6: *Schematic illustration of the TOF-MS. The acceleration region consists of two stages separated by a small field free region. At the beginning of each stage a square pulsed electrostatic potential is applied to two plates, the first plate the repeller P_1 and the second plate the extractor P_2. At the end of the the acceleration region in order to well define the electric field of the exit of the acceleration region a grid P_3 is connected to ground.*

This configuration with two stages allows increasing the time resolution by adjusting the ratio between the electrostatic potential applied to the plates. As the clusters have different positions at the moment when the pulse starts, then they will have different kinetic energies depending on the initial position. In order to counteract the dispersion in velocities due the dispersion in position, it is possible to adjust the electric field in the second stage assuring that clusters with the same mass arrive at the same time.

Typical values of the acceleration region and the pulse parameters are given in **Table I**.

TABLE I: *Typical values for the acceleration region, the pulse and the detector used in the TOF-MS.*

Repeller (P1)	+4.0 kV
Extractor (P2)	+2.8 kV
Pulse Length	180 μs
Pulse Frequency	20 Hz
Front MCP	-5.0 kV
Back MCP	-3.0 kV

The pulse length and frequency are regulated such as to detect in the case of cobalt clusters up to ten thousand atoms. The rise time of the pulse for each plate is around one hundred nanosecond, that means one order of magnitude lower than the time necessary to detect for example one atom of cobalt.

The detector is composed of three micro-channel plates (MCP), each MCP consists of an array of miniature electron multipliers oriented parallel to one another and the channels are disposed at a small angle ($\sim 8°$) with respect to the surface [78]. Typical dimensions for the channels are in the range of 10-100 μm for the diameter with a centre-to-centre distance ranging from 6-32 μm and $\sim$ 400 μm in length [18].

When an energetic ion hits the surface of the MCP secondary electrons are emitted from the surface and the current is amplified by an avalanche of emitted electrons. Applying a positive potential on the opposite side of the inner surface, the emitted electrons will be accelerated and impacting the channel walls produces an avalanche of emitted electrons [30]. To avoid that the ions enter parallel to the micro channels, the three MCPs are disposed in a cascade configuration, but rotated one with respect to the others. This configuration increases the probability to the electrons to impact the surface of the walls of the micro-channels and the signal will be amplified. The potentials applied at the *Front* and the *Back* of the detector are optimized in order to have a high intensity for the signal, their values are displayed in the **Table I**. After that the signal coming from the MCPs is collected by a Faraday cup and amplified by a pre-amplifier.

Finally the amplified signal is sent to the oscilloscope and the arrival time is measured for each mass. The oscilloscope is triggered by the same pulse that we use for the acceleration stage allowing to us know the precise time when the acceleration start and measure the arrival time with respect it. In order to increase the resolution

of the TOF-MS the potential of the *extractor* is optimized to get very sharp peaks. An example of a spectrum of cobalt clusters is displayed in the **Fig. 7**, where we observe that each peak represents cobalt clusters with different masses, starting from Co_1, meaning one cobalt atom, up to $\sim Co_{140}$.

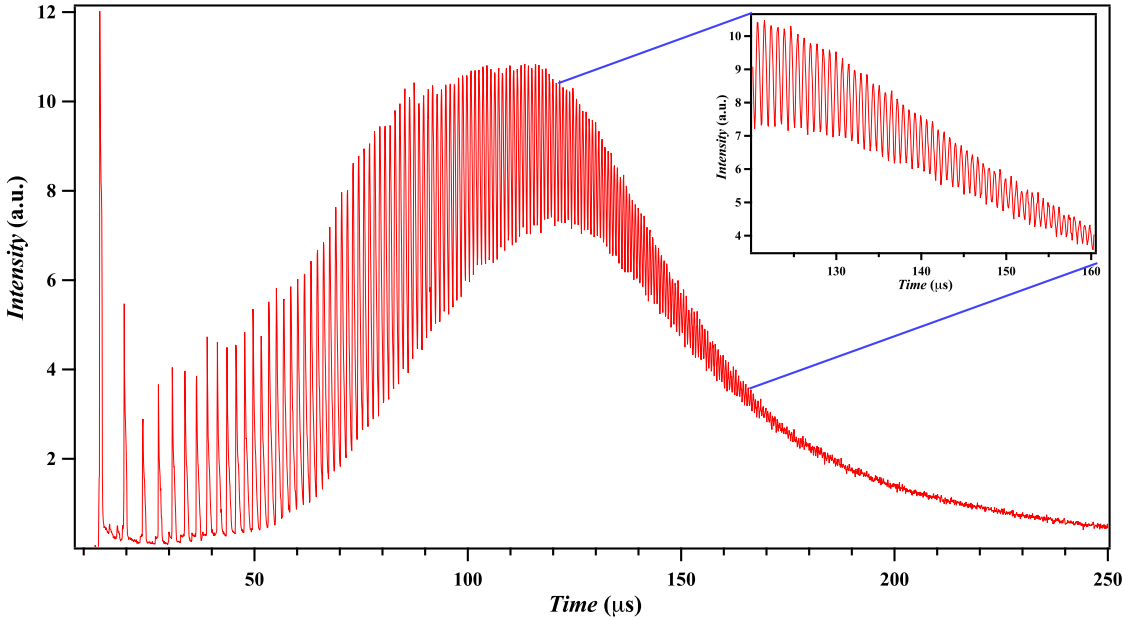

FIG. 7: *TOF-MS spectra of cobalt clusters where we observe that each peak represents cobalt clusters with different masses, starting from Co_1, meaning one cobalt atom, up to $\sim Co_{140}$.*

The resolution of the TOF-MS decreases as the size of the clusters increase, this means that the difference in time for two masses decrease as a function of the size. From **Eq. 2**, we can represent the difference of time of two masses by:

$$\Delta t = \left(\frac{l}{2\sqrt{2qVm}} \right) \Delta m \tag{2}$$

In the case of cobalt clusters we can clearly identify up to around one hundred forty atoms per clusters, which is displayed in the **Fig. 10**.

I.3.2 Calibration of TOF-MS spectra

The next step is to determine the size of the clusters from the measured spectra, *i.e.* to transform the measured arrival time into mass. Assuming that the distance that the particles traverse is the same, we obtain a relation of the ratio of the masses with the square of the ratio of the arrival times from the kinetic energy gained in the acceleration region. To determine the mass of the second particle m_2 it is necessary to know the arrival time for both particles and the mass for the first one m_1.

$$\frac{1}{2}m_1v_1^2 = \frac{1}{2}m_2v_2^2 \tag{3}$$

$$m_2 = \left(\frac{t_2}{t_1}\right)^2 m_1 \tag{4}$$

To calibrate the full spectra we improved a data treatment based on the condition that we need to have a set of identifiable peaks to extract the arrival times and relate these peaks with theirs expected masses. In the same way as in the the previous example for the two masses we used one mass like a guide to identify each peak and relate it with their expected mass. Fitting the dataset composed of the arrival times and their corresponding masses, we can determine a calibration factor to apply to the entire spectra converting the arrival time into number of atoms or diameter, even if we can no longer distinguish neighboring peaks.

If we consider for example the spectra in **Fig. 7**, we can identify around one hundred peaks.

We begin by fitting each peak, where we obtain the mean time for each peak for the entire set of masses (**Fig. 8**).

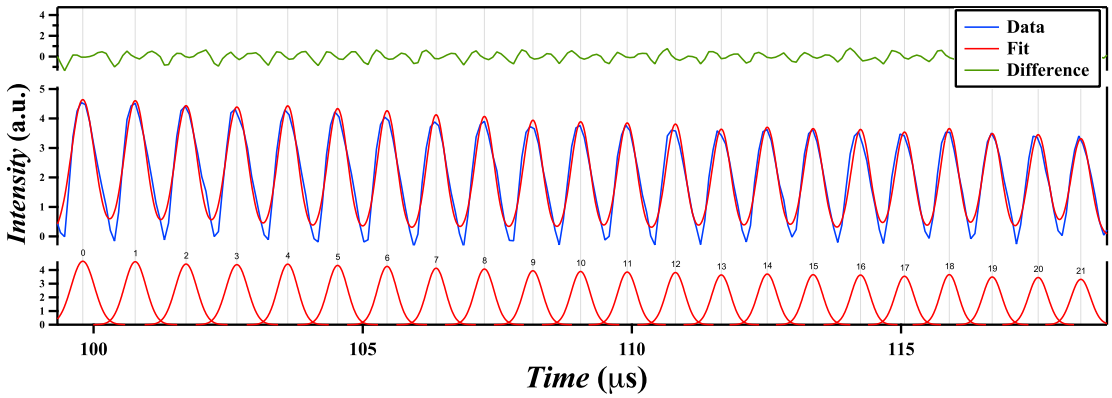

FIG. 8: *Fitting process for the set of peaks of a TOF-MS spectrum.*

To treat the data we assume that the energy which the particles gain is defined by an effective potential V_{eff}. This potential has the information about the initial energy U_0 and the energy gained in the acceleration region, and l is the effective distance travelled by the particles.

$$\frac{1}{2}mv^2 = qV_{eff} \tag{5}$$

$$m = \left(\frac{2qV_{eff}}{l^2}\right)t^2 \tag{6}$$

We get a quadratic dependency of mass with respect to time, that we transform into a linear expression by:

$$\ln(m) = a + b\ln(t)$$

where $a = \ln\left(\frac{2qV_{eff}}{l^2}\right)$ and b (the power of t) will be used like a fitting parameters. These two parameters are found from the fit and used to calibrate the spectra (**Fig. 9**).

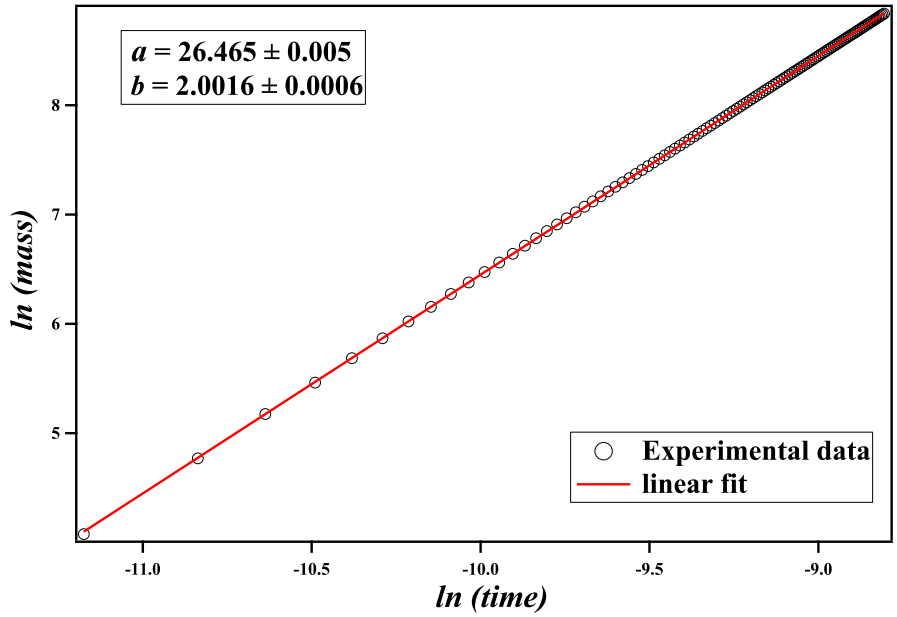

FIG. 9: *Linear fit used to calibrate the TOF-MS spectra.*

The calibrated spectra with respect to the number of atoms per cluster is displayed in **Fig. 10**. In the figure we used a grid to compare the expected value for the number of atoms with respect to the calibrated spectra.

To convert the number of atoms per cluster into diameter, we assumed the bulk molar density and a spherical shape for all sizes.

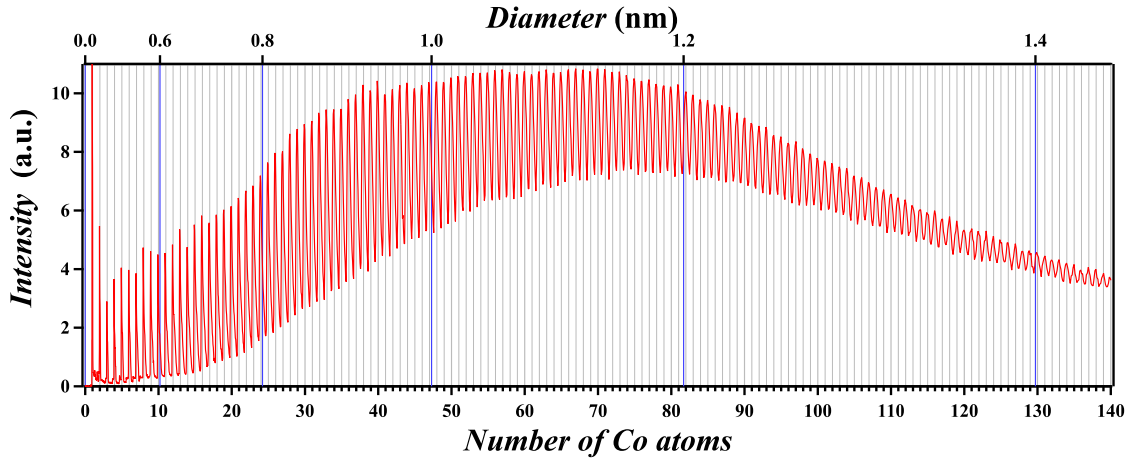

FIG. 10: *TOF-MS calibrated spectra for cobalt clusters. We used a grid to compare the expected value for the number of atoms with respect to the calibrated spectra.*

If we analyze the calibration factor as a function of the parameters behind it, we obtain values for the effective potential and the distance that are in agreement with the standard conditions that we use in the TOF-MS.

While the resolution of TOF-MS allows us to identify clusters with up to approximately one hundred atoms in the case of cobalt. To calibrate a TOF-MS spectrum for bigger clusters, where is not possible to identify individual peaks, first we record a spectrum for smaller clusters keeping identical conditions in the acceleration region and we change the source conditions in order to get the desired cluster size and we record the new spectra. Finally we use the calibration factor obtained for smaller clusters to calibrate the spectra for bigger clusters. The result obtained from the calibration needs to be checked with different experimental techniques as electron microscopy, femtosecond-spectroscopy, magnetic characterization and simulations.

I.3.3 TOF-MS analysis and simulations

At the first stage the ions arrive with a initial kinetic energy U_0 that depends on the source conditions. The ions are accelerated by the electric field E_1 traveling over a distance d_1, after that the clusters cross a distance d_2 ($E_2 = 0$) with a constant velocity, and in the second stage the ions are accelerated by E_3, during a distance d_3. Finally the ions arrive to the field free tube, where after a distance D, reach the detector. The dimensions and conditions of the TOF-MS are displayed in the **Fig 11**.

We can represent the total time t_T, using only classical mechanics by:

$$U = U_0 + U_1 + U_2 \tag{7}$$

$$t_1 = \frac{d_1(2m)^{\frac{1}{2}}}{U_1}\left(\left(U_0 + U_1\right)^{\frac{1}{2}} - U_0^{\frac{1}{2}}\right) \tag{8}$$

$$t_2 = \frac{d_2(2m)^{\frac{1}{2}}}{2\left(U_0 + U_1\right)^{\frac{1}{2}}} \tag{9}$$

$$t_3 = \frac{d_3(2m)^{\frac{1}{2}}}{U_1}\left(U^{\frac{1}{2}} - \left(U_0 + U_1\right)^{\frac{1}{2}}\right) \tag{10}$$

$$t_D = \frac{D(2m)^{\frac{1}{2}}}{2U^{\frac{1}{2}}} \tag{11}$$

$$t_T = t_1 + t_2 + t_3 + t_D \tag{12}$$

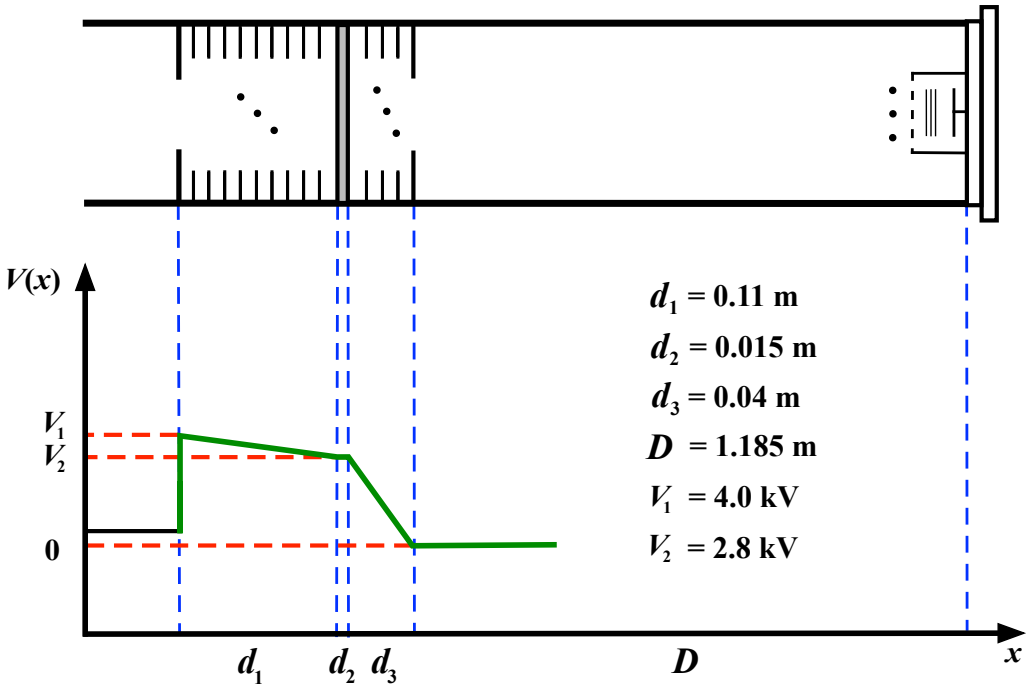

FIG. 11: *Schematic diagram of the TOF-MS, at the first stage the ions arrive with a initial kinetic energy U_0 that depends on the source conditions. The ions are accelerated by the electric field E_1 traveling over a distance d_1, after that the clusters cross a distance d_2 ($E_2 = 0$) with a constant velocity, and in the second stage the ions are accelerated by E_3, during a distance d_3. Finally the ions arrive to the field free tube, where after a distance D, reach the detector.*

If we compare using real conditions including the initial energy for different cluster sizes of cobalt (**Table II**), we are in good agreement with the simulated time.

TABLE II: *Arrival times calculated for the TOF-MS compared to the measured time for cobalt clusters with different number of atoms.*

Number of atoms	Time measured	Time Calculated
1	13.39 μs	13.33 μs
10	42.19 μs	42.17 μs
50	94.21 μs	94.29 μs

Now we will analyze the length of the pulse with respect to the time of flight in the acceleration region in order to estimate the limitations of our setup.

To reach the second stage it is necessary to acquire a minimal velocity before the pulse finishes, because is not the case the clusters will not be accelerated by the *extractor* and they will arrive much later that clusters with same mass. Thus it is possible to determine a critical cluster size where we are sure that all clusters left the first stage. A second consequence is a large temporal dispersion for this group of late particles, because the resolution in this setup is defined by acceleration given in the second stage.

We calculated the time to pass from the first to the second stage for different sizes that is displayed in the **Fig. 12**. For our setup the maximum pulse length at 4.0 kV assuring the stability of the power supplies is 180 μs. From the arrival simulated times we can observe that we are on the safe side working up at least around 5800 atoms, which corresponds to ∼5 nm for cobalt clusters. Thus in order to work with bigger clusters we need to pay attention in the compromise between the pulse length and the pulse frequency which are responsible for the stability of the power supply.

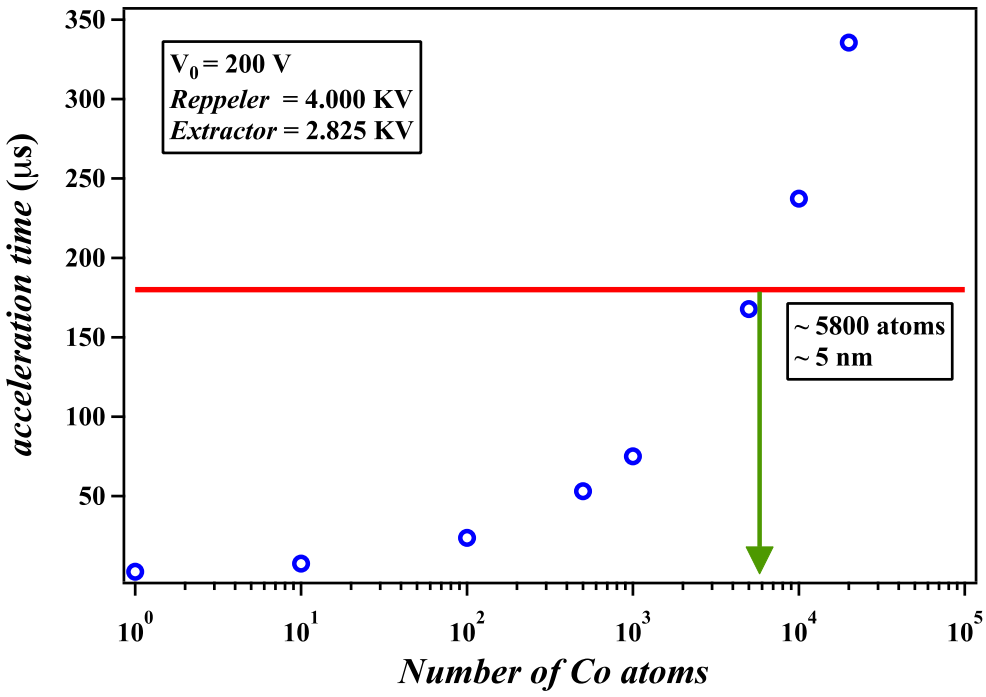

FIG. 12: *Acceleration time as function of the number of cobalt atoms.*

We simulated the arrival time in the acceleration region as a function of the position of the particles at the first stage in order maximize the resolution using different potentials in the *extractor* **Fig. 13**. The qualitative dependency of the resolution is in agreement with respect to experimental measurements and the maximum resolution is found at 2.825 KV. This value is 50V off with respect to experimental observations and could be explained by imperfections in the pulse shape.

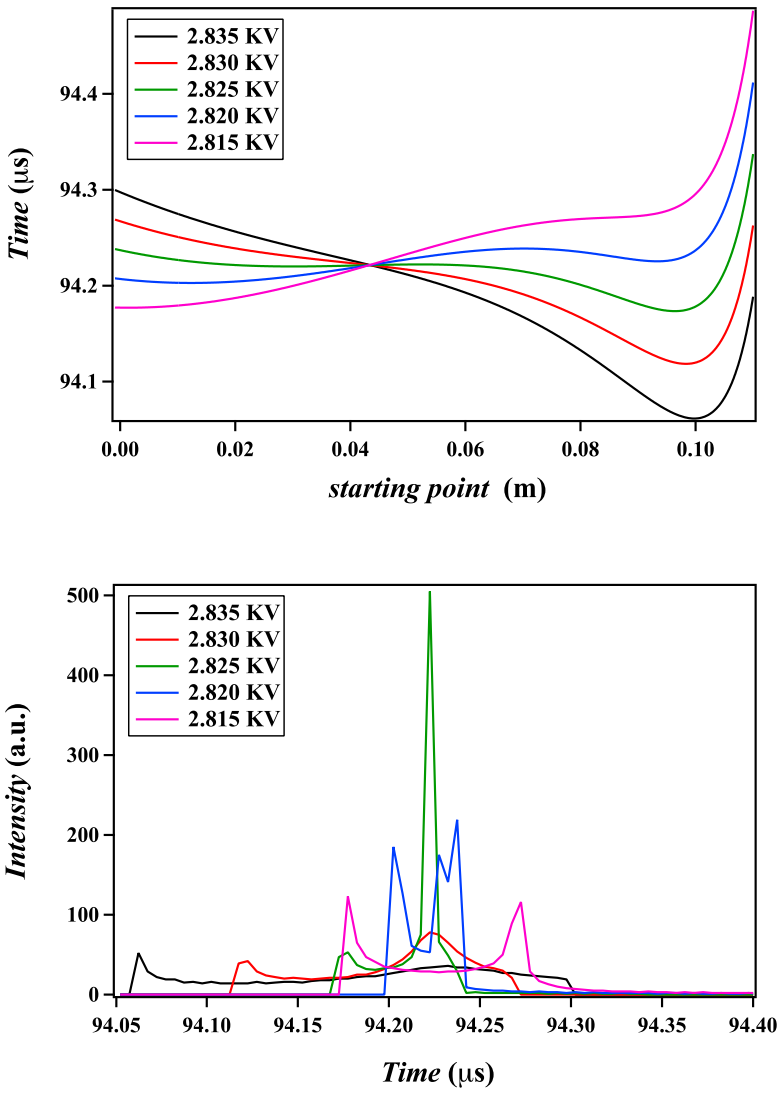

FIG. 13: *Arrival simulated times as function of the position. The qualitative dependency of the resolution is in agreement with respect to experimental measurements and the maximum resolution is found at 2.825 KV. This value is 50V off with respect to experimental observations and could be explained by imperfections in the pulse shape.*

I.3.4 TOF-MS complementary measurements

In order to test the quality of source conditions complementary to RGA shown in the previous section, the TOF-MS is an excellent technique to measure *cluster complexes*. In **Fig. 14** we observe the condition for the source a room temperature where is possible to detect the presence of water and argon and their combination with cobalt clusters.

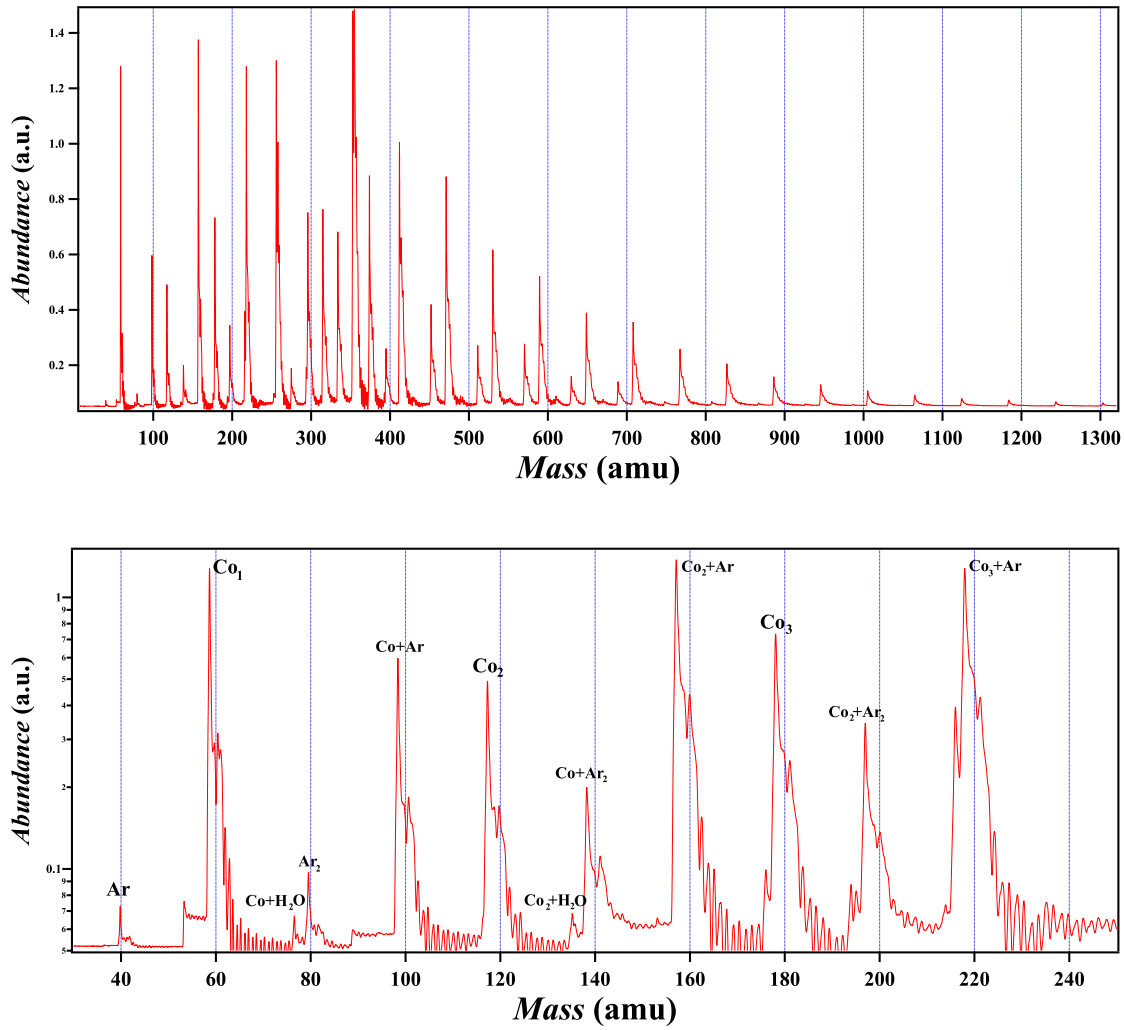

FIG. 14: *TOF-MS spectra of cobalt clusters and cluster complexes. We observe the condition for the source a room temperature where is possible to detect the presence of water and argon and their combination with cobalt clusters.*

I.4 SAMPLE PREPARATION

The samples described in this thesis consist of copper thin films (the matrix) of thickness around 100 nm with cobalt clusters embedded in it. The deposition is realized on two different substrates; silicon wafers for magnetic measurements and Kapton films for electrical measurements.

The sample preparation is based on the simultaneous deposition of the cluster beam and the atomic beam for the matrix under HV conditions. The substrates are placed at 45° with respect to each beam and both beams are perpendicular. This configuration, displayed in **Fig. 15**, assures identical geometric conditions for clusters and matrix deposition.

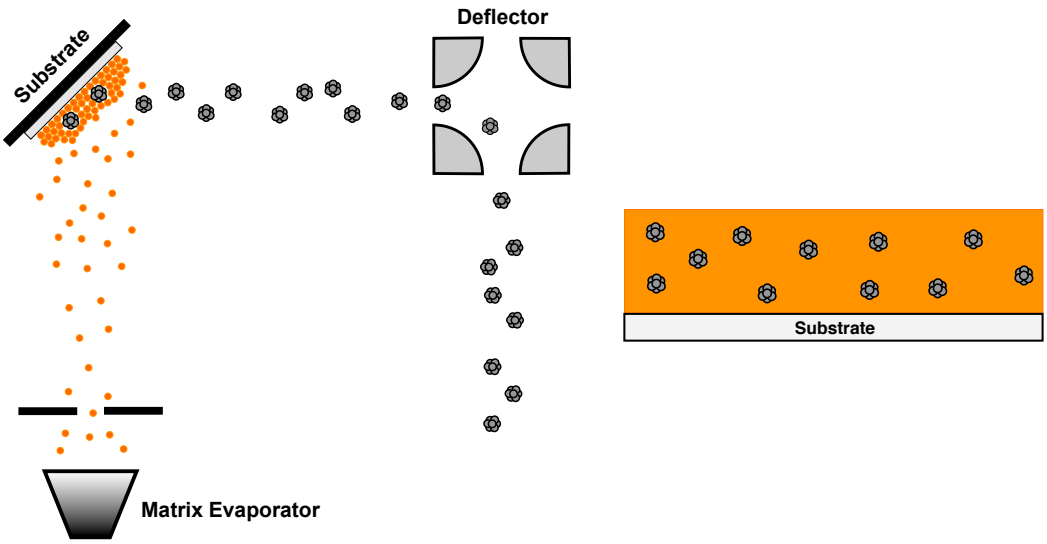

FIG. 15: *Left: Schematic illustration of the codeposition process. Right: Schematic of a sample, composed by a copper thin film with cobalt clusters embedded in it.*

For the sample preparation we have independent control over the cluster size and the concentration of the clusters in the matrix. The cluster size is varied by tuning a set of parameters in the source and the transfer region and the cluster concentration is controlled by adapting the deposition rate for the matrix.

The setup for the sample deposition consists of two main parts: the deposition chamber and the evaporation chamber. Each part is isolated with respect to the rest by valves that allow us to work independently. Each chamber is pumped by turbo-molecular pumps getting a static pressure of 8×10^{-10} mbar for the deposition chamber and 8×10^{-9} mbar for the evaporation chamber.

The ion current is measured in this part of the setup using Faraday detectors, the first one at the exit of the deviator and the second detector is placed in the sample holder with the same geometry as the substrates. The detector placed in the sample holder is composed of an internal and an external detector in order to estimate the spot size for the cluster beam. The value of the spot size is extremely important because it determines the quantity of ions per m^2 in order to obtain the deposition rate for the clusters.

A phosphor screen with MCPs is mounted on the sample holder in order to visualize and adjust the position and the shape of the cluster beam as complementary way as the internal and external detectors. The spot shape is modified by the values of the voltages applied to the three lenses at the end of the QMS and by the values of the voltage applied to the deflector.

I.4.1 Thin film preparation

The evaporation chamber is equipped with an electron gun that allows evaporating different kinds of materials, such as metals or insulators. In this work we used copper pellets with a purity of 99.999% that are evaporated by an electron beam emitted from a tungsten filament under high vacuum. The copper flux arrives at the deposition chamber and the thickness and the deposition rate are monitored by a quartz microbalance during the entire deposition process. The microbalance was calibrated using complementary techniques such as Atomic Force Microscope (AFM), X-Ray reflectometry (XRR) and Hall effect measurements. To reduce the pressure during the deposition, a cold trap with liquid air is located between the chambers that allows reducing the residual vapors of H_2O, CO_2 and CO. We use a RGA in the deposition chamber to verify the quantity of the residuals before and during the deposition in order to estimate the possible oxidation of the nanoparticles.

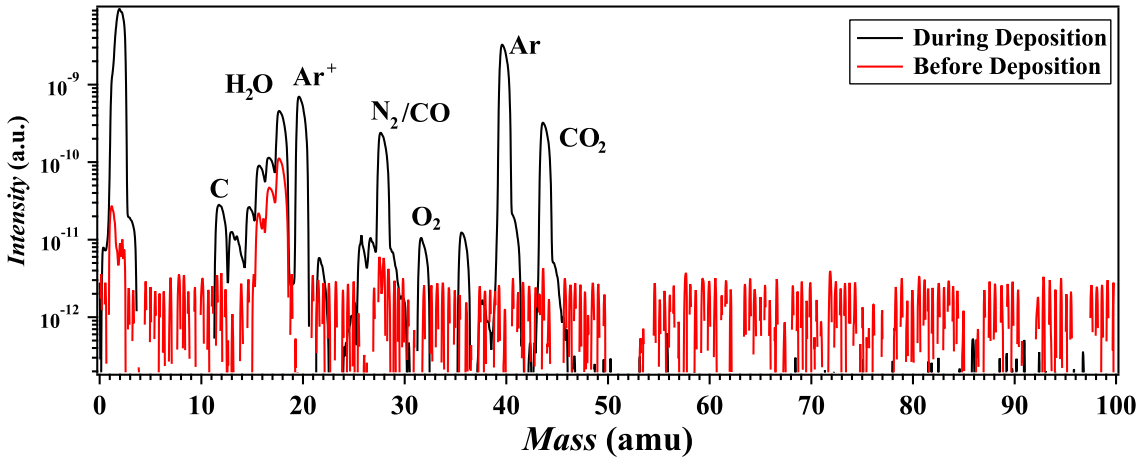

FIG. 16: *Two RGA spectra for the deposition chamber at different conditions. Before the deposition process we detect only the presence of water whose level can be reduce by baking the chamber. During the deposition process the level of oxygen corresponds to only a small fraction of the total atmosphere.*

In **Fig. 16** are displayed two spectra for the deposition chamber at different conditions. Before the deposition process we detect only the presence of water whose level can be reduced by baking the chamber. During the deposition process the level of oxygen corresponds to only a small fraction of the total atmosphere.

I.4.2 Quadrupole mass selector

After the deviator the cluster beam passes through a quadrupole mass selector (QMS) and arrives in the deposition chamber. For now the QMS was only used as an ion guide in order to maximize the ion current at the detector in the sample holder. The objective to use the QMS is to deposit a defined cluster size, for example a sample with clusters of only with twenty atoms.

The QMS is made of four parallel rods of circular section in a square configuration. Each pair of opposite rods is at the same potential and opposite values for each pair. The applied potential is composed of a DC component V and a AC component with amplitude Q and RF frequency ω, displayed in **Fig. 17**.

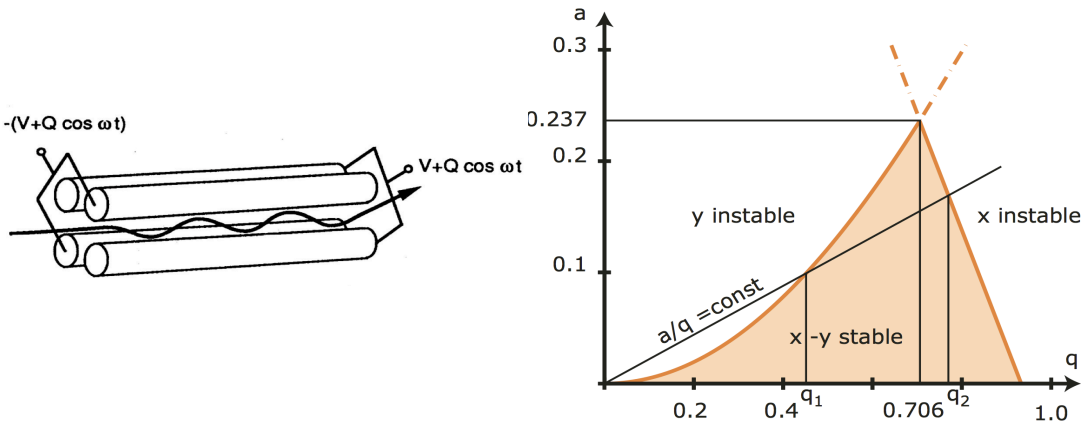

FIG. 17: *Left: Schematic representation of a quadrupole, each pair of opposite rods is at the same potential and opposite values for each pair. The applied potential is composed of a DC component V and a AC component with amplitude Q and RF frequency ω. Right: Stability diagram of the two-dimensional quadrupole field.*

When an ion enters the QMS, it is accelerated only in the directions where the potential is applied and keeps its velocity in the axis perpendicular to this plane. The possible trajectories of an ion are given by the solution of Mathieu's equations [30]. The stability of the trajectories depends on two coefficients a and q, which are proportional to V and Q respectively. The stability diagram, obtained by plotting the parameter a (ordinate, time invariant field) versus q (abscissa, time variant field), is displayed in the **Fig. 17**. Depending on the value of the ratio between V and Q, the quadruple works as mass filter or as a ion guide. For a high V/Q ratio, it will function as a mass filter, by letting through only ions whose masses are in a rather narrow window. When the DC component (V) is switched off, the quadrupole behaves as a

guide that focuses ions on the z axis [21]. Finally the ion beam is focused onto the sample holder position by three electrostatic cylindrical lenses.

I.4.3 Deposition

The sample holder allows mounting at the same time four substrates or TEM grids, where each sample is connected to the internal detector in order to measure the current ion current during the deposition. The cluster size is verified by turning the cluster beam to the TOF-MS side. When a cluster arrives at the surface of the sample, its kinetic energy will be transferred to the surface during the impact and the cluster could lose a few atoms in this process. To prevent the cluster fragmentation a voltage is applied to the sample holder in order to reduce their kinetic energy below 1 eV per atom [13]. Once *all the different parameters are optimized i.e.*: cluster size, deposition rate for the matrix, ion current, size and shape for the spot of the beam, the deposition process starts. Typical values for the pressure during the deposition are displayed in **Table III**

Once the codeposition is finished, the samples are covered by a copper protecting layer of 40 nm thick, with the objective to impede oxidation of the cluster when the sample is be exposed to air [26].

TABLE III: *Vacuum conditions for different regions of the experimental setup.*

	Pressure during operation (mbar)
Aggregation tube	1×10^{-1}
Source	2×10^{-2}
Transfer	1×10^{-4}
Deflector	5×10^{-6}
TOF	1×10^{-6}
Deposition chamber	3×10^{-7}
Evaporation chamber	3×10^{-7}

I.5 MEASUREMENTS

I.5.1 SQUID magnetometry

The SQUID (Superconducting Quantum Interference Device) measurements were performed using the MPMS-XL5 from Quantum Design at the *Centre de Magnétométrie de Lyon*. The SQUID is a highly sensitive device, where the basic principle is to detect the fluctuations in the magnetic flux, when the homogeneously magnetized sample oscillates through the detection coil. The variations in the magnetic flux induce an electric current in the detection system and this current will be proportional to the magnetization of the sample.

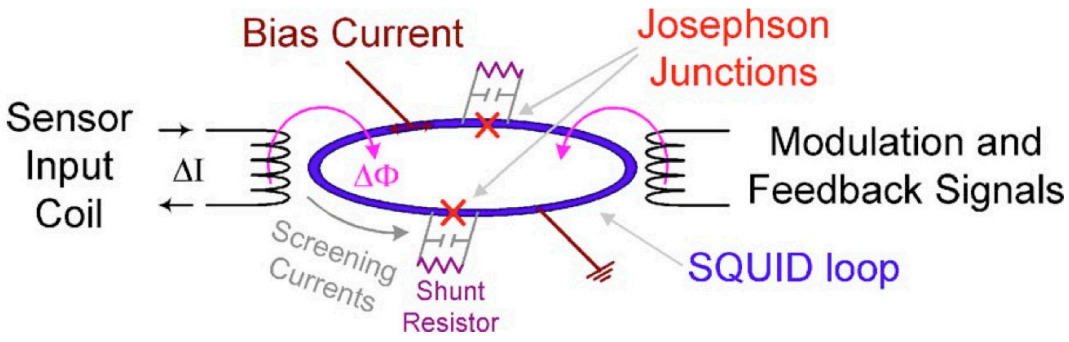

FIG. 18: *Schematic of the Superconducting Quantum Interference Device (SQUID)*

The detection system is composed by superconducting coils inductively coupled to Josephson junctions which operate below the superconducting transition temperature (**Fig. 18**). Any variation of the persistent current of the input coils will induce a current in the Josephson junction, and the voltage drop across the junction changes. Monitoring the change in the voltage provides a highly accurate measurement of the magnetic moment of the sample. The instrument allows to detect very low signals and is capable to resolve changes in external magnetic field at 10^{-15} T.

The detection system is mounted in a liquid helium cryostat, where the temperature can be varied from 2 K up to 400 K. The magnetic field of -5 T up to 5 T is produced by a superconducting coil. Two different measurements can be performed, the magnetization as a function of the magnetic field at a fixed temperature and the the magnetization as a function of the temperature at a fixed magnetic field.

I.5.2 Transmission Electron Microscopy (TEM)

To characterize nanostructures electron microscopy is an indispensable and complementary technique to obtain physical information of the sample. The dimensions of the particles are in the nanometric scale, and the electron wavelength for energetic electrons with 200 KeV is 0.003 nm. Under these conditions the resolution of the electron microscope is 0.1 nm, that means we can identify using high resolution imaging for example interatomic distances.

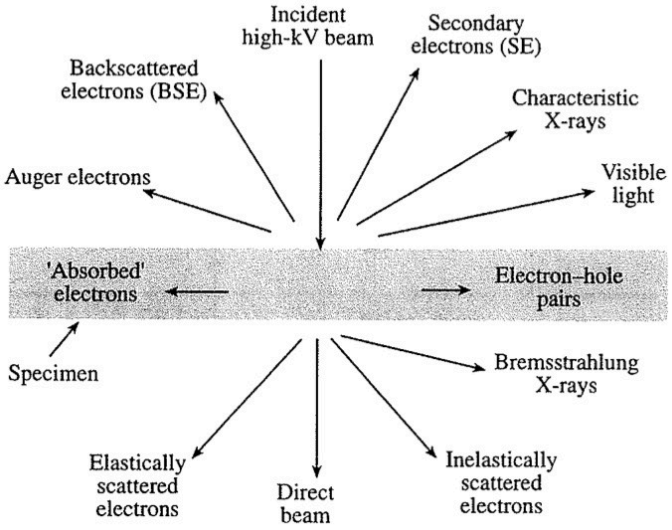

FIG. 19: *Schematic representation for different electron interactions. The electrons that emerge from elastic scattering have the structural information of the sample. The electrons that emerge from inelastic scattering have the chemical information of the sample.*

The electrons can interact in different ways with matter. The electrons that emerge from elastic scattering have the structural information of the sample. If we used these electrons to produce for example a diffraction pattern, we can obtained the crystallographic structure of the sample or lattice parameters. The electrons that emerge from inelastic scattering have the chemical information of the sample. This kind of interaction are used to perform different spectrometry techniques such as Energy-dispersive X-ray spectroscopy (XEDS) or electron energy loss spectroscopy (EELS). From X-rays it is possible to extract the chemical composition of the sample and quantify its components.

Using the microscope in image mode the electron beam traverses the sample and the emerging electrons are collected to form the image. Depending on of the thickness, density or chemical composition the electrons will be absorbed. The contrast in the image will depend on the atomic number Z of the element that composed the sample. In the interaction with heavier elements the electrons will be have a higher probability of being scattered. They will show thus a different contrast than lighter elements in the image.

For each image we adjust an ellipse to the selected particle and the effective diameter was obtained. A histogram was made with the series of the obtained values that for each sample was superior to 100 particles. The histogram is fitted using a log-normal function in order to get the median size and the dispersion of the size distribution. The results are contrasted with the mean size obtained from TOF-MS and show a good agreement for both techniques.

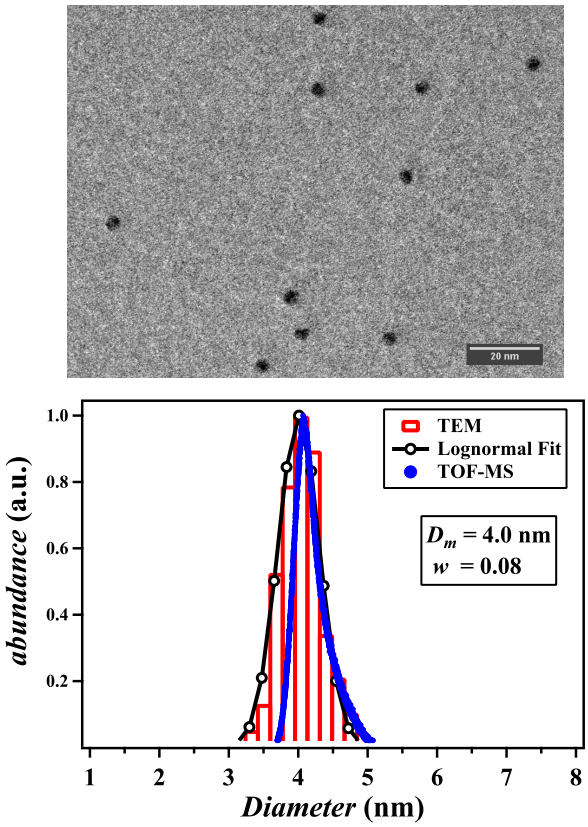

FIG. 20: *TEM image of silver clusters produced in the magnetron source and its corresponding histogram. The histogram is fitted using a log-normal function in order to get the median size D_m and the dispersion w of the size distribution.*

CHAPTER II

MAGNETIC PROPERTIES OF NANOPARTICLES

II.1 INTRODUCTION

Magnetic properties are modified with respect to the bulk when the dimensions of the structures are reduced to the nanometer scale. The resulting magnetic behavior is due to the competition of different magnetic energies and the length scale associated to the structure. Magnetic nanostructures whose dimensions are in the nanometric scale have interesting properties which depend strongly on the particle size. In order to extract the magnetic information from the nanoparticles it is mandatory to perform a complete magnetic characterization whose results must be contrasted with different experimental techniques allowing to have a solid base without ambiguity for further to studies of for example the influence of the cluster surface, shape or concentration on the magnetic properties.

In this chapter we present a description of the different kinds of magnetic energies associated with an ensemble of magnetic nanoparticles at the nanometric regime. The magnetic behavior is analyzed using different theoretical models and by different experimental techniques in order to describe and characterize this physical system.

II.2 FUNDAMENTALS

Ferromagnetic materials such as cobalt, nickel, and iron have the property of having a spontaneous magnetization even in the absence of an applied magnetic field. This effect is due to the alignment of the magnetic moments located in the atomic lattice and the magnetization direction is determined for example by crystal structure or the shape of the sample.

In order to minimize total energy E_T, the magnetic structure is divided into uniformly magnetized regions, denominated domains, separated by domain walls (Néel or Bloch walls). The domain structure and shape are determined by the final energetic equilibrium between the different energy sources.

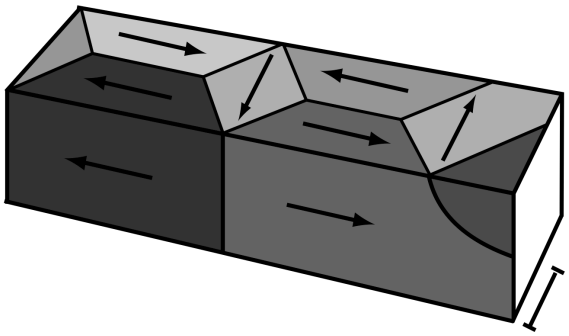

FIG. 21: *Schematic representation of domains and domain walls.*

The considered terms contributing to the total energy at a temperature of 0 K are:

$$E_T = E_{Exchange} + E_{Zeeman} + E_M + E_a \tag{13}$$

- $E_{Exchange}$: exchange energy.
- E_{Zeeman}: Zeeman energy.
- E_M: magnetostatic energy.
- E_a: anisotropy energy.

The exchange energy is given by:

$$E_{exchange} = \int_V A_E \left(\nabla \frac{M}{M_S} \right)^2 dV \tag{14}$$

The exchange energy comes from the microscopic coupling of the atomic magnetic moments and its origin is the result from Coulomb repulsion of two nearby electrons combined with the Pauli exclusion principle, which forbids two electrons to be in the same quantum state. This interaction is responsible of the spontaneous alignment of the magnetic moments and is described by the Heisenberg model, where, depending on the sign of the constant A_E, the interaction is ferromagnetic or antiferromagnetic. If $A_E < 0$ the interaction will be antiferromagnetic and the atomic magnetic moments are oriented antiparallel, and when A_E is positive the interaction is ferromagnetic and the atomic magnetic moments are parallel.

The Zeeman Energy is due to the interaction between the magnetization and the magnetic field and it is expressed by:

$$E_{Zeeman} = \mu_0 \int_V \vec{M} \cdot \vec{H} dV \tag{15}$$

The magnetostatic energy E_M or demagnetizing energy, is described by the interaction of the magnetization and the demagnetizing field H_{dm}. The demagnetizing field is created by the magnetization distribution of the magnetic charges and is related to the magnetization by $\vec{H}_{dm} = -\mathcal{N}\vec{M}$, where $\mathcal{N}$ is the demagnetizing tensor, which is represented by a symmetric 3×3 matrix.

$$E_M = -\frac{1}{2}\mu_0 \int_V \vec{M} \cdot \vec{H}_{dm} dV \tag{16}$$

For example in the case of a revolution ellipsoid, the demagnetizing energy divided by the volume of the ellipsoid can be written as:

$$\mathcal{E}_{dm} = \frac{1}{2}\mu_0 M_s^2 [N_{xx} - N_{zz}] \tag{17}$$

The anisotropy energy E_a is defined by natural orientation of the magnetization, and is generated by different contributions.

In the case of the magnetocrystalline anisotropy, this energy comes from the interactions of the atomic orbitals with the electric field (crystalline field) created by the environmental charges. In order to describe the magnetocrystalline anisotropy, the magnetization is expressed as function of the principal lattice axes of the material according to their symmetries. The energetically favorable direction of spontaneous magnetization is called *easy axis*.

The expression for a cubic material, is given by:

$$\begin{aligned} E_a = \int_V & K_1(\cos^2\alpha_1\cos^2\alpha_2 + \cos^2\alpha_2\cos^2\alpha_3 + \cos^2\alpha_1\cos^2\alpha_2) \\ & + K_2(\cos^2\alpha_1\cos^2\alpha_2\cos^2\alpha_3 + \ldots)dV \end{aligned} \tag{18}$$

Where K_i are the anisotropy constants and α_i are the angles between the magnetization and the crystallographic axes.

In the bulk, cobalt crystallizes in a hexagonal close-packed (hcp) structure where the principal axe is perpendicular to the hexagonal plane. For this symmetry, the magnetocrystalline energy represented in spherical coordinates is given by:

$$E_a = \int_V (K_1\sin^2\theta + K_2\sin^4\theta + K_3\sin^6\theta + K_4\sin^6\theta\cos\phi)dV \tag{19}$$

If we consider that the first term is dominant, we can represent this system in first approximation by a uniaxial anisotropy, and the anisotropy energy is expressed by:

$$E_a = K_1 V\sin^2\theta \tag{20}$$

In the presence of surface effects, the atomic magnetic interactions will experience a discontinuity at the surface breaking the crystalline symmetry. The magnetic moments of atoms at the surface will have the tendency to align parallel or perpendicular to the plane of the surface. We can describe the surface magnetocrystalline anisotropy energy for a cubic symmetry by:

$$E_a = K_s \cos^2 \alpha \tag{21}$$

Where K_s is the surface anisotropy constant and α is the angle between the atomic magnetic moment and the surface.

The demagnetizing energy, coming from long-range dipolar interactions in the particle induces a shape anisotropy. The demagnetizing energy has a quadratic form of the magnetization being possible to diagonalize. In an ellipsoid, a cylinder or a plate the shape anisotropy is uniaxial and we will describe as parallel to the z axis. If we suppose that the magnetocrystalline uniaxial anisotropy is parallel to the z axis, we can express the anisotropy constant by an effective anisotropy constant K_{eff} taking into account the magnetocrystalline anisotropy and the shape anisotropy energy, with N_{zz} and N_{xx} the demagnetizing factors, parallel and perpendicular to the z axis respectively [3].

$$K_{eff} = K_1 + \frac{1}{2}\mu_0 M_s^2 [N_{xx} - N_{zz}]) \tag{22}$$

The balance of the total energy will define the size of the domains. For typical magnetic materials the dimensional limit is in the range of 20-800 nm. Thus if a determined structure has dimensions below a critical size it will behave as a single domain. If we assume that the crystal has spherical shape we can estimate a characteristic radius given by $R_{sd} = 9E_\sigma/\mu_0 M_s^2$, where $E_\sigma \cong 2(K/A)^{1/2}$ is the total domain wall per surface unit, K is the anisotropy energy constant, A is the parameter that represents the exchange energy and M_s is the saturated magnetization. In the case of cobalt R_{sd} is about 35 nm.

Cobalt nanoparticles with a radius below R_{sd} behave as a single domain, where entire ensemble of atomic magnetic moments are aligned and rotate coherently. In this

configuration the total magnetic moment is represented by a single classical vector called *Macrospin* [45] [19] [8].

II.2.1 Superparamagnetism

In a single domain the anisotropy energy is proportional to the volume in first approximation assuming uniaxial anisotropy K_{eff} at zero magnetic field. Decreasing the particle size decreases the anisotropy energy which becomes comparable or smaller than the thermal energy k_BT, thus the total magnetic moment can thermally fluctuate in the same way as magnetic moments in a paramagnetic system.

This interesting magnetic behavior, where the atomic magnetic moments remain ferromagnetically coupled and can be represented by a Macrospin that can rotate independently, is called *superparamagnetism* (SPM) [8, 19, 45]. It is only valid for **non interacting** macrospins.

The anisotropy energy contributes to the total energy by the uniaxial term $K_{eff}V\sin^2\theta$ where θ is the angle between the magnetization and the easy axis. The total energy has two minima at $\theta = 0$ and $\theta = \pi$, corresponding to the alignment along the easy axis. Those two stable configurations are separated by an energy barrier $\Delta E = K_{eff}V$.
At a defined temperature the thermal agitation can reverse the magnetization of the particle when the energy barrier ΔE is overcome (**Fig. 29**).

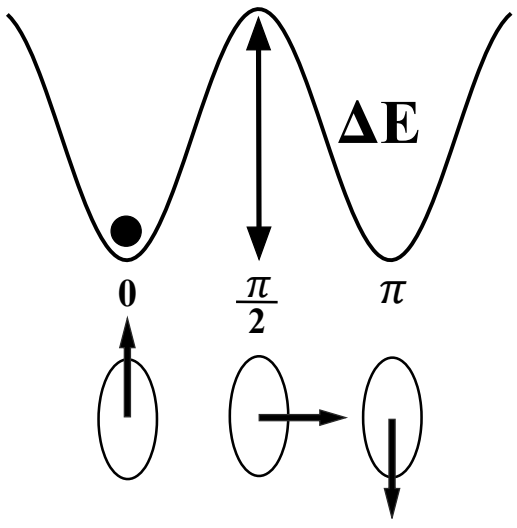

FIG. 22: *Schematic representation of the anisotropy potential barrier.*

In order to describe the magnetization reversal process as a function of the thermal activation, we introduce the Arrhenius equation for the relaxation time between the two magnetization states.

$$\tau = \tau_0 \exp\left(\frac{\Delta E}{k_B T}\right), \tag{23}$$

where τ_0 is a time constant with a value of $\sim 10^{-9}$ s and that can be determined by several ways such as the Néel or Brown models [8] [14] [52]. The value of τ_0 depends on temperature but this variation is negligible with respect to the exponential term.

In order to measure the magnetization of a single particle, the magnetic behavior will depend on the measuring time τ_m, that is related to the experimental technique performed, with respect to the relaxation time τ. In typical SQUID measurements $\tau_m \sim 10$ s.

When $\tau_m >> \tau$, the thermal relaxation appears so fast, that averaging over time, the magnetization will be zero and the particle will be in the superparamagnetic state.

In the case of $\tau_m << \tau$, the magnetization measured will have a value different of zero and the particle will be in the *blocked* state. The behavior for the blocked state in presence of a magnetic field will be discussed in the next section using the model developed by Stoner and Wohlfarth.

The blocking temperature T_B can be defined at $\tau = \tau_m$, represents the transition between the two states it is given by:

$$T_B = \frac{K_{eff} V}{k_B \ln\left(\frac{\tau_m}{\tau_0}\right)} \tag{24}$$

Using the previous values for τ_m and τ, and replacing in the **Eq. 24** is possible to calculate the value for the anisotropy energy [70] expressed by:

$$K_{eff} V \simeq 25 k_B T_B \tag{25}$$

Well above the blocking temperature, where the particles do not feel the presence of the potential well, the system will be in the superparamagnetic state. Such as in paramagnetic system the magnetization as a function of the magnetic field is described by a Langevin function $\mathcal{L}(x)$ and the dependence of the magnetization as a function of the temperature follows the Curie law $\sim 1/T$.

$$\begin{aligned} m(H) &= \coth\left(\frac{\mu_0 H M_S V}{k_B T}\right) - \frac{k_B T}{\mu_0 H M_S V} \\ &= \mathcal{L}\left(\frac{\mu_0 H M_S V}{k_B T}\right) \end{aligned}$$

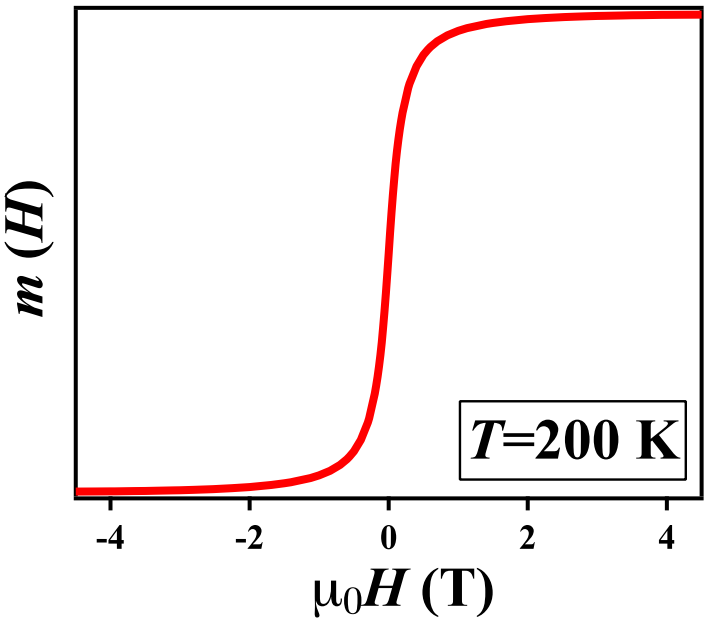

FIG. 23: *Simulation of the magnetization as function of the magnetic field described by a Langevin function for an ensemble of particles with 3.5 nm of diameter at a temperature of 200 K.*

From the **Eq. 26** it can be remarked that the magnetic behavior of a superparamagnetic system is determined by the competing actions of the external field and of thermal agitation. As a consequence, the magnetization scales with H/T.

II.2.2 Stoner Wohlfarth Model

In order to describe the magnetization reversal process of a ferromagnetic nanoparticle in presence of a magnetic field, we introduce the Stoner-Wohlfarth model [64] [68]. The ferromagnetic particle is describe geometrically as an elongated ellipsoid, where the major axis and the easy axis coincide (**Fig. 24**). The anisotropy is considered uniaxial, which produces an energy barrier $\Delta E = K_{eff} V$, where the anisotropy constant K_{eff} is independent of the volume V. The total energy at a temperature of 0 K, that describes the system is composed of the contribution of Zeeman energy and the anisotropy energy.

$$E = K_{eff} V \sin^2\theta - \mu_0 M_S V H \cos(\phi - \theta) \tag{26}$$

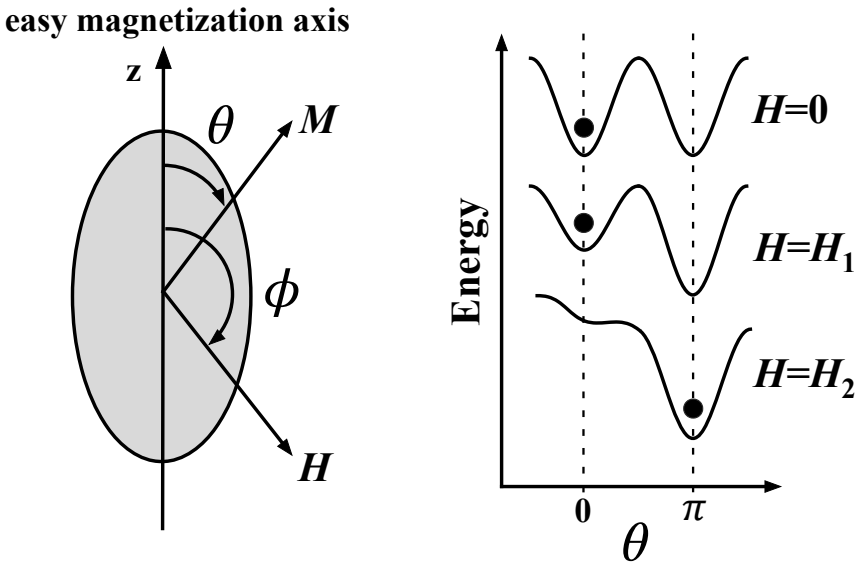

FIG. 24: *Schematic representation of a superparamagnetic potential well at different magnetic fields.*

When the magnetic field is applied the symmetry of the total energy is broken and a magnetization reversal process can occur. In **Fig. 24** the evolution of the total energy is displayed for three different values for the magnetic field ($0 < H_1 < H_2$). At zero field the magnetization is in the $+z$ direction in the initial state. When the magnetic field has the value of H_1, the magnetization tilts towards the direction of H_1, but in this case the process is reversible. When $H = H_2$, the magnetization is reversed and the process is irreversible and the final direction of the magnetization will be between $-z$ and the direction of H_2.

The value for the magnetic field H_a (anisotropy field) that induces the reversal process for $\phi = \pi$ is given by:

$$H_a = \frac{2K_{eff}}{\mu_0 M_S} \tag{27}$$

In order to calculate for a given magnetic field the stable values for the magnetization, it is necessary to minimize the total energy to determine its critical values.

$$\left(\frac{\partial E}{\partial \theta}\right)_{\theta=\theta_0} = 0 \qquad \text{and} \qquad \left(\frac{\partial^2 E}{\partial^2 \theta}\right)_{\theta=\theta_0} > 0 \tag{28}$$

Two conditions obtained are expressed for the reduced field $h = H/H_a$:

$$\big(\sin\theta\cos\theta + h\sin(\theta-\phi)\big)_{\theta=\theta_0} = 0 \qquad \text{and} \qquad \big(\cos 2\theta + h\cos(\theta-\phi)\big)_{\theta=\theta_0} \geqslant 0 \tag{29}$$

For general values of ϕ, the two equations **Eq. 29** cannot be solved analytically, except for $\phi = 0, \pi/4$ and $\pi/2$.

The solutions for a single particle are computed for different values of ϕ and the reduced magnetization m, which is obtained by normalizing the magnetization on the saturation value $m = M/M_S$, is plotted in function of the reduced field (**Fig. 25**). For $\phi = 0$ the cycle is a square and the coercive field H_c, i.e., the field necessary to reduce the magnetization to zero, is equal to the anisotropy field H_a, and the remanent magnetization m_R is equal to the saturation magnetization M_S or 1.

When the hysteresis loop is calculated at a temperature of $T = 0$ K for an array of non interacting nanoparticles with a random distribution of anisotropic axes such as a *realistic system*, the remanent magnetization $m_R = 1/2$, and the coercive reduced field is $h_c = 0.482$ (**Fig. 26**).

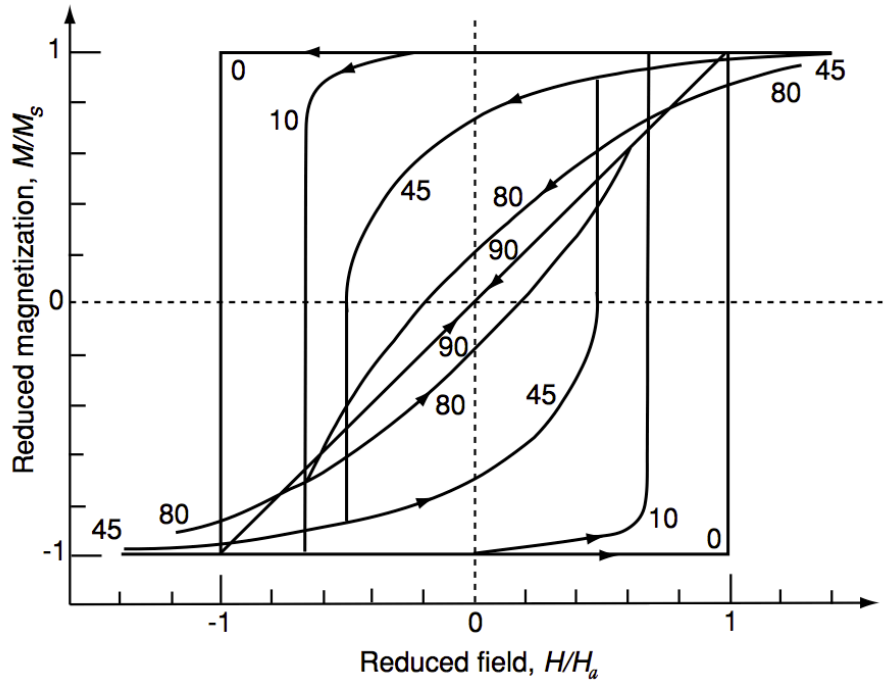

FIG. 25: *Magnetization curves for the Stoner-Wohlfarth model for various angles ϕ between the field direction and the easy axis.*

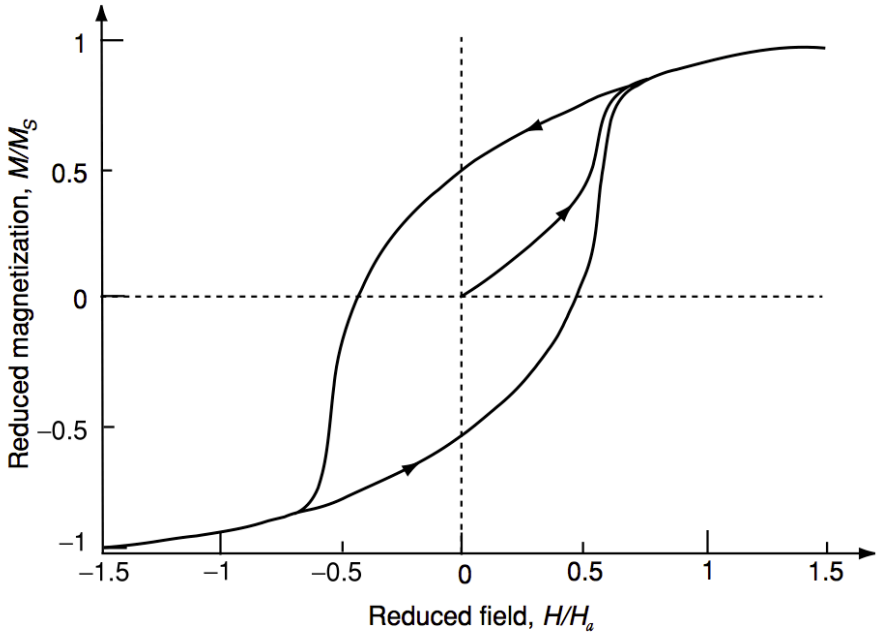

FIG. 26: *Hysteresis loop for a randomly oriented array of Stoner-Wohlfarth particles.*

II.3 MAGNETIC CHARACTERIZATION

In this thesis we studied the magnetic properties of ensembles of cobalt nanoparticles embedded in copper matrices with the objective to reveal the influence of the cluster size and the cluster concentration on the magnetic properties.

We used a SQUID magnetometer, where a set of several measurements were performed giving rise a complete characterization and thus forming in a solid base in order to understand the magnetic behavior of cluster-assembled nanostructures.

With respect to the impact of the cluster size on the magnetic properties, in the previous section we described that the anisotropy energy and the energy barrier will depend on the volume of the particles. When varying the cluster size the total energy of the system will be the result of combination of the different energy sources and we will try to elucidate the influence of the size-dependent anisotropy.

In order to study the evolution of the total energy as a function of the particle size or concentration is increased, we performed the ZFC/FC (Zero Field Cooled/Field Cooled) protocol together with magnetization measurements as a function of the magnetic field at different temperatures. A second protocol which consist of the IRM/DcD (Isothermal Remanent Magnetization/Direct current Demagnetization) was performed and both techniques together give a complete magnetic description of our system.

II.3.1 ZFC/FC susceptibility curves

The ZFC/FC (Zero Field Cooled/Field Cooled) protocol consists of the measurements of the magnetization as a function of the temperature at very low applied field. These experiments measure the trade-off between the different competing energies (Zeeman, anisotropy, thermal) and allow determining the magnetic anisotropy of the nanostructured system.

In the beginning the sample is cooled down from room temperature at zero magnetic field (ZFC) to the lowest temperature of our setup (2 K). A small magnetic field is applied (5 mT=50 Oe), preserving the linear dependency of the magnetization on the magnetic field, and the temperature starts to increase at a constant rate.

An ensemble of particles has a finite size distribution and the critical size for the progressive transition between the two regimes at 2 K is around ∼2 nm using **Eq. 24** which depends on the value of K_{eff}. At 2 K particles whose size is larger than the critical size will be in the blocked state and for sizes below this value the particles will be in superparamagnetic state. At zero field the mean magnetization is equal to zero, because total energy is completely symmetric thus statistically each orientation of magnetic moment is compensated by the orientation of another particle.

The effect of the magnetic field breaks the symmetry of the total energy (**Fig. 24**) and the magnetic moments of more and more particles will align with the field direction and the magnetization of the sample increases with temperature.

Once the thermal energy allows overcoming the energy barrier, the system will change from the blocked state towards the superparamagnetic state and the magnetization will decrease following the Curie law. In the ZFC we can distinguish a peak T_{max} that represents the signature of the magnetic anisotropy showing the passage from one regime to the other.

The FC measurement corresponds to cooling down at a non zero magnetic field and the ZFC/FC curves overlap following the Curie law around T_{max} according to the size distribution. After that the FC curve reaches a constant value where the system is at the blocked state.

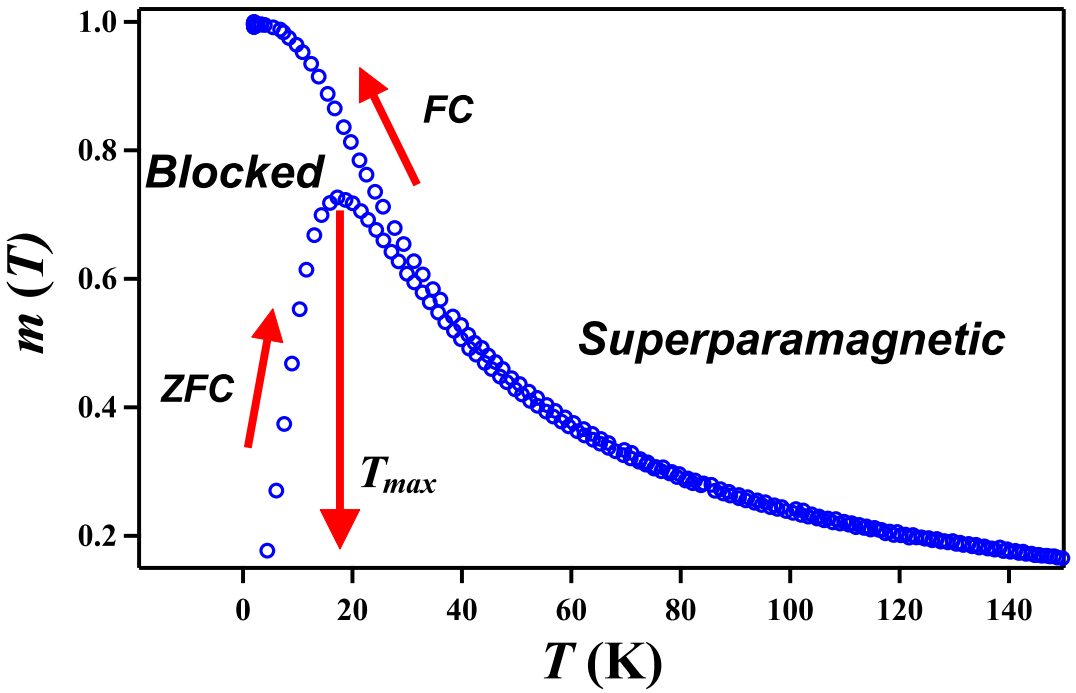

FIG. 27: *ZFC/FC susceptibility curves. The ZFC/FC protocol consists of the measurement of the magnetization as a function of the temperature at very low applied field. These experiments measure the trade-off between the different competing energies (Zeeman, anisotropy, thermal) and allow to determine the magnetic anisotropy of the nanostructured system.*

II.3.2 IRM/DcD measurements

The Isothermal Remanent Magnetization (IRM) curve corresponds to a series of measurements of the remanent magnetization at a fixed temperature. The protocol starts for a sample completely demagnetized. A magnetic field is applied and the magnetization increases, then the magnetic field is switch off and the remanent magnetization is recorded. This process is repeated increasing the value of the magnetic field in small steps. This technique allows to measure the irreversible magnetization variations of the sample.

In the case of an ensemble of particles with uniaxial anisotropy, the total energy at zero magnetic field is symmetric and in the beginning the orientation of the magnetic moments of the particles are randomly distributed. Thus the magnetization of the sample is zero, meaning that, statistically each orientation of magnetic moment is compensated by the orientation of another particle. When the magnetic field is applied this symmetry is broken and the energy barrier to overcome, from the

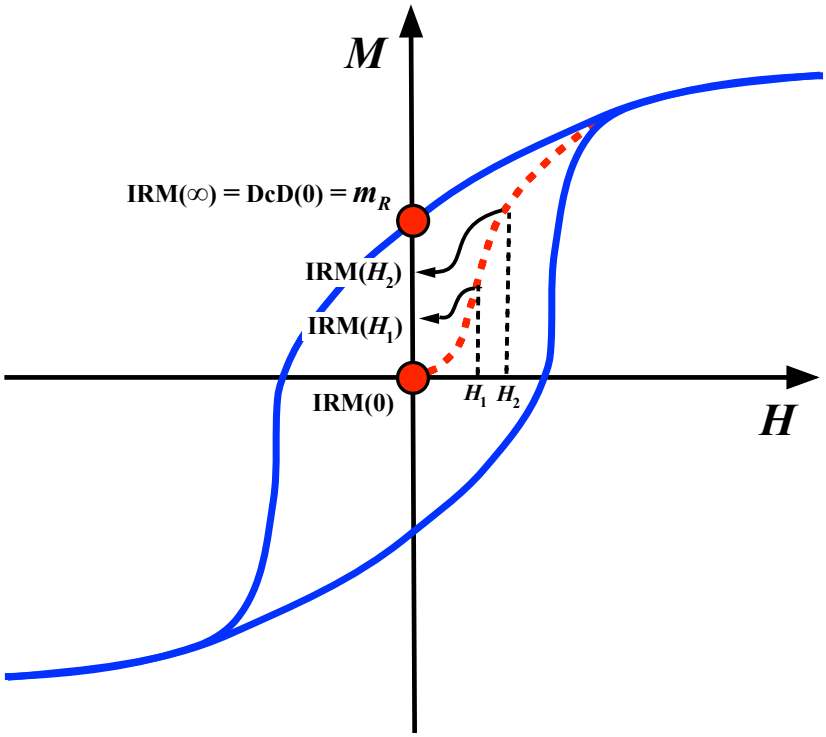

FIG. 28: *IRM/DcD protocol. The IRM curve corresponds to a series of measurements of the remanent magnetization at a fixed temperature and the DcD measurement is performed where the difference with respect to the IRM curve is its initial state.*

metastable to the stable well, decreases as the magnetic field increases. The energy barrier vanishes for a magnetic field $H > H_a$, when there is a single minimum of energy in the uniaxial case. Thus all the magnetic moments initially oriented in the opposite direction of the field will necessarily tilted. Finally the magnetization is reversed for the particles initially oriented antiparallel to the magnetic field (half of the total number of particles). At high field the IRM curve is identical to the hysteresis cycle at zero field after to saturate the sample and the value of the IRM curve is the remanent magnetization $\mathrm{IRM}(H = \infty) = m_R$.

A complementary measurement, the Direct current Demagnetization (DcD) curve, is performed where the difference with respect to the IRM curve is its initial state. This measurement correspond to the progressive magnetization reversal process. At the beginning the system is saturated to remanence m_R in a defined direction and the remanent magnetization is recorded following the same process that for the IRM curve but in the opposite direction. Initially all the particles are aligned in the magnetic field direction (saturation magnetization), and the magnetic field is applied

in opposite sense with the purpose to reverse the magnetization of the sample. This process involves to the entire number of particles in the system which differs from IRM curve where only half of them participate.

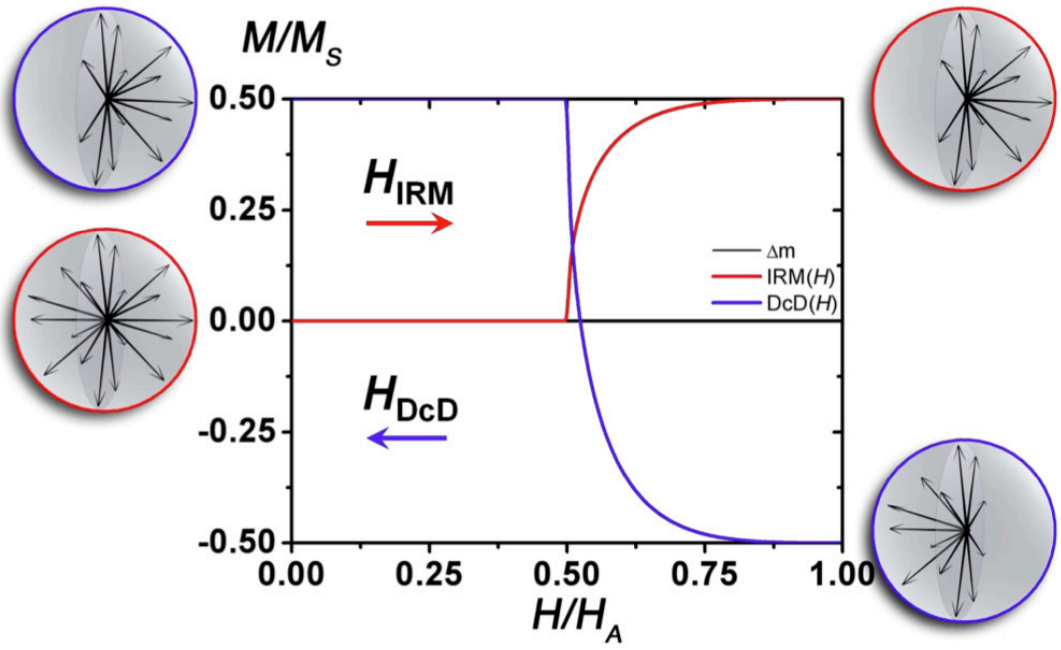

FIG. 29: *Schematic representation of the IRM/DCD measurements.*

As the starting point for the DcD is in remanence m_R, we can establish the following relation:

$$DcD = m_R - 2IRM \tag{30}$$

This relation is valid only in absence of any correlation between the magnetic moments of the particles due to magnetic interactions [43].

We can define the curve Δm [43], where the sign of Δm, determines the type of the interactions. For $\Delta m > 0$, the interactions are magnetizing and for $\Delta m < 0$ they are demagnetizing. In the case for $\Delta m = 0$, there is no indication of interactions.

$$\Delta m = DcD(H) - (m_R - 2IRM(H)) \tag{31}$$

This protocol is an extremely sensitive technique to detect interparticle interactions. In **Fig. 30** are displayed the IRM/DCD and Δm curves for two samples prepared with different cluster concentration but otherwise identical conditions. In the case of the more concentrated sample (5%), $\Delta m \neq 0$, showing interparticle interactions, while for the sample at 0.5% $\Delta m = 0$.

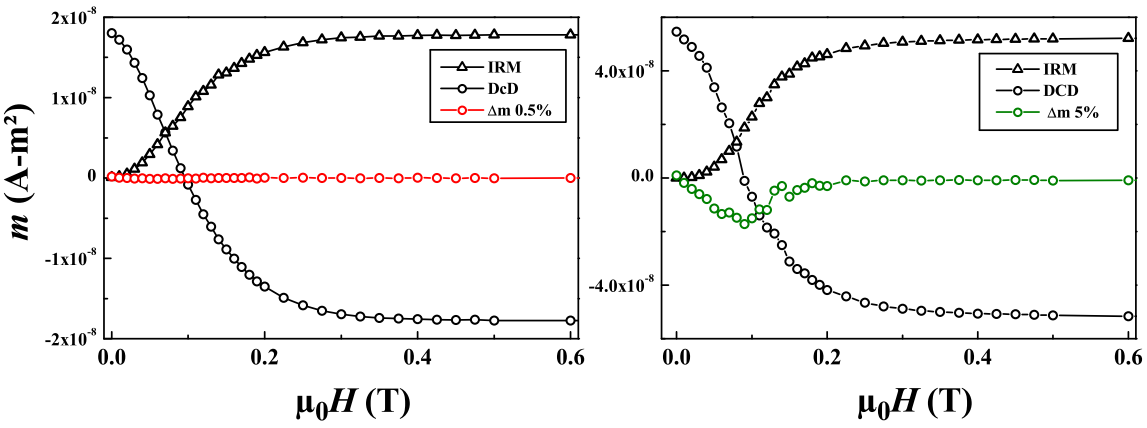

FIG. 30: *IRM/DcD and Δm curves for samples Co:Cu with different cluster concentration which diameter correspond to 2.3 nm. In the case of the more concentrated sample (5%), $\Delta m \neq 0$, showing interparticle interactions, while for the sample at 0.5% $\Delta m = 0$.*

II.3.3 Triple Fit

In the previous section we have shown different kinds of measurements and the magnetic information behind them. With the objective to extract the physical parameters involved in them, it is necessary to use an adequate model that describes the experimental data.

The magnetization at high temperature is described by the Langevin function $\mathcal{L}(x)$ (**Eq. 26**), similar to a paramagnetic system.

The physical system is composed of an ensemble of non interacting particles embedded in a nonmagnetic matrix, where the nanoparticles have a size distribution that from TEM observations we can represent by a log-normal function $f(D)$.

$$f(D) = \frac{1}{w_{mag} D\sqrt{2\pi}} \exp\left[-\frac{1}{2}\left(\frac{\ln(D/D_{mag})}{w_{mag}}\right)^2\right] \tag{32}$$

Where D_{mag} corresponds to the median diameter and w to the size dispersion. Thus the magnetization $m(H)$ as a function of the magnetic field at a fixed temperature with a size distribution, will be given by:

$$m(H) = N_t \int_0^\infty M_S \left(\frac{\pi D^3}{6}\right) \mathcal{L}\left(\frac{\mu_0 H M_S V}{k_B T}\right) f(D) dD \tag{33}$$

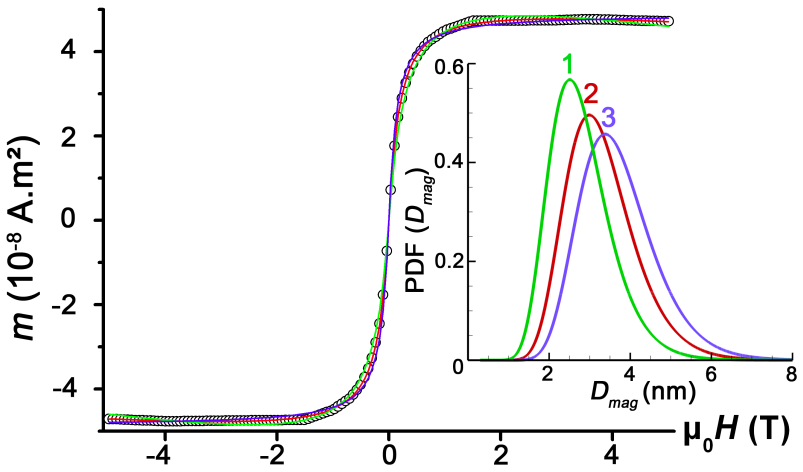

FIG. 31: *Simulation of the magnetization curves of a sample Co:Au for different size distributions at 300 K [66].*

When we describe the experimental data only using this simple model, we remark that this measurement is not sensitive enough to discriminate variations in the size distribution, such as the median size or the dispersion. In **Fig. 31** we get identical curves that overlap nicely for three different size distributions, making impossible to differentiate between them [66, 71].

In order to determine more accurately the magnetic anisotropy and the size distribution from the magnetic measurements a new method was developed, which consists of adjusting simultaneously the ZFC/FC susceptibility curves and the magnetization $m(H)$ at high temperatures using a semi-analytical model [66]. The model considers that each particle behaves as a Macrospin, that the particles have uniaxial anisotropy and the easy magnetization axes are randomly distributed. The anisotropy constant K_{eff} determines the anisotropy energy and is independent of the volume of the particles. The system is assumed as an ensemble of non interacting particles and the size distribution is described by a log-normal function (**Eq. 32**).

The ZFC and FC curves [70, 72] are described by :

$$m_{ZFC} = N_t \int_0^\infty \frac{\mu_0 M_S^2 V H}{3K_{eff}} \left(e^{-v(T)\delta t(T)} + \frac{K_{eff} V}{k_B T} \left(1 - e^{-v(T)\delta t(T)} \right) \right) f(D) dD \quad (34)$$

$$m_{FC} = N_t \int_0^\infty M_0 V e^{-v(T)\delta t(T)} + \frac{\mu_0 M_S^2 V^2 H}{3k_B T} \left(1 - e^{-v(T)\delta t(T)} \right) f(D) dD \quad (35)$$

Where

$$\delta t = \frac{k_B T^2}{K_{eff} v_T}$$

corresponds to the characteristic time, that takes account the temperature sweep $v(T)$.

For the FC curve

$$M_0 = \frac{m_0}{N_t \int_0^\infty V f(D) dD}$$

where m_0 corresponds to the value of the FC curve at 0 K.

From the simultaneous fit (triple fit) we obtain the anisotropy constant K_{eff}, the number of particles N_t, the median magnetic diameter D_m and the size dispersion w. This method was contrasted with the results from TEM observations showing a good agreement between both techniques (**Fig. 32**), the red line corresponds to the curves obtained by the triple fit, and the other color lines are constrained fits to the susceptibility curves based on the different magnetic diameter distributions from **Fig. 31**.

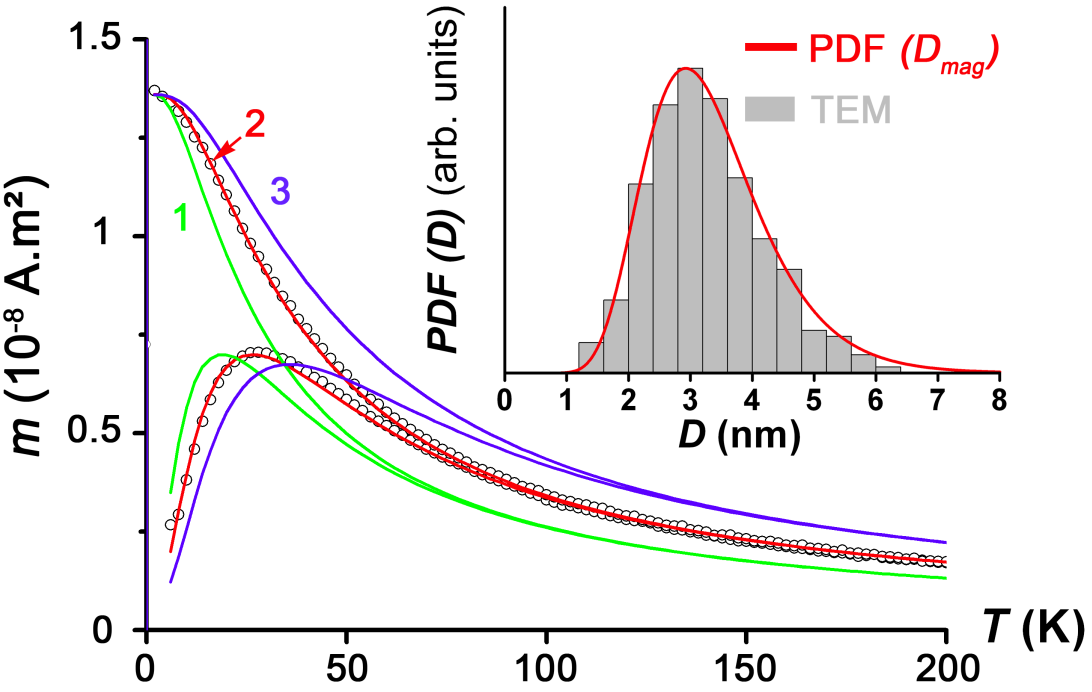

FIG. 32: *Triple fit results for cobalt clusters embedded in a gold matrix contrasted with TEM observations. The red line corresponds to the curves obtained by the triple fit, and the other color lines are constrained fits to the susceptibility curves based on the different magnetic diameter distributions [66].*

II.3.4 IRM and triple fit

According a prior study performed in our group [39], a simplified expression for the IRM curve can be expressed by:

$$\mathrm{IRM}(H,T) = m_R \frac{1-x^3}{1+x^3} \qquad \text{with} \qquad x = \frac{(1+2h^2)-\sqrt{12h^2-3}}{2-2h^2} \tag{36}$$

$$\text{Where} \qquad h = \frac{H}{cH_a} \qquad \text{and} \qquad c = 1 - \left(\frac{25k_BT}{K_{eff}V}\right)^{2/3} \tag{37}$$

As our system is composed by an ensemble of particles it is necessary to consider a size distribution $f(V)$, and thus the IRM curve can be calculated by:

$$\mathrm{IRM}(H,T) = \frac{M_S}{2}\int_{V_{min}}^{\infty} \frac{1-x^3}{1+x^3} V f(V) dV \qquad \text{with} \qquad V_{min} = \frac{25k_BT}{K_{eff}} \tag{38}$$

Where V_{min} corresponds to the volume below which the particles are in the superparamagnetic state and do not contribute to the IRM signal.

By using the triple fit protocol we determine the magnetic size distribution and the effective anisotropy constant, always considering that the magnetic anisotropy is uniaxial and has a single value K_{eff}. To simulate the IRM curve we use the same set of parameters obtained from triple fit showing a great disagreement with respect to experimental data, as is displayed in the **Fig. 33**. The sample corresponds to Co nanoparticles, with a mean diameter around 2.5 nm (lognormal size distribution, with a typical standard deviation of 0.7 nm), prepared in the gas phase and deposited fragmentation free onto a Si substrate together with an amorphous carbon matrix.

The lower slope observed in the IRM curve suggests a broader switching field distribution, which can be modeled by an K_{eff} distribution. We use a gaussian distribution function for K_{eff} where w_K corresponds to the anisotropy dispersion. With this addition it is possible to describe the experimental data for the IRM curve but the high value for the anisotropy dispersion necessary to describe the IRM curve makes incompatible to reproduce the ZFC/FC susceptibility curves (**Fig. 33**). This discrepancy can be understood by the different sources involve in the magnetization reversal process for each measurement.

For the low-field susceptibility measurements (ZFC/FC) the energy barrier is overcome by the thermal energy, independently of the direction of the applied field. In the case of the IRM curve the magnetization reversal process is induced by the magnetic field at a fixed temperature and the magnetization will be reversed when the energy barrier vanished.

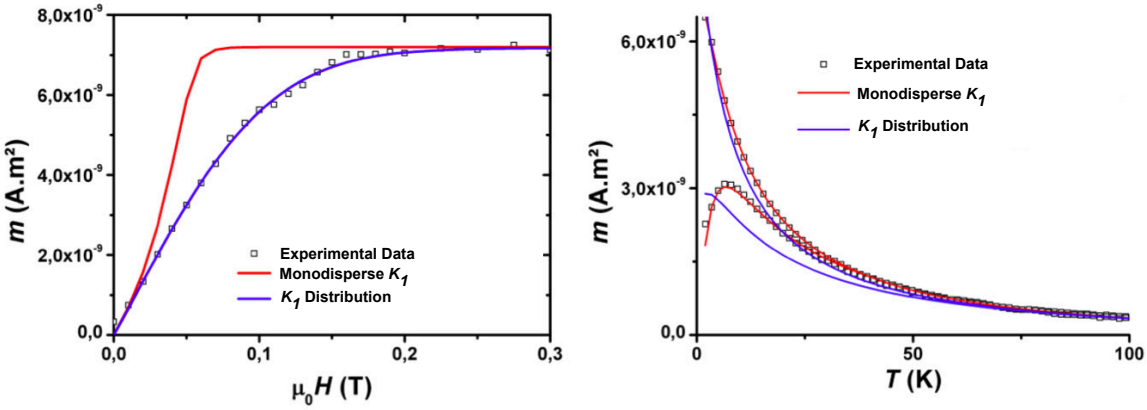

FIG. 33: *IRM and ZFC/FC curves simulated considering a single value for the anisotropy constant (red line) and an anisotropy distribution (blue line). The sample corresponds to Co nanoparticles, with a mean diameter around 2.5 nm (lognormal size distribution, with a typical standard deviation of 0.7 nm), prepared in the gas phase and deposited fragmentation free onto a Si substrate together with an amorphous carbon matrix.*

To simulate the IRM curves, a second factor to include is the presence of a second anisotropy axis contribution K_2 in agreement with previous studies on cobalt nanoparticles [41]. The K_2 term that also induces a broad switching field distribution for the IRM curve. Thus the IRM curve can be calculated using both contributions K_1 and K_2. The second anisotropy axis will not modify the distribution of the blocking temperature and thus without to affect to the ZFC/FC susceptibility curves.

Finally assuming an anisotropy dispersion for K_{eff} and a second anisotropy axis contribution K_2, it is possible to describe the experimental data using the same set of parameters for the ZFC/FC susceptibility, $m(H)$ and the IRM curves **Fig. 34**. Once the set of parameters are obtained, the magnetization cycle at a temperature of 2 K are simulated using a modified Stoner-Wohlfarth model [65] showing a good agreement with experimental data.

In the **Fig. 34** are displayed the experimental data for ZFC/FC, $m(H)$ and the IRM curves, the triple fit is performed considering the anisotropy dispersion and for the case of IRM and $m(H)$ at 2 K simulations adding the biaxial contribution. The agreement of the simulations and the experimental data using the same set of parameters is remarkable.

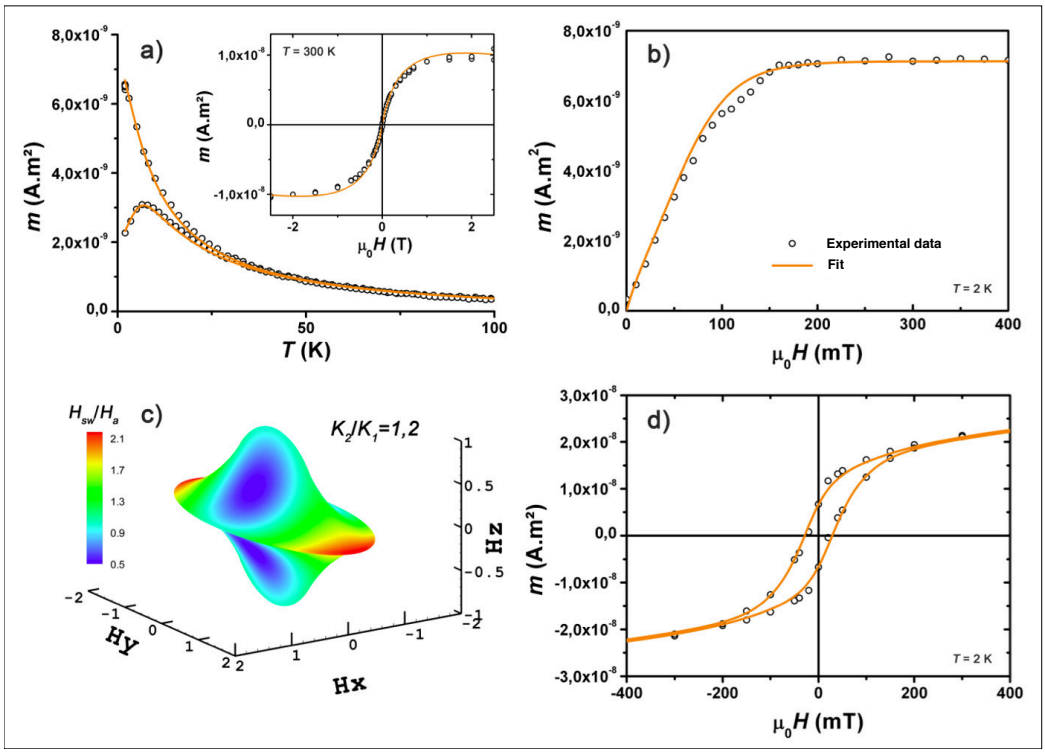

FIG. 34: *Triple Fit (a), IRM (b) and m(H) (d) at 2 K simulations considering an anisotropy dispersion and biaxial anisotropy. (c) corresponds to the Stoner-Wohlfarth astroid. The sample corresponds to Co nanoparticles, with a mean diameter around 2.5 nm (lognormal size distribution, with a typical standard deviation of 0.7 nm), prepared in the gas phase and deposited fragmentation free onto a Si substrate together with an amorphous carbon matrix.*

chapter III

Magnetic anisotropy of cobalt nanoparticles

In the last years magnetic nanostructures have attracted a lot of attention due to their potential applications in high density magnetic recording data [58, 61]. Their future applications are limited by the transition between the blocked and superparamagnetic regimes [8, 45] where the energy barrier $\Delta E = K_{eff}V$, necessary to overcome and reverse the magnetization, is defined by the magnetic anisotropy energy (MAE). The contributions to the MAE can be separated into two mean parts: the magnetocrystalline anisotropy and shape anisotropy [40]. The magnetocrystalline anisotropy has been widely studied from experimental and theoretical point of view. The origin of the MAE is in the coupling of the magnetization with the crystal lattice through spin-orbit (SO) interaction [74] as was presented in **chapter II**. At the cluster surface the crystalline symmetry is broken, giving rise to a new contribution called surface magnetocrystalline anisotropy. Reducing the cluster size the fraction of the atoms at the surface increases and the influence on the magnetic anisotropy becomes more and more important [41].

Different studies have been performed in order to investigate the magnetic anisotropy of nanoparticles and new techniques were developed to access to it, such as X-ray magnetic circular dichroism (XMCD) [63] and micro-SQUID [76] measurements.

XMCD is an useful technique that allows to access to the orbital and spin magnetic moments. Diverse investigations on cobalt nanoparticles by XMCD have been made to study the influence of the surrounding matrix (Cu, Au, Ag and Al_2O_3) on the spin-orbit coupling that gives rise to the surface anisotropy which varies with respect to the material of the matrix [6, 20, 27, 44, 46]. An important relation was proposed by Bruno for transition-metal monolayers [15] that relates the difference between the in-plane and out-of-plane orbital moments to the surface anisotropy by a tight-binding approach. Recently measurements on Co thin films capped by Cu well fulfilled this relation by showing a low SO coupling between Co and Cu [4].

Different calculations have been performed to estimate MAE of small clusters composed of $\sim$ 40 atoms with respect to the particle size [56]. The MAE shows a complicated behavior as a function of cluster size and by investigating different relaxations in the cluster structure, it is shown that the existence of nonuniform pattern of interatomic distances causes significant variations in the magnitude of the MAE [31].

In particular for cobalt cluster with sizes between 2-4 nm in diameter (400-2000 atoms) a tight-binding (TB) approach [81] and the phenomenological Néel model [53] were used in order to estimate the value of the magnetocrystalline surface anisotropy for different structures for cobalt nanoparticles such as a truncated FCC octahedron [40] and icosahedron [47]. The values obtained for the effective anisotropy constant in the first method (TB) depending on the cluster symmetry are in range of 60-530 kJ/m^3 and for the second one (Néel model) 160-200 kJ/m^3 (11-14 μeV/atom) for the truncated octahedron and 50-200 kJ/m^3 for icosahedron. These calculations are in agreement with the experimental results performed by micro-SQUID for a single cobalt cluster embedded in a Nb matrix where a value of K_{eff}=220 kJ/m^3 was determined [41].

Yanes *et al.* [82] performed different calculations to describe the energy barrier for magnetic nanoparticles by using the Néel model for the surface anisotropy. They compare with the widely used formula for $K_{eff} \cong K_{bulk} + 6K_S/D$, where K_S corresponds to the surface anisotropy constant that become important with respect to the

bulk value when the diameter D of the particles decreases. They conclude that this expression is valid when the shape of the particles is modified by a small elongation.

The demagnetizing energy is controlled by the shape of the particles and earlier classical calculations allow to estimate the magnetic anisotropy for a general ellipsoid as a function of its three preferential axis [54]. The anisotropy constant is determined by the aspect radio corresponding to the ratio between the major and minor semi-axes. For a sphere (aspect ratio of 1) the shape anisotropy is 0 and for small elongations whose aspect ratio is in the range of 1.1-1.2 the anisotropy constant for a revolution ellipsoid is 20-60 kJ/m^3. Recent studies show the shape anisotropy energy makes a contribution to the total energy even for relatively small shape distortions, with equivalent ellipsoids having aspect ratios of 1.1 [73].

In granular systems the total magnetic anisotropy will be composed of the contributions of the shape and the surface anisotropies. The effect of the surface will be more important for small particles and almost negligible for bigger ones. Until now there are no studies to define the region of sizes where each contribution become dominant and the corresponding size where the transition is produced.

In this work we study the magnetic properties of a set of samples with varying particle size. With the propose to extract the most of the magnetic information and to elucidate the influence of size of the particles on the magnetic anisotropy we performed a complete magnetic characterization and data treatment. In order to describe the magnetic anisotropy we take into account the demagnetizing energy to study the influence of the shape of the particles and the Néel model for the surface magnetocrystalline anisotropy.

III.1 EXPERIMENTAL

The samples consist of cobalt nanoparticles embedded in copper matrices, where the mean particle diameter was varied from 1.9 nm to 5.5 nm. The samples were prepared in order to study size effects of magnetic properties. The mean size was obtained by TOF-MS during the deposition process and TEM grids were prepared at identical source conditions in order to compare the magnetic results with electron microscopy and magnetic measurements. The cobalt concentration was reduced until the most sensitive measurement no longer detect any significant coupling, thus minimizing cluster interactions (0.2-0.3% of concentration). The samples were characterized by the triple fit protocol and by IRM/DcD measurement in order to study their magnetic properties.

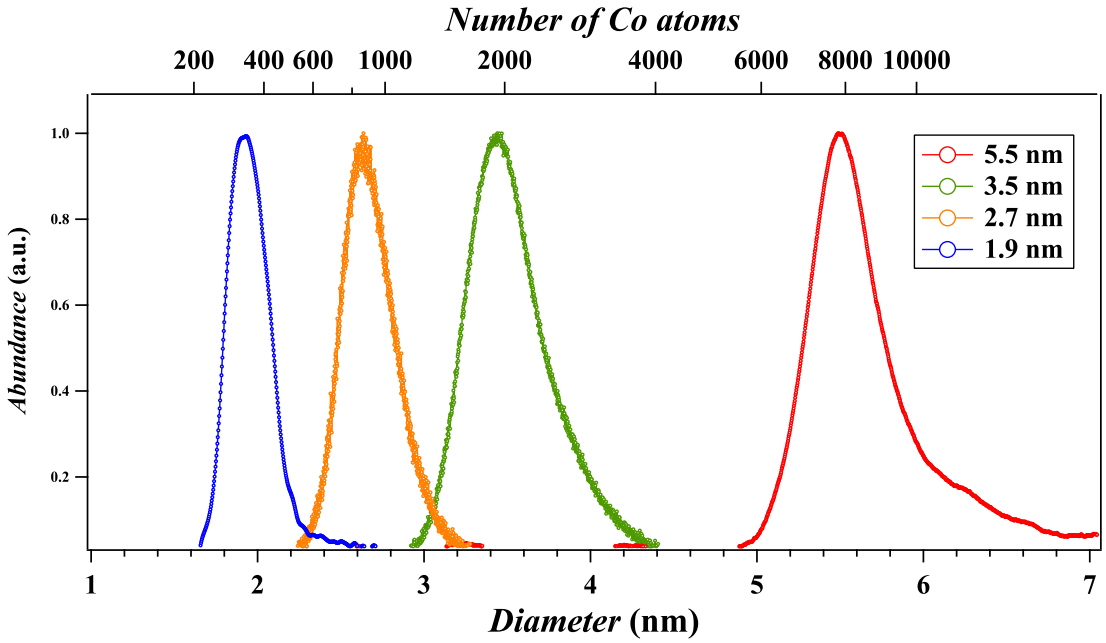

FIG. 35: *TOF-MS spectra of cobalt clusters at different sizes produced by the magnetron cluster source.*

The samples were prepared under the conditions described in **chapter I**. The cluster deposition rate was determined from the ion current measured in-situ in the deposition chamber, on a detector of 0.15 cm^2. In order to avoid magnetic interactions the cluster concentration was decreased below of 0.5%, taking into account the amount of material which gives rise a minimum magnetic signal for SQUID measurements, which is approximately 1×10^{-8}A-m^2, corresponding to 6×10^{14} cobalt atoms. The copper deposition rate was adjusted as a function of the cluster deposition rate under UHV conditions. The values from each sample are displayed in the **Table VI**.

TABLE IV: *Deposition conditions for samples prepared by magnetron sputtering varying the cluster size. The copper deposition rate was adjusted as a function of the cluster deposition rate under UHV conditions. The size distribution was obtained by fitting a log-normal function to the TOF-MS spectra where D_m corresponds to the median diameter and w_m to the size dispersion.*

Sample Name	D_m (nm)	w_m	Co rate (Å/s)	Cu rate (Å/s)	Ion current (pA)	Co % concentration
NTM13-21	1.9	0.07	0.002	0.7	200	0.2
NTM12-12	2.7	0.06	0.005	2.4	100	0.2
NTM12-39	3.5	0.04	0.02	6.0	200	0.3
NTM13-16	5.5	0.04	0.01	6.0	30	0.2

The mean cluster size was determined at the moment of the deposition by TOF-MS, and the corresponding spectra are displayed for the entire set of samples in **Fig 35**. We observe a very sharp size distribution for each size, where the size dispersion w_m, obtained by fitting with a log-normal function, is smaller than 10%.

III.1.1 Results from the Magnetic Characterization

A complete magnetic characterization was performed on the entire set of samples. We started by measuring the magnetization $m(H)$ as function of the magnetic field at different temperatures. At high temperatures the clusters are in the superparamagnetic state and we observe that the magnetization curves at 300 K are arranged by cluster size (**Fig. 36A**), which is agreement with the dependency of the Zeeman energy on the volume of the particles, and the experimental data are well described by a superposition of Langevin functions (**Fig. 40**).

At 2 K most of the particles are in the blocked state, and the magnetization shows a hysteric behavior. In the previous section we introduced the energy barrier, which depends on the volume of the nanoparticles and the anisotropy constant, thus the values obtained for the coercive field H_c will be a combination of both effects. In our samples the ensemble of particles have a size distribution and the critical size for the progressive transition between the two regimes at 2 K is around $\sim$2 nm using **Eq. 24** which depends on the value of K_{eff}. This means that especially for the samples with smaller particles a part of the them will be in the blocked state and others will be superparamagnetic.

For the samples where the mean cluster size are 3.5 nm and 5.5 nm the fraction of superparamagnetic particles at 2 K is negligible and H_c presents a size dependency, but for the sample of 1.9 nm and 2.7 nm the population of superparamagnetic particles ($H_c = 0$ and m_R/m_S=0) becomes important and is estimated in the next section. This indication explains the overlap in the coercive field for the sample of 3.5 nm and 2.7 nm. In a system for particles with uniaxial anisotropy which are all in the blocking state the ratio m_R/m_S between the remanent and the saturation magnetization is 0.5 at a temperature of 0 K [16]. In our case at 2 K for all the samples m_R/m_S is lower than 0.5 and depends on the particles size in agreement with the presence of particles in the superparamagnetic state at 2 K where $m_R = 0$. In **Table V** are presented the values for the coercive field H_c and the ratio m_R/m_S.

TABLE V: *Values for the coercive field H_c, the ratio m_R/m_S and T_{max} for samples with different cluster size.*

Diameter of particles	Cycles 2 K $\mu_0 H_c$ (T)	m_R/m_S	ZFC T_{max} (K)
1.9 nm	0.01	0.15	3.5
2.7 nm	0.03	0.30	9.7
3.5 nm	0.03	0.33	10.7
5.5 nm	0.08	0.38	71.3

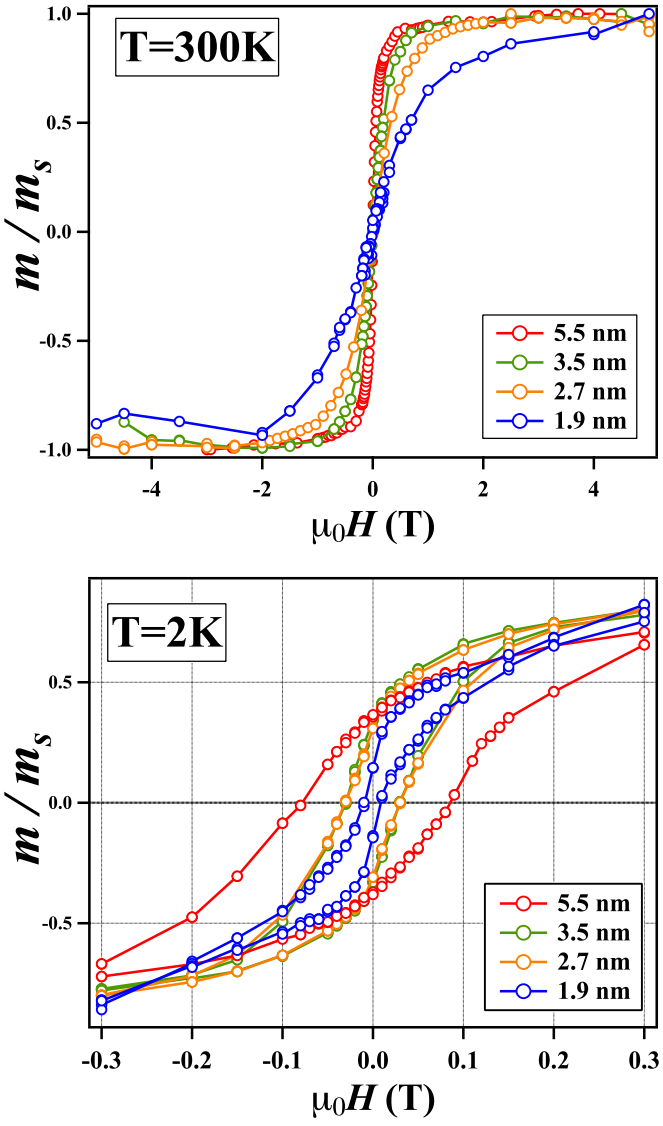

FIG. 36: *Magnetization curves as function of the magnetic field at 300 K and 2 K for samples with different cluster size.*

The ZFC/FC protocol was performed and the susceptibility curves were measured. In **Fig. 37** are displayed the normalized ZFC/FC susceptibility curves, showing the evolution of the T_{max} as function of the cluster size for all four samples.

We observe that T_{max} for the ZFC curves is shifted as a function of the cluster size (**Table V**), varying from 3.5 K for the sample of 1.9 nm up to 71 K for the sample of 5.5 nm. This behavior is in qualitative agreement with the dependency of the blocking temperature on the volume and the magnetic anisotropy of the particles as was presented in the previous section. At this point it is impossible only from the ZFC curves to quantify the influence of the cluster size on the value of the blocking temperature and to determine the magnetic anisotropy as was presented in **chapter II**. Usually the value of T_{max} is used to obtain the value of the anisotropy constant by **Eq. 25** where the size distribution is not taking into account and its value is overestimated [66].

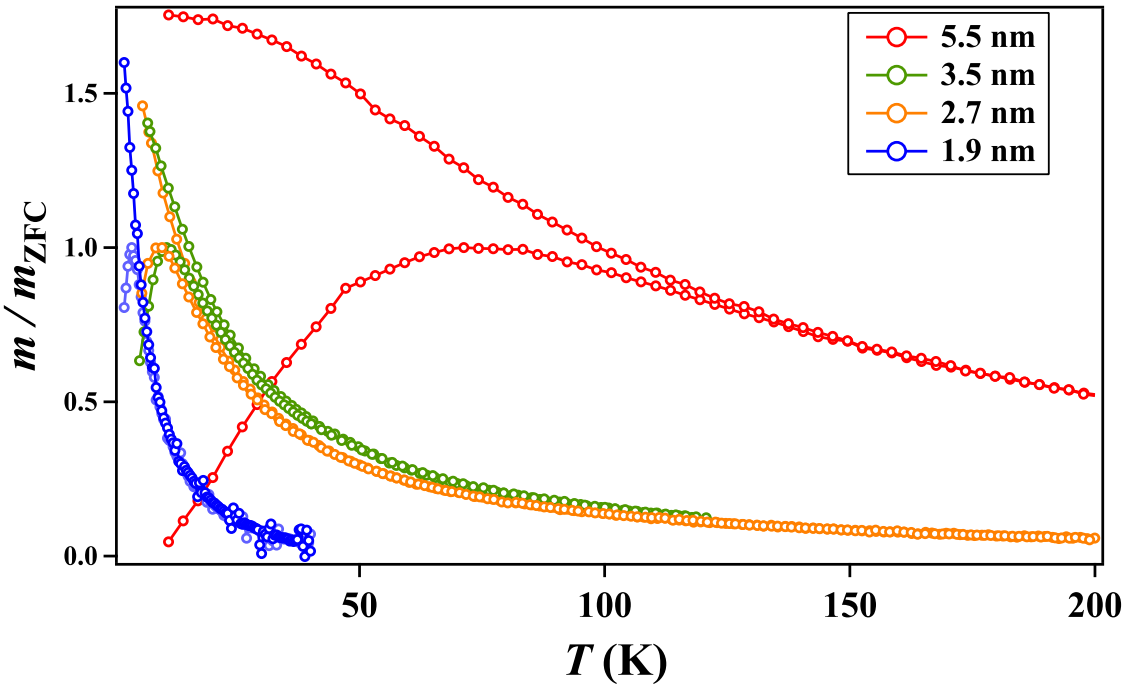

FIG. 37: *Normalized ZFC/FC susceptibility curves for different cluster sizes. T_{max} for the ZFC curves is shifted as a function of the cluster size, varying from 3.5 K for the sample of 1.9 nm up to 71 K for the sample of 5.5 nm.*

In order to study the presence of cluster interactions, IRM/DCD curves were measured and the Δm curve was determined using **Eq. 31**. The values for Δm is at the noise level, except for the sample of 1.9 nm, where a small dip is observed, which represents an additional uncertainty that we need to consider when the data will be analyzed. For the rest of the samples the inter-cluster interactions can be assumed as negligible. Now with this indication we can analyze the magnetic response with respect to the cluster size, assuming interaction-free particles.

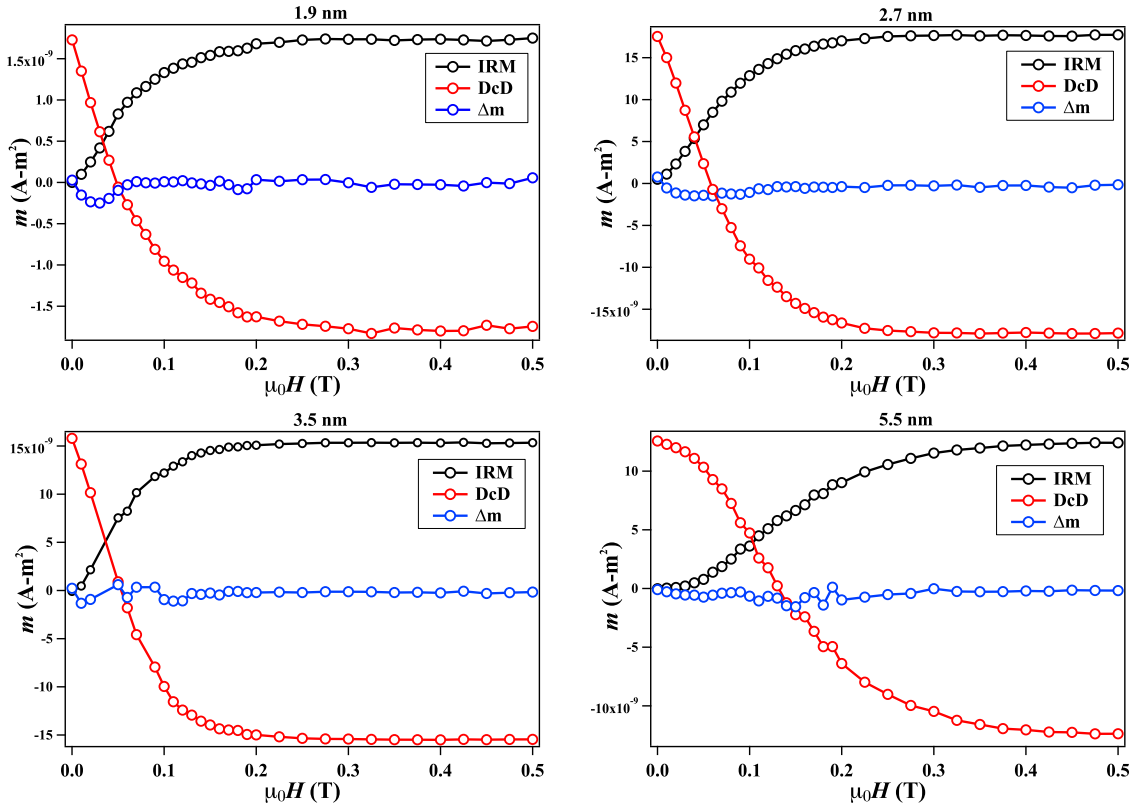

FIG. 38: *IRM/DcD protocol for the set of samples. The values for Δm is at the noise level, except for the sample of 1.9 nm and the inter-cluster interactions can be assumed as negligible*

Plotting the normalized IRM curves for each size (**Fig. 39**), we observe that the effect of the cluster size is not solely responsible for the magnetization reversal process and the slope of the IRM curves do not follow a monotonous cluster size dependency.

The IRM curve is associated to the magnetization reversal process, thus depending on the depth of the potential well, which is determined by the anisotropy constant and the volume of the particles. Using this criterion we can deduce from the IRM curves that the magnetic anisotropy does not follow a monotonous behavior with respect to the cluster size. This is the signature that magnetic anisotropy cannot be considered the same for all samples, and that due to the fact that our samples have been prepared with very sharp size distributions, it is possible to observe a complex size effect of the magnetic properties.

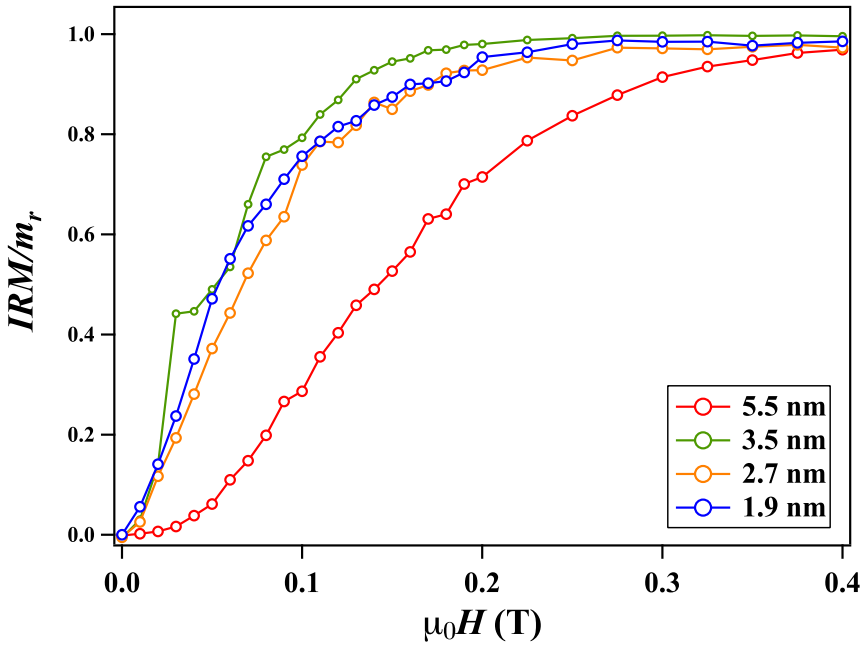

FIG. 39: *Normalized IRM curves for different cluster sizes. The slope of the IRM curves do not follow a monotonous behavior with respect to the cluster size and it is possible to observe a complex size effect of the magnetic properties*

In order to determine the values of the magnetic anisotropy and the size distribution for the ensembles of particles, we performed the triple fit protocol and IRM & m(H) at 2 K simulations, as presented in the next section.

III.1.2 Triple Fit & IRM

We carried out the triple fit protocol considering an anisotropy distribution described by a gaussian function with K_{eff} the mean value and w_K as the anisotropy dispersion and the three curves for each sample were adjusted simultaneously. The obtained values for the median size, the diameter dispersion, the effective anisotropy constant and its dispersion are listed in **Table VI**. The experimental data with the curves from the fit are displayed in **Fig. 40**. Using the same set of parameters obtained from the fit, we simulate the IRM and the $m(H)$ at 2 K curves and compare them to the experimental data.

For the samples of 2.7 nm, 3.5 nm and 5.5 nm it is not possible to reproduce the IRM curves directly with the parameters obtained from the triple fit, and it is necessary to add a second anisotropy term K_2 to the IRM and $m(H)$ at 2 K curves calculation. Using this additional term and the values obtained from the triple fit, the simulations reproduce the experimental with a remarkable agreement. Only for the sample of 1.9 nm it was possible to simulate the data without an additional K_2 term. In **Fig. 41** are displayed the entire sets of experimental data and their corresponding fits and simulations. For each sample are displayed the IRM simulations using only the triple fit parameters and as well as with the second anisotropy term. The parameters obtained for each sample are presented in **Table VI**.

TABLE VI: *Parameters obtained by the Triple fit and IRM simulations for samples with different cluster size.*

	Triple Fit with K_{eff} dispersion				**IRM**
Samples	D_{mag} (nm)	w_{mag}	K_{eff}(kJ/m^3)	w_K	K_2/K_{eff}
1.9 nm	1.9	0.10	218	0.40	0
2.7 nm	2.7	0.20	135	0.40	0.8
3.5 nm	3.2	0.17	110	0.35	1.1
5.5 nm	5.5	0.13	170	0.35	1.2

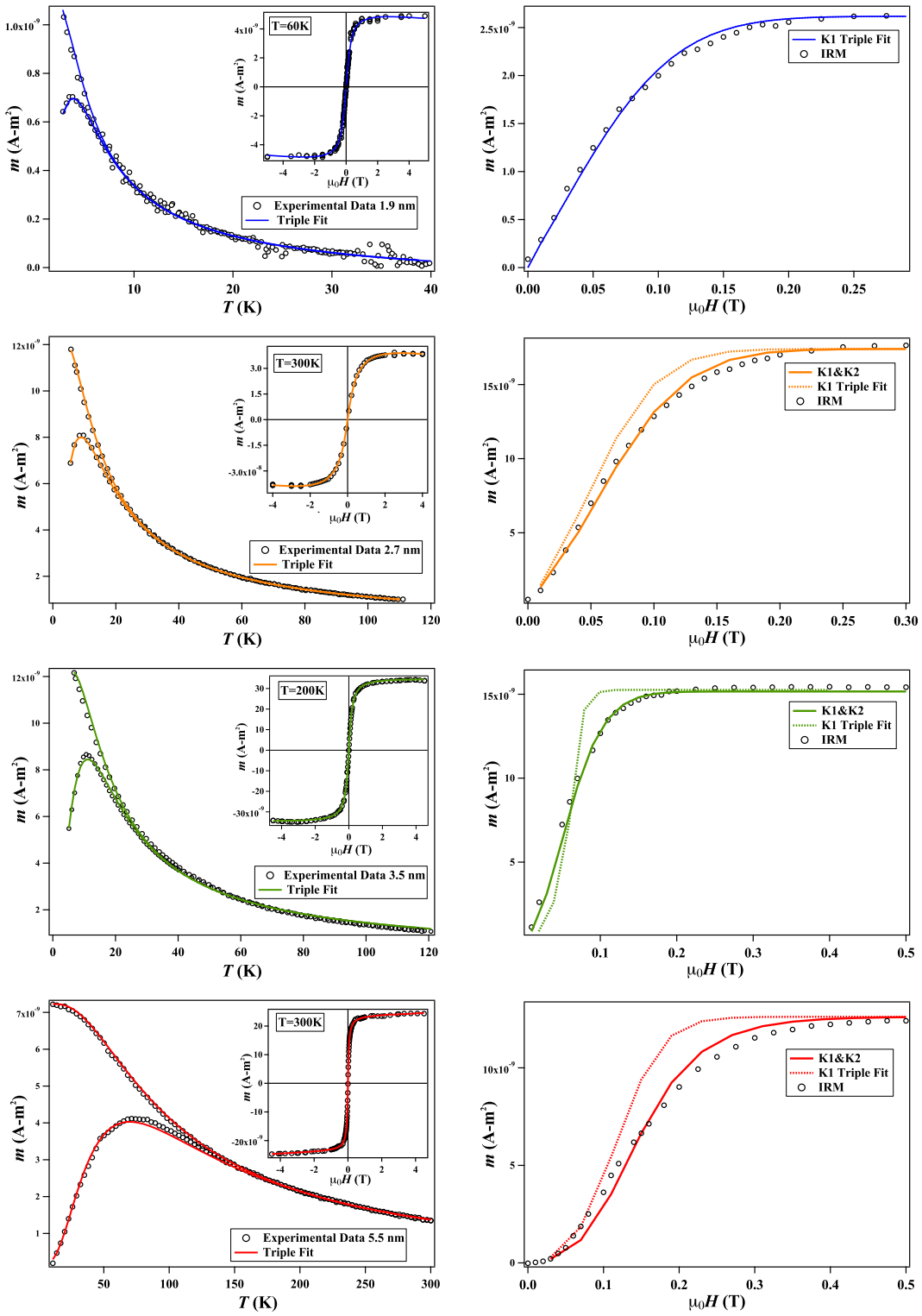

FIG. 40: *Triple Fit results, IRM simulations at 2 K and ZFC/FC curves at 5 mT for samples with different cluster sizes. Left side: points correspond to the experimental data and the lines to triple fit. Right side: point correspond to IRM experimental data and the continuous line to simulations considering biaxial contribution and the dash line uniaxial contribution*

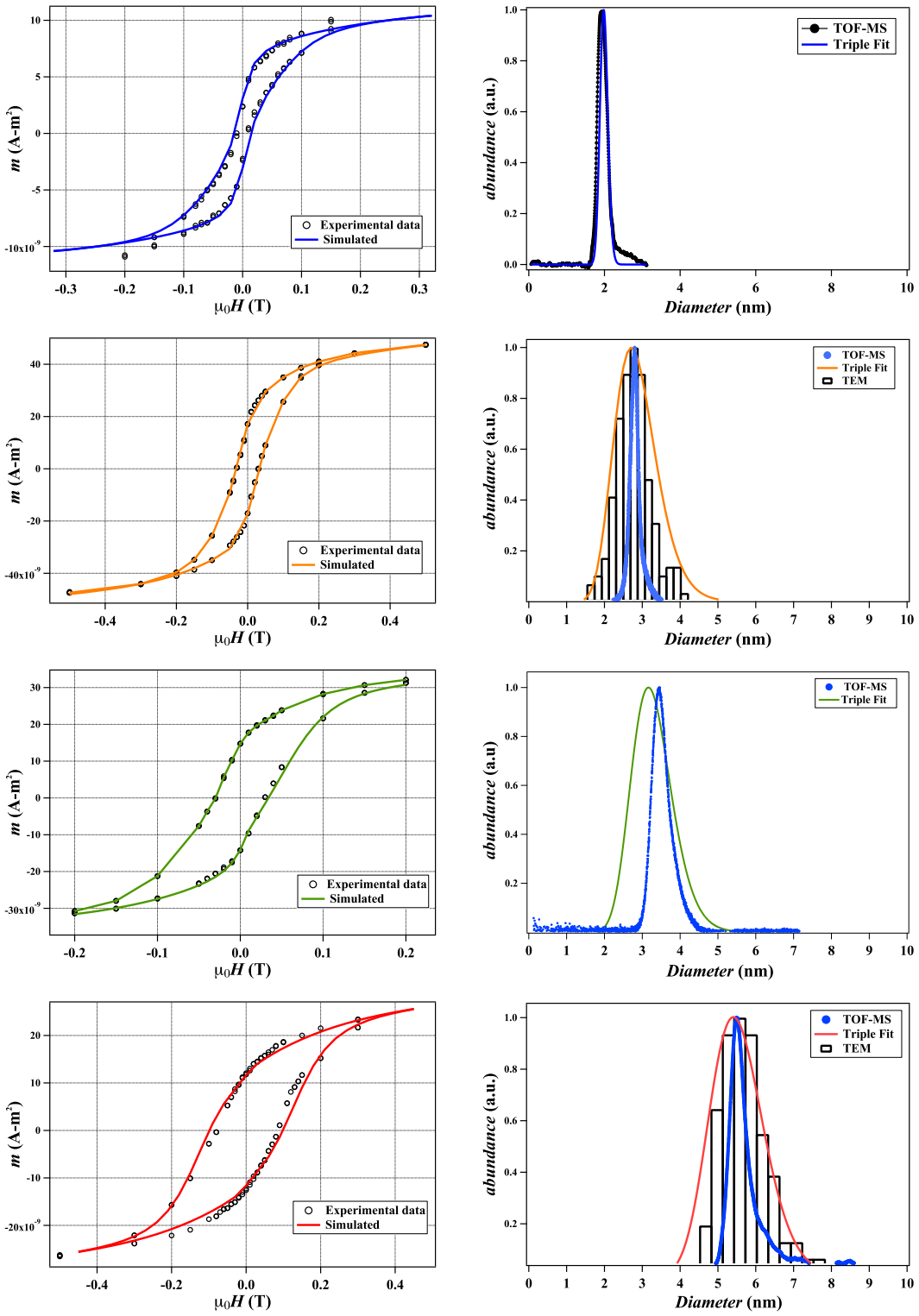

FIG. 41: *Left side: Simulation of the magnetization cycles at 2 K. Right side: magnetic size distribution compared to TEM and TOF-MS.*

In order to reproduce the magnetization cycle at 2 K it is necessary to take into account the cluster size dispersion, thus the signals measured have contributions from superparamagnetic and blocked particles. We simulate the cycle at 2 K as a superposition of two contributions: the superparamagnetic particles described by a Langevin function and the contribution of the blocked particles calculated using the SW model with the parameters obtained from the triple fit and IRM simulations. Each contribution was weighted by the fraction of particles that give rise to the magnetic signal. In **Fig 42** are presented the curves for the samples of 1.9 nm and 2.7 nm. For the rest of the samples the superparamagnetic contribution at 2 K is negligible.

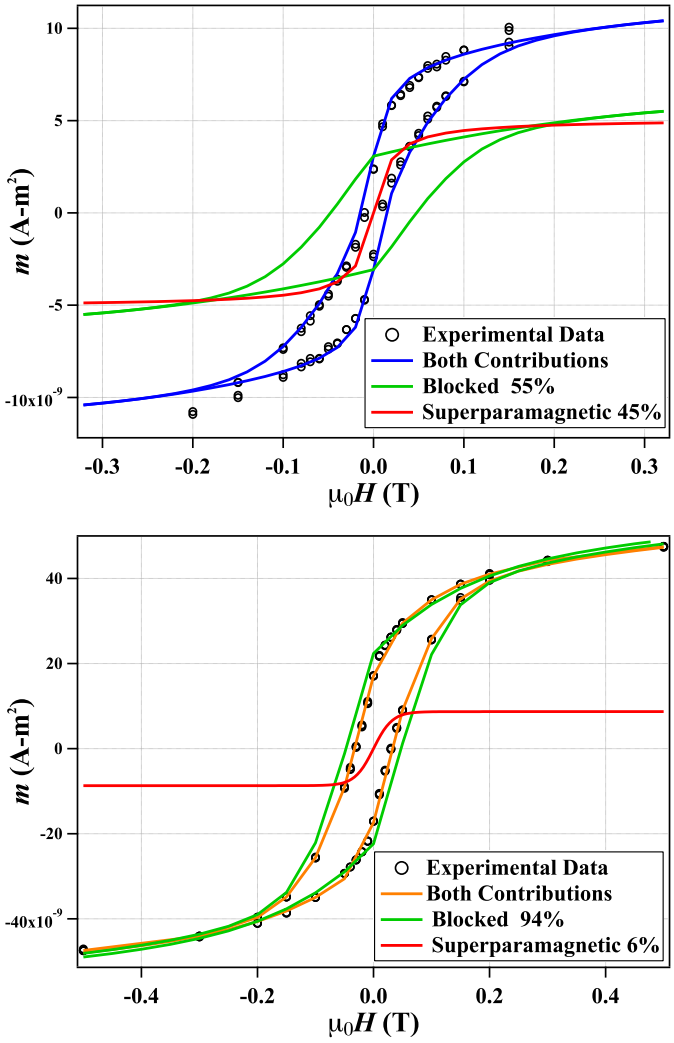

FIG. 42: *Simulated magnetization cycles at 2 K, using the superposition of the contribution from the blocked and superparamagnetic particles.*

We now compare the values obtained from the triple fit with TEM observations and TOF-MS. The three techniques are in agreement with respect to the mean size within the uncertainty of the triple fit method of $\sim 10\%$. Concerning the size dispersion, systematically the TOF-MS shows smaller values than the other two techniques. From prior TEM observation using silver clusters (showing better contrast than cobalt), the results obtained between TOF-MS and TEM are in agreement for the size dispersion. Thus we can assume that the disagreement for TOF-MS comes from the fact that, first of all the poor contrast for cobalt images increase the uncertainly inducing an increment in the size dispersion. The difference between magnetism and TOF-MS could be explained by hybridization of the atomic orbitals at the interface, or the effect of the shape of the particles does not entirely accounted for the anisotropy dispersion. For the three techniques we used a log-normal function to describe the size distribution, and the results obtained are displayed in **Table VII**.

TABLE VII: *Median diameter and dispersion obtained by Triple fit, TOF-MS and TEM for samples with different cluster size.*

	Triple Fit		**TOF-MS**		**TEM**	
Samples	D_{mag} (nm)	w_{mag}	D_m (nm)	w_m	D (nm)	w
1.9 nm	1.9	0.16	1.9	0.07	-	-
2.7 nm	2.7	0.20	2.7	0.06	2.7	0.15
3.5 nm	3.2	0.17	3.5	0.04	-	-
5.5 nm	5.5	0.13	5.5	0.04	5.6	0.10

III.2 DISCUSSION

Plotting the values obtained for the anisotropy constant K_{eff} as a function of the mean size from **Table VI** (**Fig. 43**), we observe that it does not correspond to a monotonous behavior with respect to the cluster size. Thus we need to go further in our study of the nature of magnetic anisotropy.

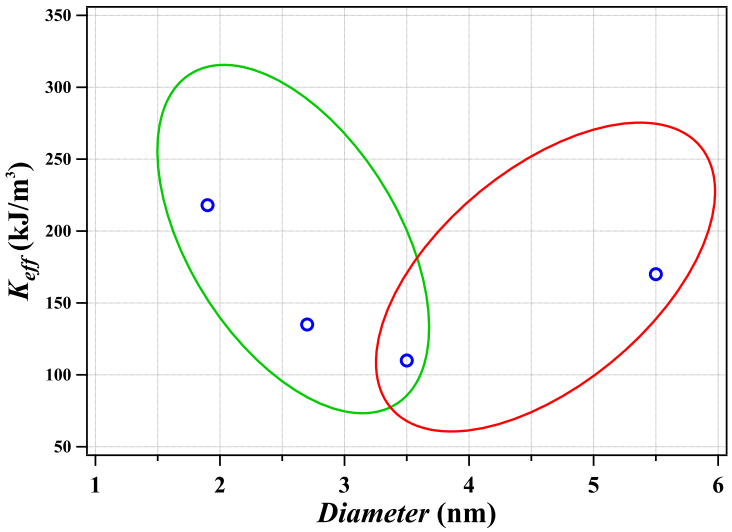

FIG. 43: *Anisotropy constant as function of the cluster size. We observe that the anisotropy constant does not correspond to a monotonous behavior with respect to the cluster size.*

In order to elucidate which source of magnetic anisotropy is responsible for the magnetic properties, we can identify first two regions in **Fig. 43**.

In the region of large clusters where K_{eff} increases as function of the cluster size, we will now show that this is due to the fact that when the particles become bigger their growth is no longer uniform. The elongated shape determines that one of the axes becomes preferential inducing an increment in the magnetic anisotropy by the change in the shape of the particles.

In the second region the magnetic anisotropy increases with decreasing cluster size. When reducing the size of nanoparticles, the number of atoms at the cluster surface increases and their contribution to the magnetic anisotropy becomes more and more important. Thus we assume, in the same way as in previous work [40, 41], that the magnetic anisotropy is determined by the surface anisotropy.

III.2.1 Shape anisotropy

In order to study the influence of the nanoparticle shape, we performed TEM measurements for samples with different cluster sizes. The samples of 2.7 and 5.5 nm correspond to TEM grids prepared at the same time as the samples presented earlier in this chapter. In the case of the sample of 4.5 nm the magnetic results are not unambiguous, for this reason they are not presented in this thesis, but we will use the information extracted from TEM observations. From the TEM images we observe that the shape of the particles is modified as function of the particles size that can be explained by the growth process in the gas phase when one or two primary clusters collide. Prior studies have been shown that large clusters produced in a laser vaporization source result from a coagulation process and are not necessarily spherical. For platinum clusters, a transition from spherical to strongly ramified shapes is observed when the cluster size increases beyond a critical diameter of about 2.5 nm [1].

To analyze the set of images for each sample, we adjusted ellipses to the selected particles and we obtained the length of both axes that describe the ellipse. In order to explore the shape of the particles, we analyze the ratio c/a, between the major and minor semi-axis, known as aspect ratio. Following this protocol it is possible to quantify the evolution of the shape with respect to the cluster size in our experiment. We adjusted a log-normal function in order to describe the aspect ratio histogram for each sample, obtaining the median value for the distribution and the dispersion $w_{c/a}$ (**Table VIII**). We observe that for the sample of 2.7 nm, the ratio of the two axes is close to 1, thus the shape of the particles is closely described by a circle. In the case of bigger particles ($\sim$5 nm), the shape is better described by an ellipse and the ratio of the two axes is around 1.6. Additionally, from the histogram analysis we remark that dispersion increases in function of the cluster size in the same way as the shape varies.

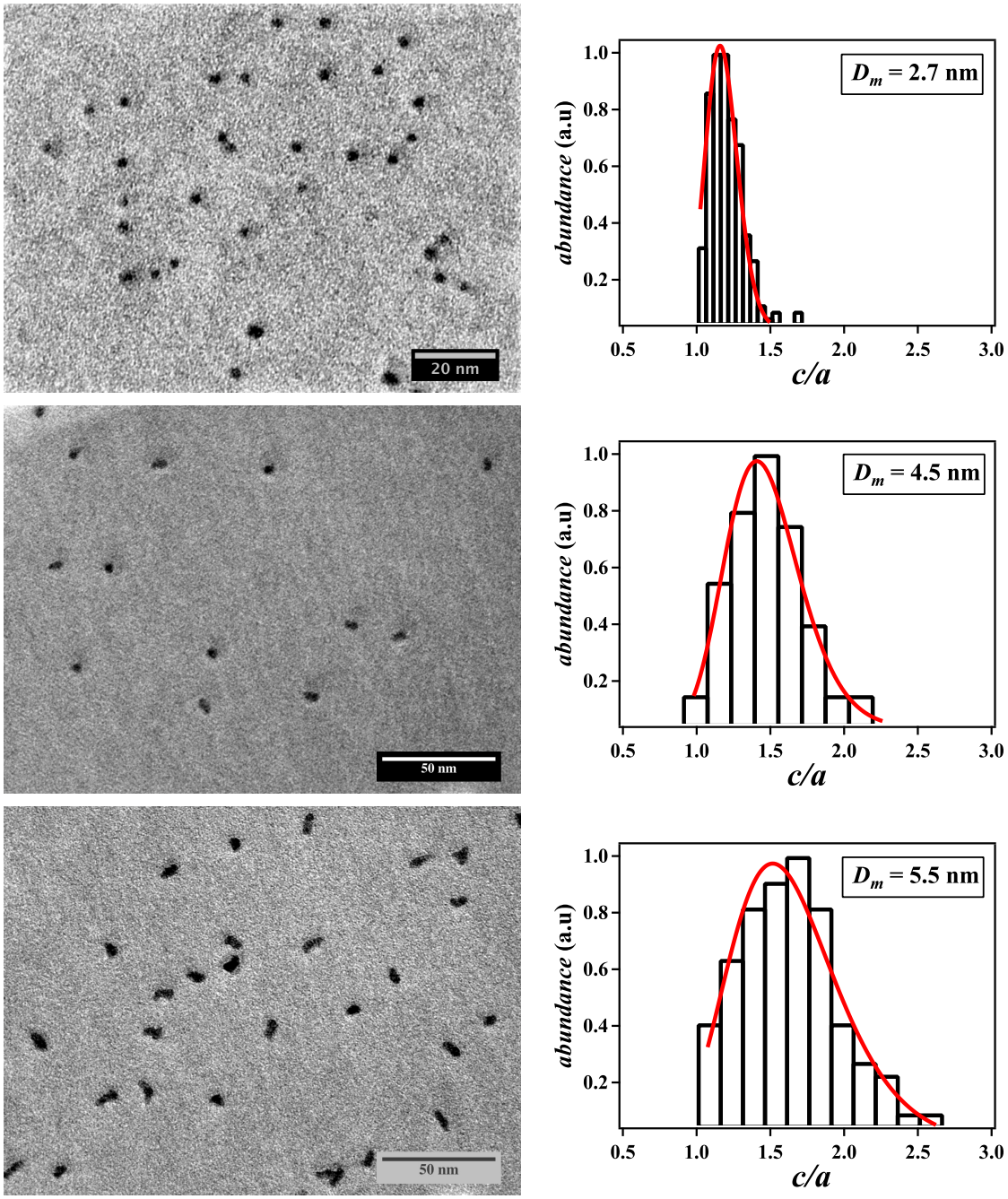

FIG. 44: *Aspect ratio c/a for samples with different cluster size obtained by TEM observations. From the TEM images we observe that the shape of the particles is modified as a function of the particles size.*

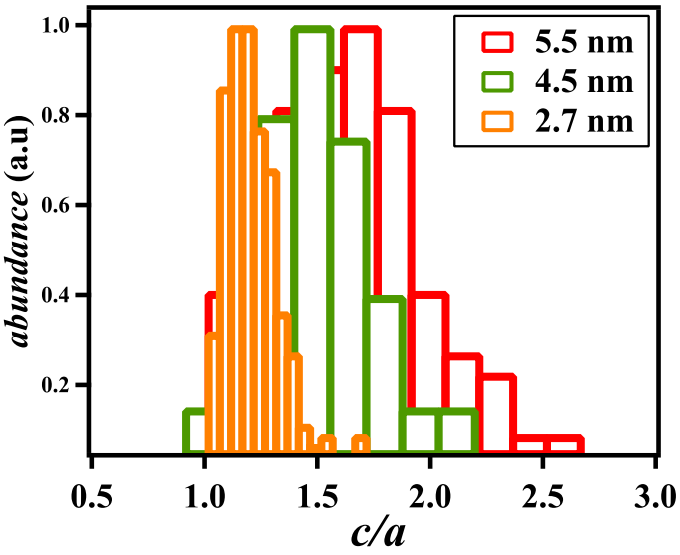

FIG. 45: *PDF of the aspect ratio for samples with different cluster sizes.*

For the samples of 1.9 nm and 3.5 nm, we do not have TEM measurements, thus by extrapolating the obtained values for the rest of the samples we can estimate the values for the aspect ratio and the dispersion. At this point we can quantify the shape of the particles from TEM images, but always keeping in mind that a particle is a tridimensional object and from the image analysis we obtain only the projections of the axes onto the plane of the image.

TABLE VIII: *Median value and dispersion for the aspect ratio (c/a) distributions. The * values were obtained by extrapolating the c/a distributions*

Samples	c/a	$w_{c/a}$
*1.9 nm	1.03	0.05
2.7 nm	1.16	0.09
*3.5 nm	1.24	0.11
4.5 nm	1.45	0.17
5.5 nm	1.60	0.23

Next we calculate the demagnetizing energy for an ellipsoid whose three axes have different values. We assume the three semi-axes in the flowing way:

$$c \geqslant b \geqslant a \geqslant 0$$

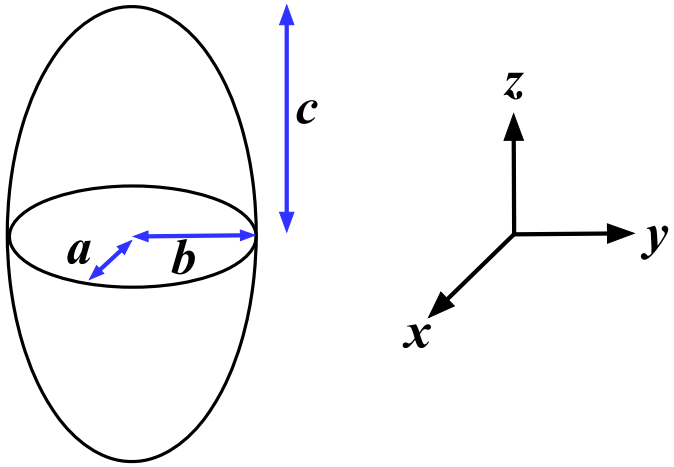

FIG. 46: *Schematic representation of an ellipsoid*

The demagnetizing field is given by $\vec{H}_{dm} = -\mathcal{N}\vec{M}$ and the demagnetizing tensor $\mathcal{N}$ corresponds to a diagonal matrix whose components N_{xx}, N_{yy} and N_{zz} are related to the semi-axes a, b and c.

Using the expression for the demagnetizing energy (**Eq. 16**), and expressing $\vec{M}_s$ in spherical coordinates, the anisotropy energy divided by the volume of the particles is given by:

$$\begin{aligned}
\mathcal{E}_a &= K\sin^2\theta + \mathcal{E}_{dm} \\
&= K\sin^2\theta - \frac{1}{2}\mu_0\vec{M}_s\cdot\vec{H}_{dm} \\
&= K_1\cos^2\theta + K_2\sin^2\theta\sin^2\phi \qquad \text{with} \qquad K_1 < 0 \\
&= K_1 m_z^2 + K_2 m_y^2
\end{aligned} \tag{39}$$

Where

$$\begin{aligned}
K_1 &= -(K + \frac{1}{2}\mu_0 M_s^2[N_{xx} - N_{zz}]) \\
K_2 &= \frac{1}{2}\mu_0 M_s^2[N_{yy} - N_{xx}])
\end{aligned} \tag{40}$$

From this result we observe that for an ellipsoid with its three axes having different values, the magnetic anisotropy is biaxial. Finally we can express K_{eff} by

$$K_{eff} = -(\frac{1}{2}\mu_0 M_s^2[N_{xx} - N_{zz}]) \qquad \text{using} \qquad K_{eff} = K_1 + K \tag{41}$$

Here we focus on the analysis of the influence of the shape on the effective anisotropy constant c and our calculus will be performed by a revolution ellipsoid with $a = b$. In 1945 J.A. Osborn [54] computed the demagnetizing factors (N_{xx}, N_{yy} and N_{zz}), for a general ellipsoid, thus we used these sets of values to calculate K_{eff} in function of the aspect ratio c/a. The values of the K_{eff} obtained as a function of c/a are displayed in the **Fig. 47** together with the K_{eff} values for our samples.

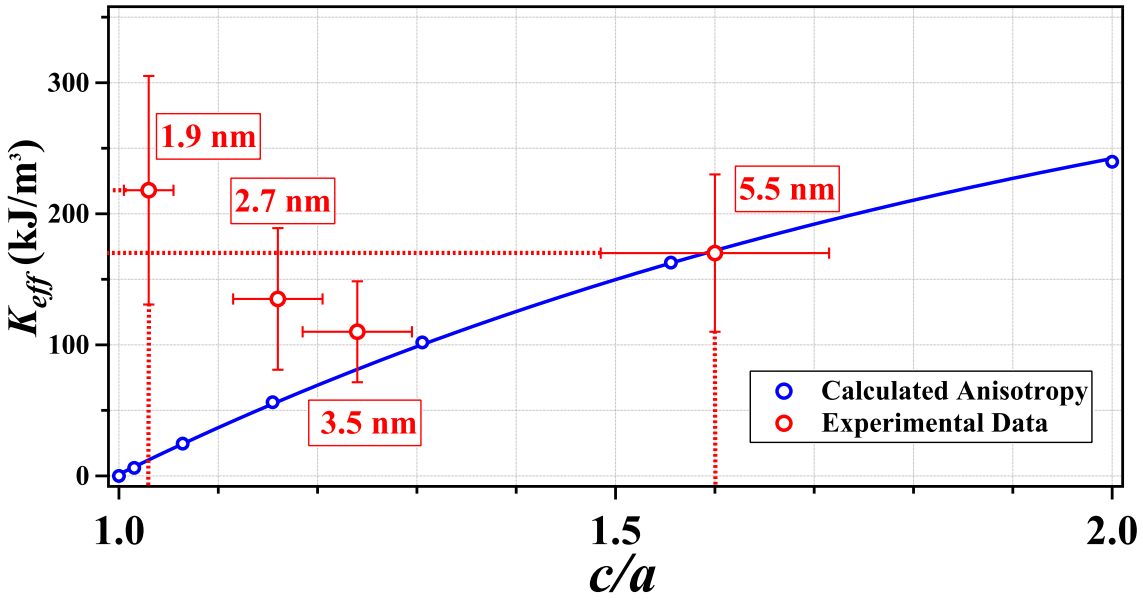

FIG. 47: *Shape anisotropy as function of the aspect ratio c/a. The error bars correspond to the dispersions obtained for K_{eff} from the triple fit and for the c/a distributions from TEM observations.*

From the graph we observe that for the sample of 5.5 nm, using only the contribution of the shape to the anisotropy energy is enough to reproduce the value of the anisotropy constant. In the case of the sample of 2.7 nm, with a value for c/a =1.16, the model predicts an anisotropy constant value of ∼60 kJ/m^3. This result puts in evidence that for smaller sizes an additional mechanism that determines the anisotropy energy is necessary.

We fitted the computed values using an exponential function in order to obtained an analytical expression for K_{eff} with respect to the aspect ratio. The expression that describes the curve is given by:

$$K_{eff} = 393.8 - 1016.4 \exp\left(-\frac{0.951c}{a}\right) \tag{42}$$

In order to simulate the magnetic anisotropy distribution deduced from the Triple Fit, we used the values obtained from the TEM image analysis. First we determined the probability distribution function (PDF) for the anisotropy constant, which was deduced from the PDF for the aspect ratio c/a obtained from the TEM histograms.

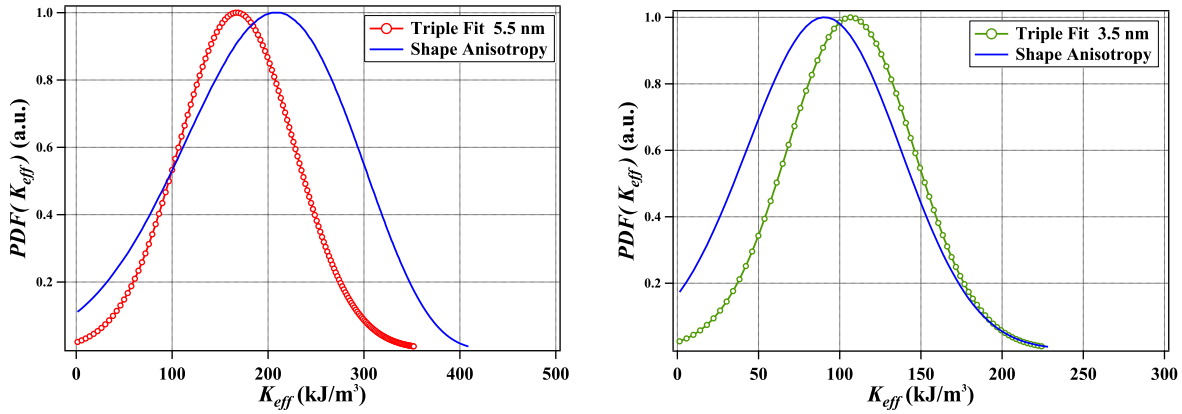

FIG. 48: *Magnetic anisotropy distributions obtained by using the shape anisotropy contrasted with the Triple Fit results.*

We estimated the shape anisotropy for the samples of 3.5 nm and 5.5 nm and we observe that for both samples the mean K_{eff} value is in agreement within around 10% with respect to the values deduced from triple fit. We can conclude that for our samples whose cluster size is in the range between 3.5 nm and 5.5 nm, the shape of the particles dominates and determines the value of the magnetic anisotropy. This result justifies the first hypothesis proposed at the beginning of the discussion and now we will continue in order to elucidate the role of the magnetic anisotropy due the cluster surface.

III.2.2 Surface anisotropy

In order to explore the influence of the cluster surface on the magnetic anisotropy, we will introduce Néel's pair anisotropy model [53] to describe the magnetic anisotropy energy. Taking into account the cylindrical symmetry of the system, the magnetic energy for the interaction of a pair of atoms in this model is given by

$$E = L(\vec{m} \cdot \vec{r})^2 = L \cos \varphi \tag{43}$$

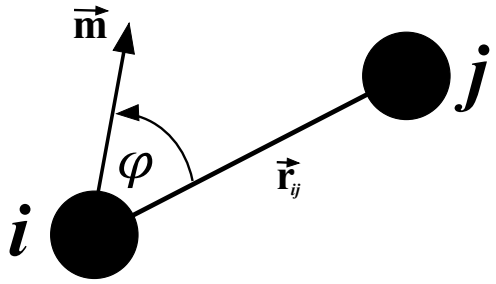

FIG. 49: *Schematic drawing illustrating the Néel pair model; m is a unitary vector in the direction of the magnetization and r corresponds to a vector that relates the two atoms.*

Where m is a unitary vector in the direction of the magnetization and r corresponds to a vector that relates the two atoms. The factor L corresponds to the Néel constant and depends on magnetoelastic constants that in our case was taken as the same as in FCC cobalt [40]. The Néel model is broadly used in thin films to describe the magnetocrystalline surface energy, and we will use it for a cluster nanostructure, summing over all the pair interactions between nearest neighbors in the particle [40]. The atoms located at the center of the particle have the environment of the bulk, thus they do not participate in this anisotropy energy. Assuming that all the magnetic moments of the particles are parallel, we can express the anisotropy energy in a general way by:

$$E = \frac{L}{2} \sum_{i,j} \frac{(\vec{m} \cdot \vec{r}_{ij})^2}{\|r_{ij}\|^2} \tag{44}$$

Where atoms i and j are nearest neighbors. The magnetic anisotropy is a quadratic form of the magnetization, thus it can be diagonalized along eigenvectors $\hat{x}$, $\hat{y}$, $\hat{z}$, and the anisotropy energy divided by the volume of the particles is expressed by:

$$\mathcal{E} = K_1 m_z^2 + K_2 m_y^2 \qquad \text{with} \qquad K_1 < 0 \qquad \text{and} \qquad K_2 > 0 \tag{45}$$

In order to calculate the anisotropy energy using the Néel model, we used the structure of a perfect truncated FCC octahedron, which is in agreement with prior HRTEM observations performed of cobalt nanoparticles produced in our laboratory [41].

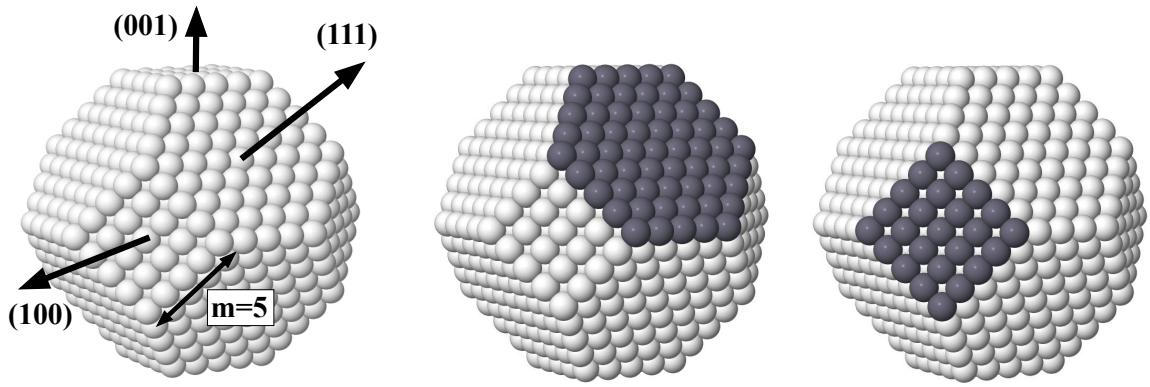

FIG. 50: *Perfect truncated FCC octahedron whose (111) and (001) facets are filled with surface atoms (dark atoms).*

To describe the values obtained for the magnetic anisotropy from the magnetic characterization, the atoms at the surface must be considered as organized and adding a new facet in a defined direction increases the values of the anisotropy constant. In contrast if the atoms are randomly distributed over the cluster surface this results in an anisotropy value (~ 50 kJ/m^3) not large enough compared with the experimental results (220 kJ/m^3) [40]. Adding a single facet does not modify significantly the shape of structure because the resulting cluster keeps an aspect ratio close to 1. The surface magnetocrystalline anisotropy will be zero when all the facets are completely filled.

We performed calculations for the truncated octahedron where its size depends on the value of m, corresponding to the number of atoms between two facets (**Fig. 50**). In **Table IX** are displayed the number of atoms corresponding to different values of m, and the diameter in the case of the truncated octahedron formed by cobalt atoms.

TABLE IX: *Number of atoms and diameter for the truncated octahedron corresponding to different values of m at different cluster sizes.*

m	Number of atoms	Atoms at the surface	D (nm)
3	201	122	1.6
4	586	272	2.4
5	1289	482	3.2
6	2406	752	4.0
7	4033	1082	4.8

In order to compute the magnetic anisotropy of the truncated octahedron, we start by reproducing the values obtained by M. Jamet *et al.* [40] for the magnetic anisotropy with respect to the number of atoms and the added facets.

To study how the magnetic anisotropy varies as a function of additional surface atoms, we started by adding new facets in the direction (001), assuming uniaxial anisotropy. By symmetry, the same results were obtained for directions (010) and (100). We explored doing the same process in the (111) direction and the corresponding symmetries, and the values obtained for the anisotropy constant are three times bigger than the anisotropy values determined by the magnetic characterization.

The increment in magnetic anisotropy is determined only by surface anisotropy by adding a facet while keeping the aspect ratio is close to 1. In this calculation we do not consider the demagnetizing energy excluding the effect of the shape in the anisotropy energy.

We analyzed the structures corresponding to this work of 1.9 nm, 2.7 nm, 3.5 nm and 5.5 nm in diameter whose corresponding value for m are 3, 4, 5 and 7 respectively.

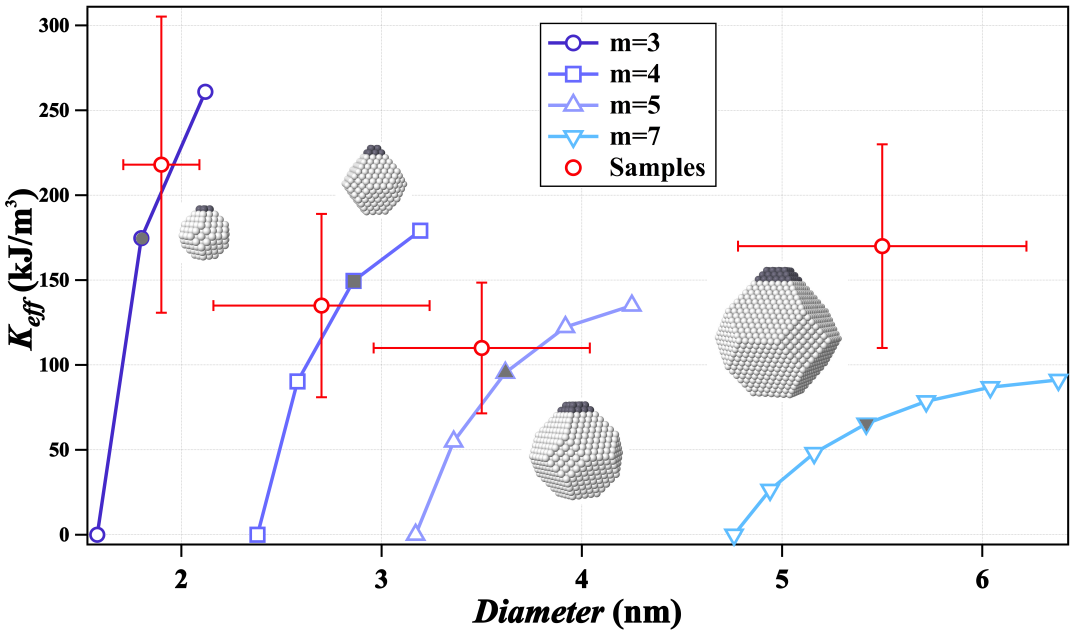

FIG. 51: *Magnetic anisotropy determined using the surface anisotropy at different cluster sizes. The error bars correspond to the dispersions obtained for K_{eff} and the median cluster size from the triple fit.*

For each size we explore a defined region (K_{eff},D) adding facets in one sense in order to obtain the anisotropy values determined by the triple fit. Adding facets on both sides at the same time increases by almost a factor 2 the anisotropy constant [81]. An earlier study using the Néel model considering an icosahedral structure for cobalt nanoparticles estimates values of the anisotropy constant (50-200 kJ/m^3) for particles between 3-4.5 nm [47], which in agreement with values obtained in this work for the same range of sizes.

We can conclude that using the Néel model it is possible to estimate the values for the anisotropy constant for the samples with smaller cluster sizes (1.9-2.7 nm) according to the mean diameter by adding facets. The magnetic anisotropy is determined by the surface magnetocrystalline anisotropy where the shape anisotropy is not large enough compared with the values obtained from the triple fit as was presented in the previous section.

Finally using two different models in order to interpret our results, we can separate the two contributions to the magnetic anisotropy. For smaller particles, where the aspect radio is close to 1, the magnetic anisotropy is controlled by the effect of the surface, whereas for increased cluster size the shape becomes important and is fully responsible of the magnetic anisotropy. We observe that in the case of the sample of 3.5 nm, is possible describe the magnetic properties by the two models, being the transition size between the two regimes.

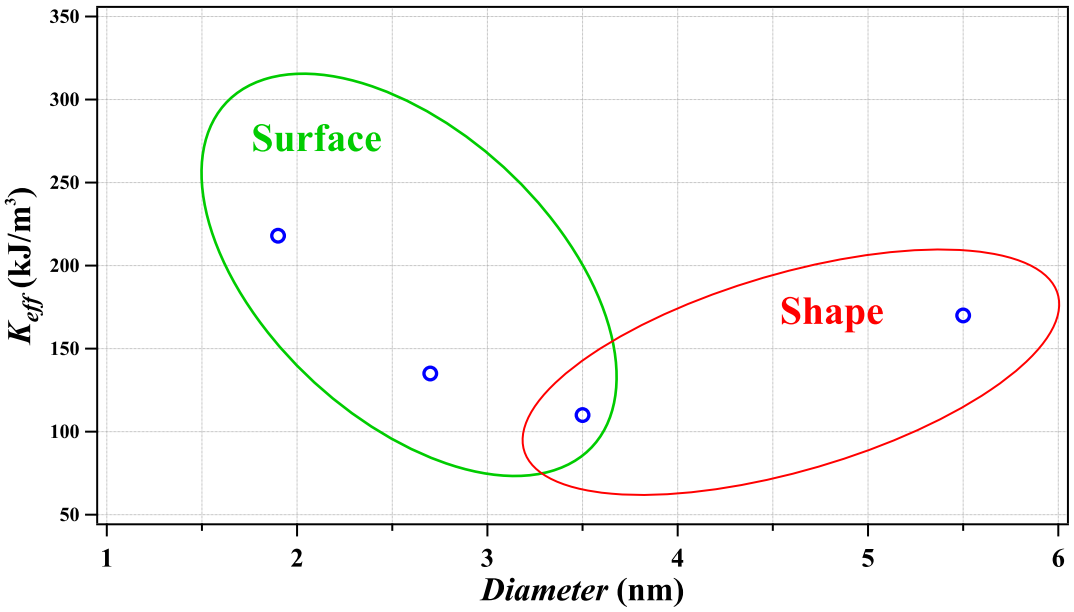

FIG. 52: *Anisotropy constant as function of the cluster size. For smaller particles, where the aspect radio is close to 1, the magnetic anisotropy is controlled by the effect of the surface, whereas for increased cluster size the shape becomes important and is fully responsible of the magnetic anisotropy. We observe that in the case of the sample of 3.5 nm, is possible describe the magnetic properties by the two models, being the transition size between the two regimes.*

III.3 CONCLUSIONS

- We prepared a set of samples with cobalt nanoparticles embedded in copper matrices varying the cluster size between 1.9 nm and 5.5 nm in diameter. The cluster size distributions are very narrow making it possible to study size effects of the magnetic properties.

- We performed a complete magnetic characterization in order to extract the magnetic information from the samples by different experimental techniques. We determined the magnetic anisotropy for each sample, observing a non monotonous behavior as function of the cluster size.

- In order to study the nature of the magnetic anisotropy as a function of the cluster size we analyzed two contributions that determine the magnetic anisotropy; the shape of the cluster and the influence of the cluster surface.

- Using two models to describe the magnetic anisotropy we separated each contribution depending on the cluster size. We demonstrated that for bigger cluster 5.5 nm in diameter the shape of the particles is enough to describe the magnetic anisotropy and for smaller clusters of $\sim$2 nm, where the aspect ratio is close to 1, the magnetic anisotropy is dominated by the surface anisotropy.

chapter IV

Spintronics in granular systems

In this chapter we will expose the transport properties of nanostructures with of cobalt cluster embedded in copper matrices at different cluster concentrations.

We will introduce the different transport coefficients that allow extracting information from the electrical measurements. We study in detail the magnetoresistance (MR) in granular systems where the nanoparticles show a superparamagnetic behavior at low concentrations (0.5%). In order to describe this physical system a complete magnetic characterization was performed allowing to obtain the magnetic cluster size distribution from the triple fit protocol. The IRM/DcD measurements allow to determine the existence of magnetic interactions induced by increases of cluster concentration. The magnetic results were compared with the electrical response in order to have a solid base that allows to study without ambiguity the transport properties in granular systems. Finally the experimental data was analyzed using the Zhang and Levy model [83], that describes the dependence of the resistivity on the magnetic field in a system composed of magnetic nanoparticles immersed in non magnetic matrices.

IV.1 TRANSPORT COEFFICIENTS

IV.1.1 Resistivity

When a current I flows through a metallic sample with homogeneous cross section, the voltage drop measured over the sample is proportional to the current:

$$V = IR$$

Where R is the resistance, that in case of metallic samples depends on the shape of the sample and not on the voltage drop measured or the current flowing through the sample.

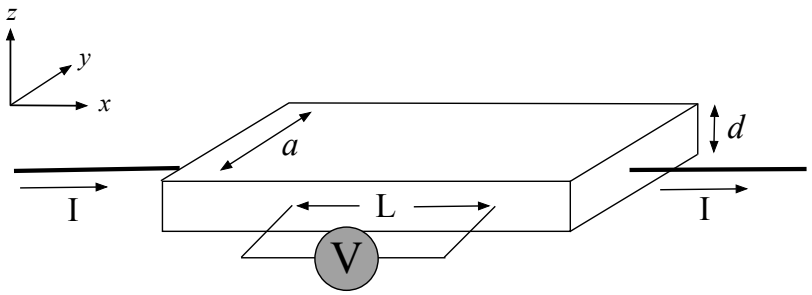

FIG. 53: *Schematic representation of the resistance measurements.*

The resistivity ρ is defined as a coefficient independent of the dimensions of the sample, and is represented by:

$$R = \frac{L}{A}\rho$$

Where L is the distance between the two terminals where the voltage drop is measured and A is the cross section perpendicular to the current flow. The cross section is given by $A = ad$, where a is the width and d is the thickness of the metallic sample.

We can express the relation between the resistivity and the applied electric field $\vec{E}$ and the current density $\vec{j}$ by Ohm's law:

$$\vec{E} = \rho\vec{j}$$

The electric field induces a drift velocity $< v >$ associated with a drift mobility μ_D, expressed by:

$$< \vec{v} >= \mu_D\vec{E}$$

In the Drude Model, the resistivity is given by:

$$\rho = \frac{m^*}{nq^2\tau} = \frac{1}{nq\mu_D} \tag{46}$$

Where τ is the mean collision time, m^* is the effective mass of the electrons in the material, n is the number of the carriers per unit volume and q is the electron charge.

Since the electrons involved in the conduction are moving at the Fermi velocity v_F, the distance that an electron travels on average between two collision events, the mean free path λ is given by

$$\lambda = v_F\tau \tag{47}$$

The statistical independence between the scattering with the vibration of the lattice atoms (phonons) τ_f and any scattering process **independent** of temperature that can be represented by a characteristic time τ_c, leads to:

$$\frac{1}{\tau} = \frac{1}{\tau_c} + \frac{1}{\tau_f}$$

Using the Drude model, we can represent the resistivity for the bulk, by:

$$\rho = \rho_c + \rho_f$$

In this expression ρ_f corresponds to the resistivity due to electron-phonon scattering and ρ_c is the residual resistivity, originated from the interaction of the electron with different localized dispersion sources which are independent of temperature. The additivity of resistivities is know as Matthiessen's rule.

At the macroscopic scale, the resistivity is a quantity intrinsic of the sample, however, in thin films when one or more of the dimensions characterizing the structure are comparable to or smaller than the mean free path λ of the charge carriers, the resistivity will be controlled by *the dominant scattering mechanism*. In thin films we can find scattering mechanisms that increase the value of the resistivity such as grain boundaries, impurities, the roughness of the surface and point defects [49] [33] [34].

IV.1.2 Hall Effect

When we apply a magnetic field B in the $\hat{z}$ direction, perpendicular to the current I flowing in the $\hat{x}$ direction, the effect of the magnetic field is to deflect the electron trajectories due to the Lorentz force. The curvature induces a charge accumulation producing a transverse voltage known as Hall voltage V_H.

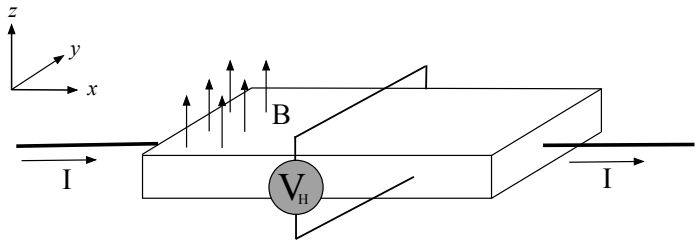

FIG. 54: *Schematic representation of the Hall effect measurements.*

The presence of both fields will induce a drift velocity in response to the Lorentz force on the charge carriers, given by:

$$< \vec{v} >= \mu_D \vec{E} + \mu_D \mu_H \vec{E} \times \vec{B}$$

The Hall field necessary to compensate the transverse component of the drift velocity is:

$$E_H = \mu_H E_x B$$

We can defined the angle θ_H between both components of the electric field, express by the Hall tangent [86]:

$$\tan \theta_H = \frac{E_H}{E_x} = \mu_H B$$

In the Drude model the Hall constant R_H for the bulk is defined by:

$$R_H = \frac{E_y}{j_x B} = \frac{V_H d}{IB} = \frac{1}{nq} \frac{\mu_H}{\mu_D} = R_0 r$$

Where $R_0 = 1/nq$ is the Hall constant for a free electron gas, and $r = \mu_H/\mu_D$, represents the ratio between the mobilities [12, 62].

To describe the electron motion in a metal by the Boltzmann transport equation, using the relaxation-time approximation τ, the mobilities are expressed by [86]:

$$\mu_D = \frac{q}{m^*}\tau$$

and

$$\mu_H = \frac{q}{m}\frac{<\tau^2>}{<\tau>}$$

Where $<\tau>$ represents the mean time over the distribution function. In semiconductors the ratio between the mobilities r is close to 2, but in the case of metals characterized by a spherical Fermi surface, the carriers that participate in electrical conduction are only those located on the Fermi sphere, hence we expect r =1 [12].

When r =1 the relation for the Hall constant leads $R_0 = \frac{V_H d}{IB}$, we can define the normalized V_H^*, by

$$V_H^* = \frac{V_H}{IR_0}$$

and we can obtain the film thickness as the inverse of the slope when we plot :

$$V_H^* = \frac{1}{d}B \tag{48}$$

This expression can be used to measure the sample thickness, and represents a non-destructive technique [35].

IV.1.3 Magnetoresistance in non-magnetic metallic thin films

The percentage change in resistivity due to the action of the magnetic field at a fixed temperature is called **magnetoresistance MR** and can be defined as follows

$$MR = \frac{\Delta\rho}{\rho} = \frac{\rho(B,T) - \rho(0,T)}{\rho(0,T)}$$

In metallic thin films, when we apply a magnetic field B in a defined direction, the magnetic field will deflect the electron trajectories between two scattering events, which means that the frequency at which the charge carriers interact with any scattering mechanism is modified with respect to the absence of B. In non-magnetic thin films the value of the magnetoresistance is positive and increase as a function of the magnetic field but it will depend on the value of the mean free path with respect to the cyclotron radius. For example for a gold thin film, when the scattering is controlled by the surface and the mean free path is around 390 nm at 4K, the ratio between the cyclotron radius and the mean free path is close to 2 and the value of the magnetoresistance rises up to 14% [49, 50] with the magnetic field applied oriented perpendicular to the sample (ordinary transverse magnetoresistance). In thin gold films when the scattering is controlled by grain boundaries, the mean free path is around 50 nm at 2 K and the ratio between the cyclotron radius and the mean free path is close to 20, thus the ordinary transverse magnetoresistance is zero. This experimental evidence indicates that decreasing the mean collision time with structural defects reduces the curvature induced by the magnetic field on the electron trajectory between scattering events, thereby decreasing the magnetoresistance until it eventually falls below the noise level [33].

IV.1.4 Magnetoresistance in ferromagnetic thin films

In ferromagnetic materials like cobalt, nickel and iron the magnetoresistance will depend on the relative orientation between the magnetization and the current flow. When the magnetic moments are aligned in a certain direction, the conductance will have a variation between the perpendicular and parallel direction with respect to the current in the sample, and this effect is called Anisotropic Magnetoresistance (AMR) [69]. The origin of the AMR is related to the coupling of the magnetic moment to spatial degrees of freedom, due to spin-orbit interaction, where the mean collision time depends on the direction of the local magnetization with respect to the current [28].

IV.1.5 Magnetoresistance in magnetic multilayered systems

The "giant" magnetoresistance (GMR) was observed in multilayered systems independently by the groups of Peter Grünberg [10] and Albert Fert [5]. The effect of the magnetic field reduces the value of the resistivity by around 50% with respect to zero field at 4.2 K. The system is composed of an alternating stack of thin magnetic and non-magnetic layers whose thickness is around a few nanometers (Fe/Cr/Fe trilayers [10] and Fe/Cr superlattices [5]). The variation in the resistivity depends on the coupling between the magnetic layers induced by the magnetic field. The GMR was observed when at zero magnetic field the Fe layers are coupled antiferromagnetically via the Cr layer. The resistivity decreases in an applied field as the antiferromagnetically coupled Fe layers (in zero field) align ferromagnetically at high magnetic fields. The variation in the resistivity was one order of magnitude greater than for single Fe films showing the "giant" behavior. The origin of the GMR comes from the link between magnetism and electrical currents. A simple explanation for the GMR can be done based on the two-current model proposed by Mott [48]. In the Mott model the current is carried in separate spin-up and spin-down channels. For non-magnetic materials the current is identical for both channels, while for ferromagnetic materials the current flow is unbalanced between the spin channels and the current becomes spin-polarized.

The difference in the spin density is produced by the exchange interactions that shift the spin-up and spin-down bands and give rise to the ferromagnetic moment [25]. The d-band splits and consequently the density of states (DOS) at the Fermi

energy is different for spin-up and spin-down carriers.

A model proposed by Fert and Campbell [23, 24] explains the magneto-transport in ferromagnetic materials and provides the basis for understanding GMR. The current flows through the two magnetic layers separated by a thin non-magnetic spacer: it current becomes spin-polarized by transmission through the first magnetic layer. If the spacer layer is thin enough, the current maintains its polarization as it passes through the non-magnetic spacer and interacts with the second ferromagnetic layer. This interaction leads to a change of resistance depending on the **relative orientation** of the magnetic layers. If the layer magnetization are parallel, the spin-polarized current flows more easily into the second ferromagnetic layer. As the angle between the magnetizations increases, there is an increasing resistance resulting from spin-dependent scattering.

IV.1.6 Magnetoresistance in granular systems

The system presented in this work is composed of cobalt nanoparticles embedded in non magnetic copper matrices. Cobalt nanoparticles below 10 nm act like a single domain and we can represent the total magnetic moment by a single vector or macrospin as was discussed in **chapter II**. At zero magnetic field the macrospins of an ensemble with random easy axes will be randomly oriented and the magnetization is null.

In a similar way as in multilayer systems the effect of the magnetic field reduces the value of the resistivity of the sample. The current at zero magnetic field is equally shared between the spin-up and spin-down channels and the probability to be scattered will be identical. The presence of a magnetic field defines a quantization axis and each macrospin will try to align parallel to the magnetic field. A macrospin in the electron path will polarize the electron current as parallel or antiparallel to the particle magnetic moment. Now when electron current scatters from a second magnetic particle oriented in a different direction with respect to the first one, for one spin-channel it will more *easy* to pass than for the other, and the resistivity decreases. The variation in the resistivity will depend on the relative orientation of the magnetization axes of the nanoparticles.

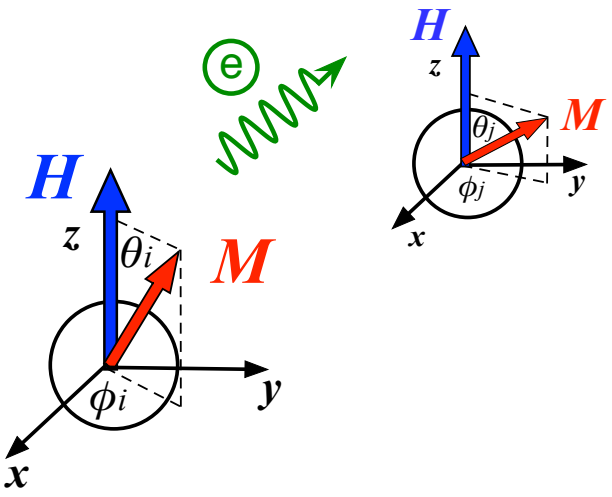

FIG. 55: *Schematic representation of two clusters at different magnetization orientations. The angle θ_i represents the tilt between each magnetic moment and the field axis (z axis), ϕ_i is the angle of twist.*

We can qualitatively describe the dependence of the resistivity with respect to the magnetization in the presence of a magnetic field by the picture of two subsequent magnetic particles in the electron path. The resistivity will be composed of the resistivity at zero field ρ_0 and the effect of the relative orientation of two subsequent moments. The angle θ_i represents the tilt between each magnetic moment and the field axis (z axis), ϕ_i is the angle of twist, and we assume that both angles are statistically independent.

$$\rho = \rho_0 - k < \vec{\mu_i} \cdot \vec{\mu_j} >$$

$$\begin{aligned} < \vec{\mu_i} \cdot \vec{\mu_j} > &= < \cos\phi_i \sin\theta_i \cos\phi_j \sin\theta_j + \sin\phi_i \sin\theta_i \sin\phi_j \sin\theta_j + \cos\theta_i \cos\theta_j > \\ &= < \cos\theta_i >< \cos\theta_j > + < \sin\theta_i \sin\theta_j (\cos(\phi_j - \phi_i)) > \\ &= < \cos\theta_i >< \cos\theta_j > + < \sin\theta_i >< \sin\theta_j >< \cos(\phi_j - \phi_i) > \\ &= < \cos\theta >^2 + < \sin\theta >^2 < \cos(\phi_j - \phi_i) > \end{aligned}$$

The current measures and averages over the relative orientations of subsequent moments. If and only if the two are decoupled, $< \cos(\phi_j - \phi_i) >= 0$ [2, 29], we obtain the MR as proportional to the square of the mean cosine with respect to the external field axis, *i.e.* the square of the mean magnetization.

$$\rho = \rho_0 - k < m_z >^2 \tag{49}$$

IV.2 OVERVIEW

In the last years since the discovery of the giant magnetoresistance (GMR) in multilayer systems [5, 10], spintronics has become an important research subject for fundamental studies and different applications have been developed such as magnetic recording head in hard drives using the GMR effect [79]. In parallel cluster assembled-nanostructures show interesting properties such as superparamagnetism [8, 45] and their potential application in high density storage devices [58, 61]. The mixture of these two main topics, that means spin-dependent transport in granular systems has been studied in the last years but it is still fragmentary.

Granular systems correspond to magnetic nanoparticles embedded in non magnetic matrices where the central idea is to study the interaction between the conduction electrons with the localized magnetic moments by spin-dependent scattering. Granular systems nowadays offer the possibility to vary the physical properties via different parameters such as the mean cluster size or the cluster concentration. Additionally, the electrical response depends on the density of the magnetic material and not on the amount of magnetic material that give rise a magnetic signal for SQUID measurements, making it possible to study samples of only a few nanometers thickness.

GMR in granular systems was observed only a few years after of the discovery of GMR in magnetic multilayer systems and samples were constituted of annealed Co/Cu alloys [9, 80]. The experimental results show GMR values between 20% and 75% with Co concentrations up to 30%. The GMR shows a dependence with respect to the magnetization of the sample described by a quadratic behavior ($MR \propto (M/M_s)^2$) [29]. This relation seems correct but can be used only when there are no correlations between the particle magnetic moments [2]. A theoretical model derived using a formalism for thin films was developed by Zhang and Levy [83] in order to describe the MR for non interacting particles as function of the magnetization.

In the Zhang and Levy model the spin-dependent scattering is due to the interaction between the conduction electrons and the magnetization at the interface between the nanoparticles and the matrix and the spin-dependent scattering within the particles. The scattering mechanism that dominates the transport properties is not yet determined and the question is still open. A few works show contradictory conclusions about the role of the interface or the volume in the scattering process. Rubin *et al.* [60] have shown that the interface dominates as scattering mechanism, observing a dependency of the MR on the inverse particle diameter. A few works have used the Zhang and Levy model to reproduce the experimental data e.g. Ferrari *et al.* [22] conclude that to reproduce the MR experimental data it is necessary to consider both contributions while Parent *et al.* [55] consider only the effect of the interface assuming the volume contribution negligible. In all these works the cluster concentration is equal or more than 10%, meaning that cluster interactions are not negligible, making it impossible to consider the system non interacting and thus to extract reliable information about each contribution to the Zhang and Levy model. This means that inter-particle interactions violate the commonly used assumptions twice, once in the superparamagnetic assumption of the magnetic behavior (magnetization proportional to a superposition of Langevin curves) and again in the connection between magnetic and spintronic response ($MR \propto (M/M_s)^2$).

In order to perform fundamental studies in granular systems is it necessary to have well-defined samples where the electrical response can be attributed to the effect of the magnetization of non interacting nanoparticles on the electrical current. For this it is mandatory that magnetic interactions between the particles must be negligible, assuring no correlations between the local magnetic moments. Previous studies of magnetic properties in cobalt nanoparticles show magnetic interactions even at very low concentration ($\sim$ 3% vol.) [38] where the system cannot be described as superparamagnetic. The first step to study the transport properties in granular systems is to start with highly diluted samples ($\sim$ 0.5%) and to perform a complete magnetic characterization using the set of measurements and data treatment described in **chapter II**. This protocol allows us to have a solid base in order to compare with the electrical response and thus go further to study extraordinary Hall Effect [51], spin transfer torque [59, 75] or spin caloritronics [7].

IV.3 EXPERIMENTAL SETUP

IV.3.1 Sample Preparation

At the beginning of this thesis the magnetron source was not working in order to obtain reliable results, for this reason, the samples for electrical measurements were prepared from preformed gas-phase clusters following the low-energy cluster beam deposition technique (LECBD) [57]. Metal clusters are produced in a laser vaporization-gas condensation source. The plasma is created by the impact of a Nd:YAG (yttrium aluminum garnet) laser beam focused on a Co rod, and thermalized by injection of a continuous flow of helium at low pressure inducing the cluster growth. Next, the clusters are cooled down in a supersonic expansion at the exit nozzle of the source. The obtained low-energy cluster beam is then co-deposited together with the atomic beam for the matrix under ultrahigh-vacuum conditions (10^{-10} mbar static pressure, 10^{-8}mbar He during deposition). The diameter Probability Density Function (PDF) of the deposited clusters, as deduced from earlier transmission electron microscopy observations, closely follows a log-normal curve with a fairly sharp dispersion (described by the standard deviation w) and typical median sizes D_m around 2 to 4 nm, depending on the source conditions.

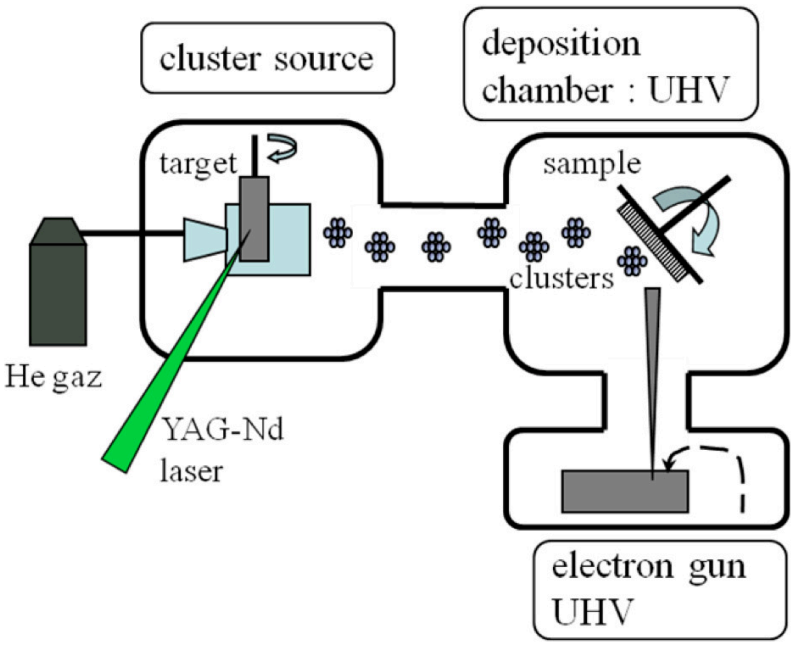

FIG. 56: *Schematic overview of the laser vaporization-gas condensation source.*

The samples discussed here consist of cobalt clusters embedded in copper matrices. By comparing electron microscopy of carbon covered cobalt clusters and the magnetic response of a sample with Co clusters dispersed in a copper matrix prepared at the same time we have verified that the obtained size distributions are nearly the same and that copper forms a neat interface with the embedded clusters [37], just as Au and Ag [67]. The geometric and magnetic diameters are thus interchangeable in this case. Our codeposition technique protects metal clusters from oxidation and allows us to independently adjust chemical composition, cluster size and concentration. We use slightly conducting Kapton foil (Kapton XC, Goodfellow) as substrate material for transport measurements, which allows bypassing nano-or microcracks in the sample without perturbing the overall response. The substrates consist of pre-cut, 6 terminal Hall crosses that allow four point measurements. The **Fig. 57** shows a comparison between the geometric size distribution of carbon covered Co clusters and the magnetic size distribution of the same clusters embedded in a copper matrix. The good agreement indicates a neat interface between cobalt and copper and no interface alloying or magnetically dead layer is observed.

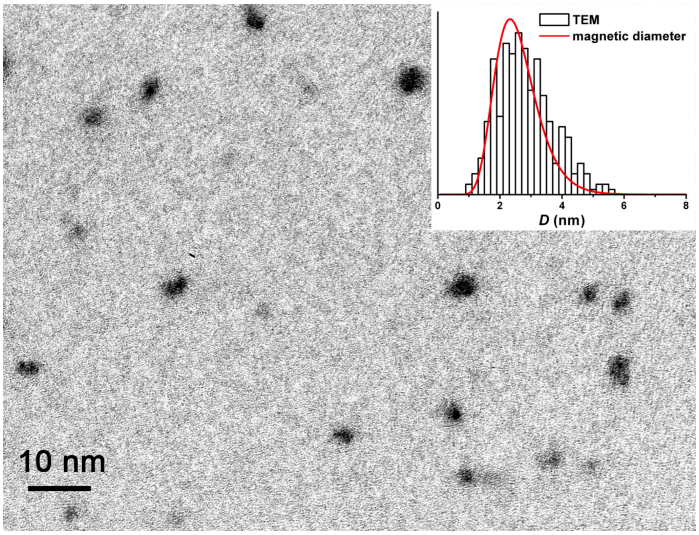

FIG. 57: *TEM image of cobalt clusters produced by laser vaporization-gas condensation source. Comparison between the size distributions derived from TEM (histogram) and the triple fit (red curve).*

IV.3.2 Transport measurements

For transport measurement we used the MPMS-XLS system, but in this case only like a cryostat, where we measured the resistance of the sample under a magnetic field and at different temperatures. The dimensions of the sample are displayed in **Fig. 58**.

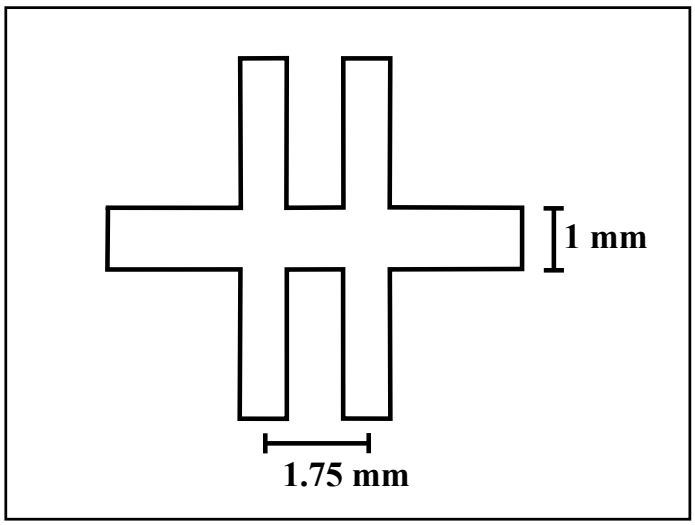

FIG. 58: *Dimensions of the sample used for transport measurements.*

We used a Keithley current source model 6220 DC and Keithley nanovoltmeter model 2182 in the Delta configuration. This configuration uses the current source in the AC mode synchronized with nanovoltmeter avoiding contact potentials in the entire circuit. This configuration provides pseudo-lock-in measurements with the necessary signal to noise ration of better than 10^5.

For the magnetoresistance measurements, we fed the sample with current typical values between 1 mA up to 10 mA between the terminals 1-2 and we measured the voltage drop between the terminals 3-4.

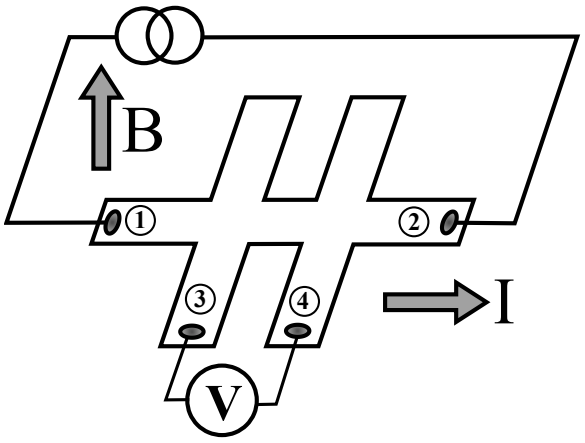

FIG. 59: *Representation of the Magnetoresistance measurements.*

For Hall Effect measurements, we used a potentiometer in order to compensate a possible misalignment between the terminals 4-5. We fed the sample by the terminal 1-2 and we measure the voltage drop between the terminal 5 and 6. The terminal 6 corresponds to the position when the terminal 4 and 5 are at the same potential.

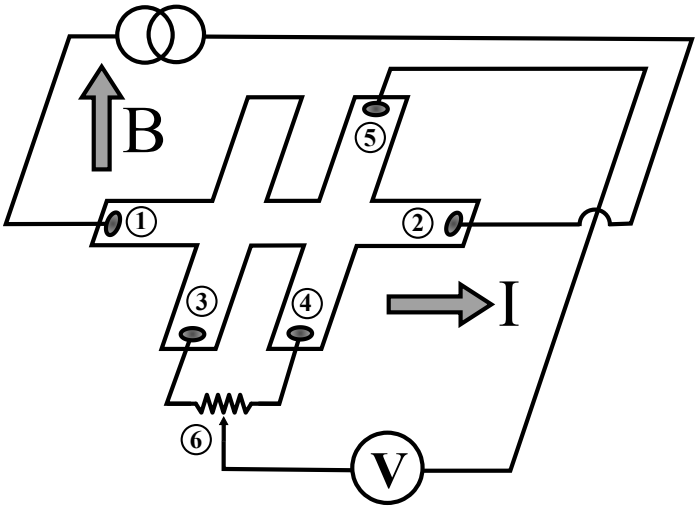

FIG. 60: *Representation of Hall Effect measurements.*

IV.4 RESULTS

In this section we present the results for a set of samples prepared by LECBD. The samples consist of cobalt nanoparticles embedded in copper matrices, where the mean particle diameter is around 2-3 nm and the cluster concentration was varied from 0.5% to 5%. The samples were prepared in order to study the effect of the cluster concentration in magnetic and transport properties. The samples were characterized by conventional magnetic measurements (ZFC/FC and m(H)) which we adjusted simultaneously by the triple fit protocol. Furthermore we performed IRM/DcD measurements in order to detect cluster interactions produced by increasing the cluster concentration.

We measured the magnetoresistance at different temperatures over the samples and the spintronic response is compared to the Zhang and Levy model. The transport and magnetic results were contrasted for a truly superparamagnetic sample, corresponding to a necessary condition to verify the Zhang and Levy model.

IV.5 SAMPLE PREPARATION

We prepared a set of samples with the same cluster mean size and at different concentrations, 0.5%, 2.5% and 5% of cobalt nanoparticles embedded in copper matrices and one sample only a copper thin film (0%). The concentration of the nanoparticles was controlled by the deposition rate for the copper matrix, keeping the clusters rate constant. The samples were prepared at room temperature and in each deposition two twin samples on different substrates were obtained assuring the same preparation conditions. We used as substrates silicon wafers for magnetic measurement and Kapton foils for electrical measurements.

The cluster source conditions were identical for the entire set of samples, producing equivalent cluster size distributions for all the samples.

TABLE X: *Deposition conditions for samples prepared in the laser vaporization-gas condensation source.*

Sample Name	Sample Concentration % Vol.	Cu rate (nm/min)	Co rate (nm/min)	Microbalance Thickness (nm)
NT11-43	0	0.8	-	100
NT12-01	0.5	4.2	0.021	151
NT12-04	2.5	0.8	0.021	78
NT12-02	5	0.4	0.021	53

The cluster mean size and the size dispersion was deduced from earlier transmission electron microscopy observations. The size distribution is describe by a log-normal curve with typical median sizes around 2 to 4 nm.

IV.6 RESULTS FROM MAGNETIC CHARACTERIZATION

IV.6.1 Magnetic measurements

All the magnetic measurements were performed in a SQUID magnetometer, were the temperature can be varied from 2 K up 300 K and the magnetic field between -5 T and 5 T. We performed a set of conventional measurements which consists of the zero field cooled and the field cooled (ZFC/FC) susceptibility curves as well as the magnetization cycles at high temperature where the particles are in the superparamagnetic state. To investigate the presence of interactions we performed the Isothermal Remanent Magnetization (IRM) and the Dc Demagnetization (DcD) measurements where the difference of the two curves is extremely sensitive to interactions.

First of all we verified that the magnetic measurements for both substrates (Kapton and Si) are consistent for the entire set of samples. This verification is extremely important because it allows to work with Kapton as substrate in order to study magnetic and transport properties in the same sample. From previous studies performed in our group, Si substrates are well characterized and the magnetic results are consistent with different techniques [37]. In **Fig. 61** are displayed the ZFC/FC curves and the magnetization curve at 300 K for the samples of 0.5% concentration for different substrates.

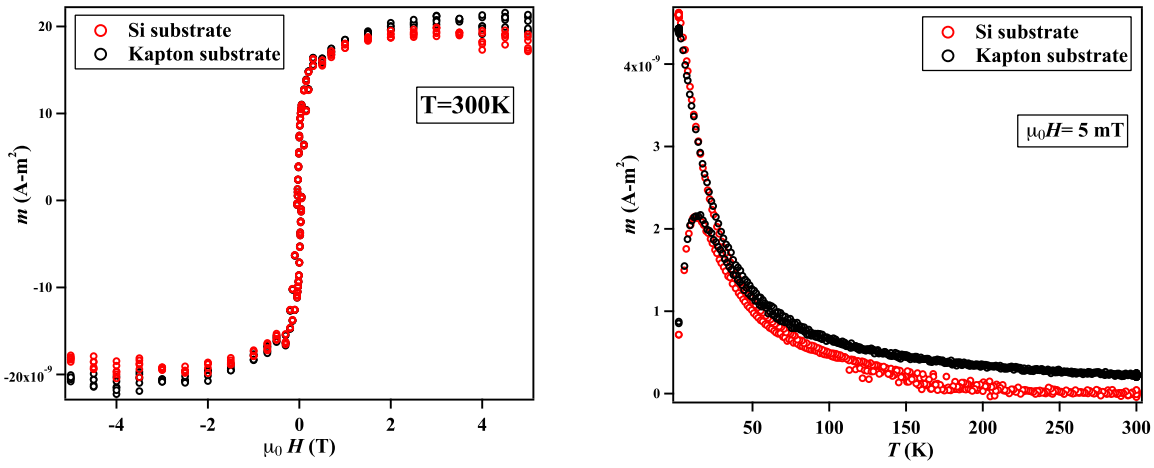

FIG. 61: *Magnetic measurements for cobalt clusters deposited on Kapton and Si substrates. We observe that the magnetization curves at 300 K overlap and ZFC/FC show the same T_{max} corresponding to 13 K.*

We observe that the magnetization curves at 300 K overlap and ZFC/FC show the same T_{max} corresponding to 13 K. The difference between the ZFC/FC curves a high temperatures does not affect to the results obtained from the triple fit protocol. This verification is necessary in order to assure that both samples are identical allowing to discard any disagreement explained by the influence of the substrates in the magnetic measurements.

In order to determine the influence of the cluster concentration on the magnetic properties, we performed a set of measurements that give indications of particle interactions. We started by the magnetization measurements at different temperatures in order to study the superparamagnetic behavior of the particles. After that we studied the influence of the concentration in the ZFC/FC susceptibility curves by the modification of the blocking temperature. Finally we performed the IRM/DcD protocol to detect the presence of the interaction in our samples.

IV.6.2 m(H) measurements

We measured the magnetization cycles at different temperatures for all the samples and we plot the magnetization as function of H/T in order to verified the superparamagnetic behavior. The curves overlap showing the *classical scaling law of superparamagnetism*. The results for the sample of 0.5% and 5% are displayed in **Fig. 62**. The magnetization plotted as function of H/T does not show any deviation at different temperatures. At this point there are no indications of the influence of the cluster concentration from the magnetization measurements.

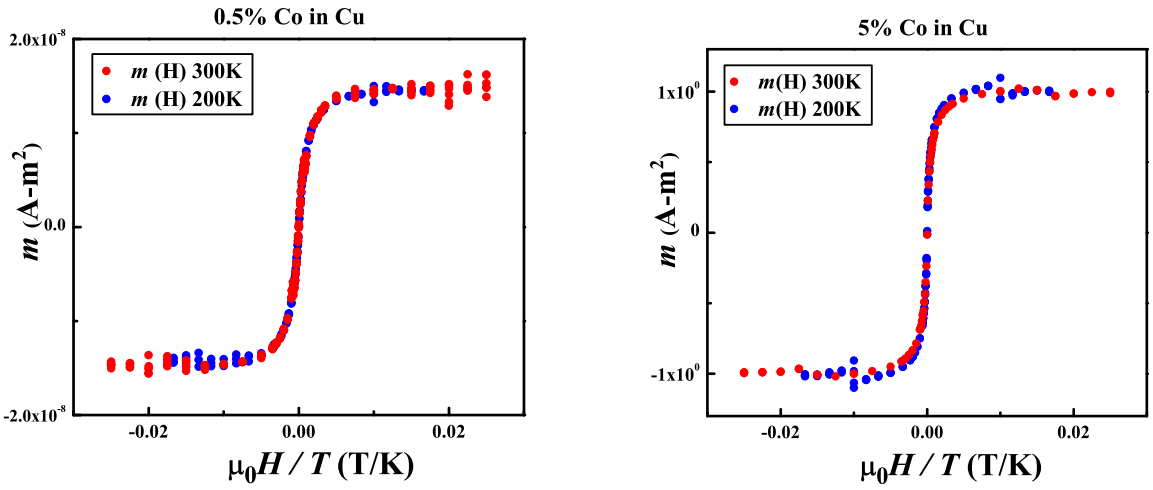

FIG. 62: *Magnetization curves as function of H/T at different temperatures for two different concentrations. The curves overlap showing the classical scaling law of superparamagnetism and there are no indications of the influence of the cluster concentration from the magnetization measurement.*

From the magnetization cycles at 300 K for all samples it is not possible either to observe any difference as a function of the cluster concentration and the three magnetization curves overlap nicely (**Fig. 63**). The magnetization cycles are not sensitive to this concentration level in the same way as was presented in **chapter II** for the magnetization cycles which are not sensitive enough to variations in the cluster size distribution. We need additional magnetic measurements in order to observe the influence of the cluster concentration on the magnetic properties.

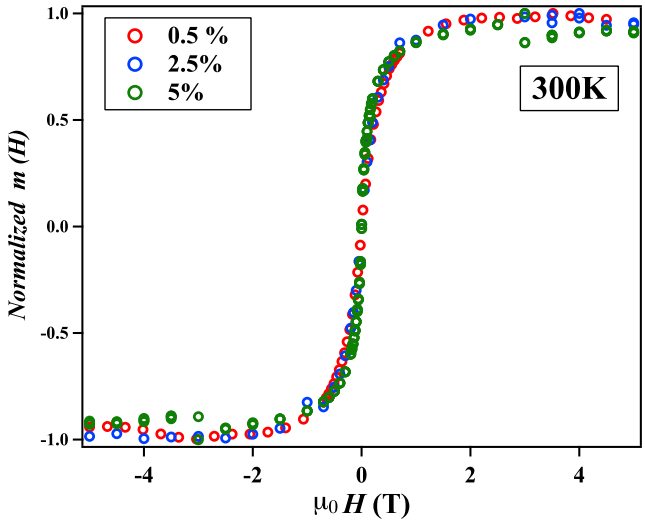

FIG. 63: *Magnetization curves as function of the magnetic field for samples at different concentrations at 300 K. From the magnetization cycles it is not possible either to observe any difference as a function of the cluster concentration and the three magnetization curves overlap nicely.*

IV.6.3 ZFC/FC susceptibility curves

In order to extract more magnetic information from the samples, we performed a set of conventional measurements which consists of the zero field cooled and the field cooled (ZFC/FC) susceptibility curves.

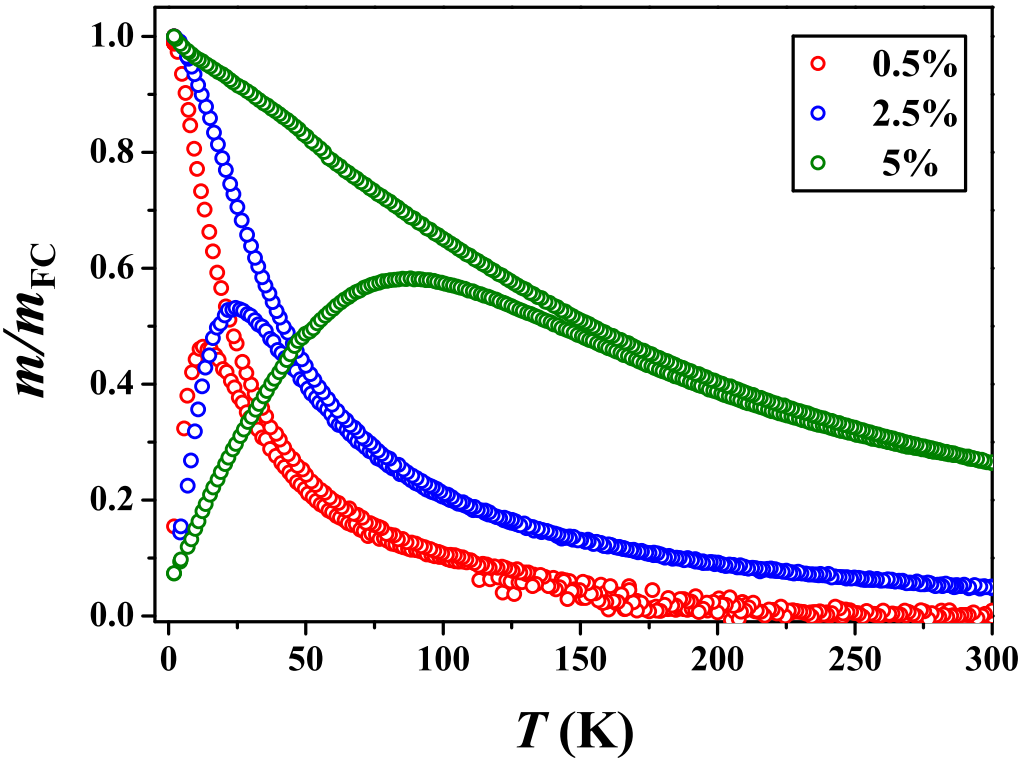

FIG. 64: *ZFC/FC susceptibility curves at 5 mT for samples at different concentrations. We observe that T_{max} is shifted as a function of the concentration from 13 K for the sample of 0.5% to 88 K for the sample of 5%.*

From the ZFC/FC curves for the three samples at different concentrations (0.5%, 2.5% and 5%), we observe that T_{max} is shifted as a function of the concentration from 13 K for the sample of 0.5% to 88 K for the sample of 5%. For samples of 0.5% and 2.5% the dependence of the magnetization in function of the temperature for the FC curve is proportional to $1/T$, which corresponds to the superparamagnetic behavior, but in the case of the more concentrated sample the dependency is linear, showing a behavior corresponding to a correlated spin glasses [11]. These results are displayed in **Table XI**.

IV.6.4 IRM/DcD measurements

We measured the IRM/DcD curves in order to determine the existence of interactions between the clusters induced by the increment on the cluster concentration. From the IRM/DcD measurements we observe that for the sample of 0.5% $\Delta m \sim 0$, indicating that at this concentration level there is no evidence of interactions as was presented in **chapter II**. The value of Δm increases as a function of the concentration in the case of the samples with 2.5% and 5% concentration. This is the confirmation together with the ZFC susceptibility curves that even at low cluster concentrations (2.5%) it is possible to detect correlations between clusters. The Δm curve is an extremely sensitive technique to detect magnetic cluster interactions. The negative value of Δm indicates that the interactions correspond to demagnetizing interactions [43]. The results for the three samples are displayed in **Fig 65**.

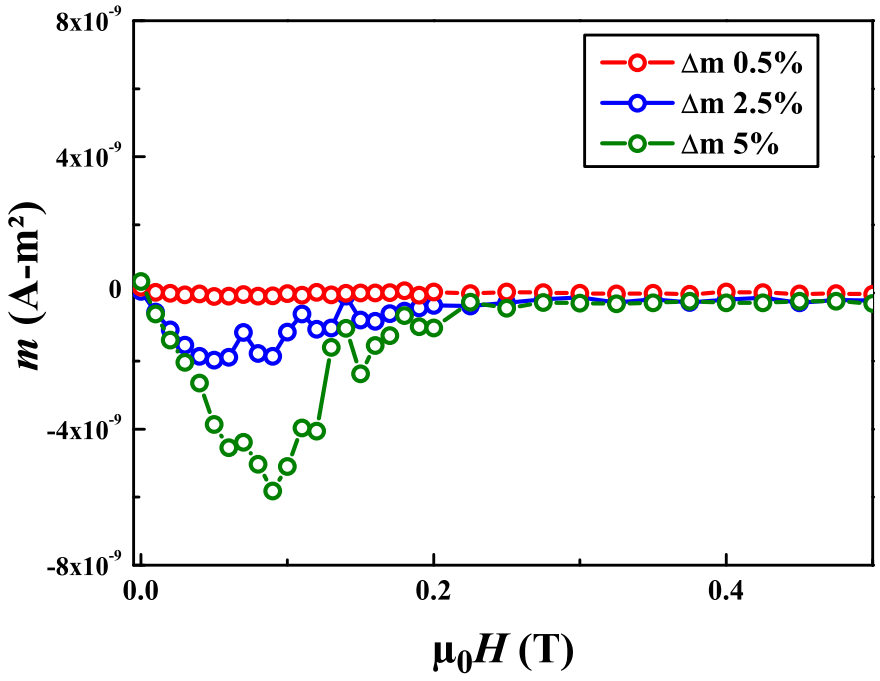

FIG. 65: *Δm curves for samples at different concentrations at 2 K. We observe that for the sample of 0.5% $\Delta m \sim 0$, indicating that at this concentration level there is no evidence of interactions. The value of Δm increases as a function of the concentration in the case of the samples with 2.5% and 5% concentration.*

IV.6.5 Triple fit

To treat the entire data, we used the triple fit protocol where we adjust simultaneously the three curves (ZFC/FC and m(H) at 300 K). Using the triple fit protocol we obtain the median magnetic diameter D_{mag}, the size dispersion w_{mag} and the effective anisotropic constant K_{eff}. For the sample with 0.5% where no interactions have been detected, the triple fit reproduces the experimental data very well and the parameters that we obtain are in agreement with previews studies, using similar conditions for the cluster source and for the concentration [37]. In the case of the more concentrated samples we fitted the data but it was necessary to increase the mean diameter and the effective anisotropy constant in order to reproduce the experimental data. The quality of the fit is not similar to more diluted sample because the triple fit protocol assumes non interacting particles.

The magnetic diameter and the effective anisotropy constant obtained from the triple fit increase as a function of the cluster concentration. The triple fit yields false median diameters for the more concentrated samples even though the fits seem correct. The magnetic interactions can be interpreted by a modification of the size distribution by including magnetic multimers [38]. The experimental ZFC and FC curves cannot be reproduced with the true magnetic diameter. This implies that the initial assumptions for superparamagnetism are not valid and that inter-particle interactions distort the magnetic response. The results are displayed in the **Table XI** and the **Fig 66**.

This complete characterization shows how the magnetic properties are modified by cluster interactions even at very low concentrations, as previous work performed in our group [37]. To have a complete image of the magnetic properties it is necessary to perform complementary measurements, because using only the criterion of plotting $m(H/T)$, is not enough to assure the absence of interactions.

In order to work in diluted cluster systems it is necessary to pay attention to interparticle interactions, because otherwise we can deduce incorrect conclusions about the magnetic properties of the nanoparticles such as the median magnetic diameter or the magnetic anisotropy.

TABLE XI: *Comparison between the three samples at different cobalt concentration: median magnetic diameters D_{mag}, dispersions w_{mag}, and effective anisotropy constants K_{eff} as derived from the triple fit, maximum temperatures of the ZFC curve and coercive fields at 2 K.*

Sample Concentration	D_{mag} (nm)	w_{mag}	K_{eff}(kJ/m^3)	T_{max}(K)	$\mu_0 H_c$(mT)
0.5%	2.3	0.3	135	13	45
2.5%	3.2	0.25	152	24	59
5%	4.3	0.25	280	88	60

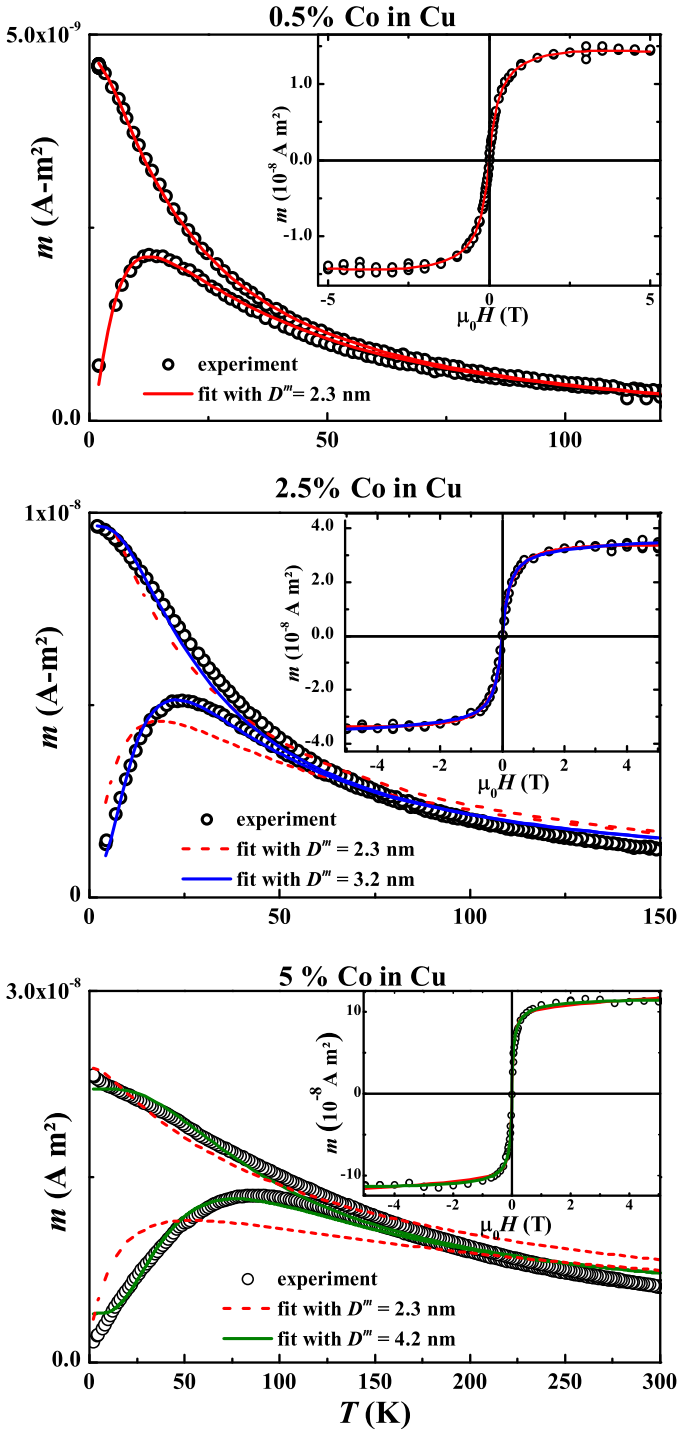

FIG. 66: *ZFC/FC curves taken at 5 mT and magnetization curves at 300 K for samples at different cluster concentration. The solid lines correspond to the adjustments using the triple fit. The red dashed lines show the best fit with the median diameter fixed to the true value of 2.3 nm.*

IV.7 MAGNETO-TRANSPORT RESULTS

The electrical measurements were performed in a SQUID magnetometer which in this case used as a superconductor cryostat where the temperature was varied from 2 K up 300 K and the magnetic field between -5 T and 5 T. We performed a complete electrical characterization, where the set of transport coefficients were measured.

IV.7.1 Resistivity

We measured the resistivity as a function of the temperature between 2 K and 300 K at zero magnetic field. We observe an increased resistivity due to the increment in the nanoparticles concentration. The effect of the nanoparticles is to decrease the electron mean free path and thus increase the resistivity of the sample.

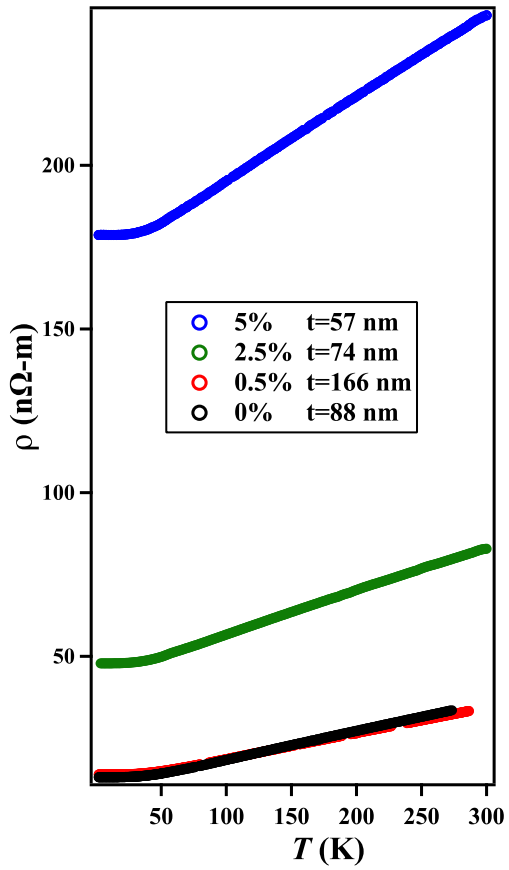

FIG. 67: *Resistivity as function of the temperature at zero magnetic field for Co:Cu samples at different concentrations, where t corresponds to the sample thickness. We observe an increased resistivity due to the increment in the nanoparticles concentration.*

At 2 K when the phonons are frozen and do not contribute to the electrical resistivity we determine the mean free path from the residual resistivity. The values obtained for the m.f.p for each sample (**Table XII**) represent the signature of the scattering processes involved in the electronic scattering, which are controlled by the cluster concentration.

We measured the magnetoresistance in the sample without nanoparticles (0%), and the value was below the noise level of our setup. This result is in agreement with prior measurements for thin gold films where the mean free path has equivalent values and the transport coefficient are controlled by the size of the grains [33]. This result represents an advantage in order to discard transverse magnetoresistance contributions from size effects in order to study the magnetoresistance in granular systems.

TABLE XII: *Comparison between the three samples at different cobalt concentrations: mean free path (m.f.p) at 2 K, Hall mobility μ_H, drift mobility μ_D and the ratio r between them.*

Sample Concentration	m.f.p 2 K (nm)	μ_H (10^{-3} T^{-1})	μ_D (10^{-3}T^{-1})	r
0%	52	5.80	4.97	1.16
0.5%	52	5.84	5.90	0.99
2.5%	13	1.42	1.47	0.97
5%	3	0.37	0.44	0.84

IV.7.2 Hall Effect

The Hall mobility μ_H and the drift mobility μ_D were determined from the Hall effect and the residual resistivity at 2 K. The ratio r between the Hall mobility and the drift mobility is close to 1 for all the samples and thus the Fermi surface for copper can be considered spherical neglecting the presence of a second electron carrier.

By using the Hall effect measurements we determined the thicknesses of the samples. The thickness of each sample was obtained by fitting the experimental data using **Eq. 48** and the results are compared with the thickness measurements using the quartz microbalance. The values obtained by both techniques are in agreement within 10% and the results are displayed in the **Table XIII**.

TABLE XIII: *Comparison of the sample thickness obtained by Hall Effect measurements and the quartz microbalance.*

Sample Concentration	Hall Thickness (nm)	Microbalance Thickness (nm)
0%	88	100
0.5%	166	151
2.5%	74	78
5%	57	53

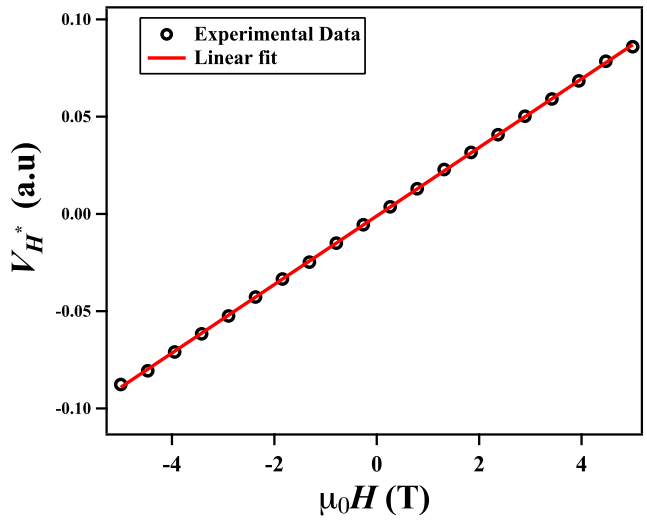

FIG. 68: *Normalized V_H^* as function of the magnetic field. The inverse of the slope corresponds to the thickness of the sample.*

IV.7.3 Magnetoresistance

In this section we present the MR results for a set of samples in order to study the influence of the concentration by cluster interactions on the transport properties. From the electric characterization we observed that the resistivity is determined by the cluster concentration and the samples do not exhibit ordinary transverse magnetoresistance.

We measured the MR where the magnetic field is oriented perpendicular to the plane of the samples and the measurements were performed at different temperatures, the result are displayed in the **Fig. 69**.

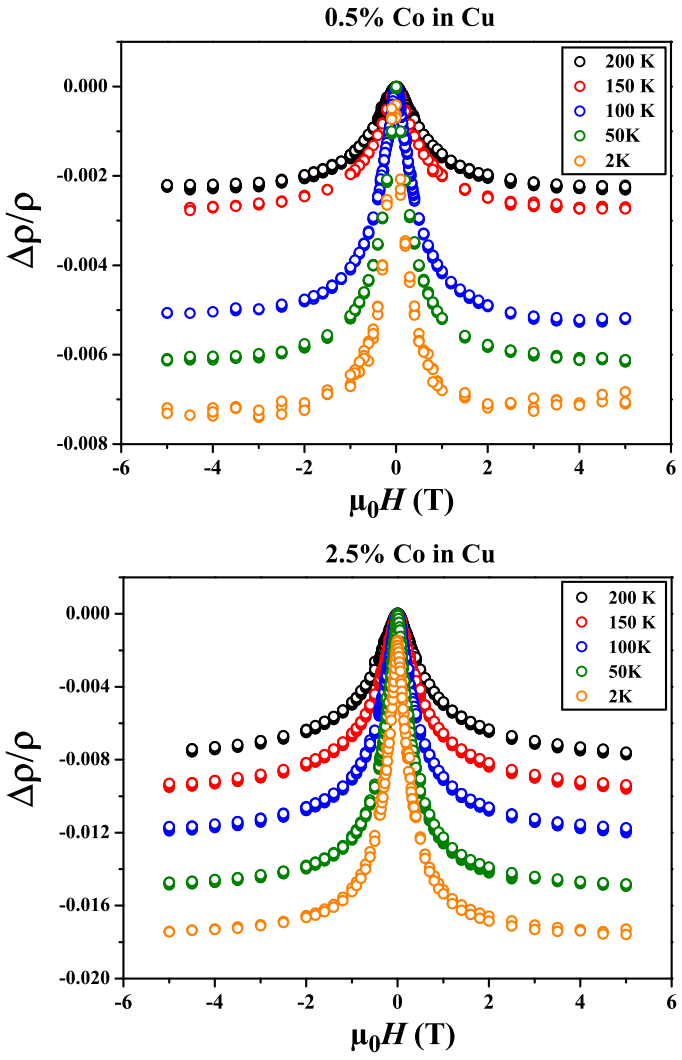

FIG. 69: *MR as function of the magnetic field at different temperatures for 0.5% and 2.5% of cluster concentration.*

We observe that the effect of increasing temperature reduces the time elapsed between scattering events, and hence to reduce the influence of the magnetic field, thus reducing the value of the magnetoresistance. For the three samples the maximum value of the MR (5 T) shows a linear dependency on temperature similar to the resistivity as function of the temperature.

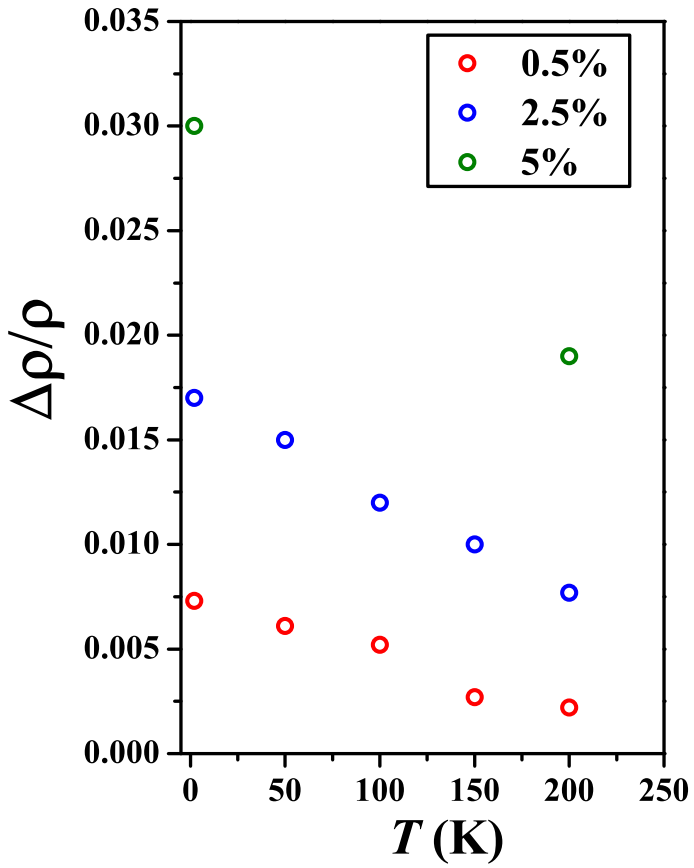

FIG. 70: *MR at 5 T as a function of the temperature for samples with different cluster concentration. For the three samples the maximum value of the MR (5 T) shows a linear dependency on temperature similar to the resistivity as function of the temperature.*

At 2 K the system is in the ferromagnetic state and both the magnetization and the magnetoresistance curves show hysteric behavior. For both measurements the coercive field is identical and the results for the sample of 0.5% are displayed in **Fig. 71** .

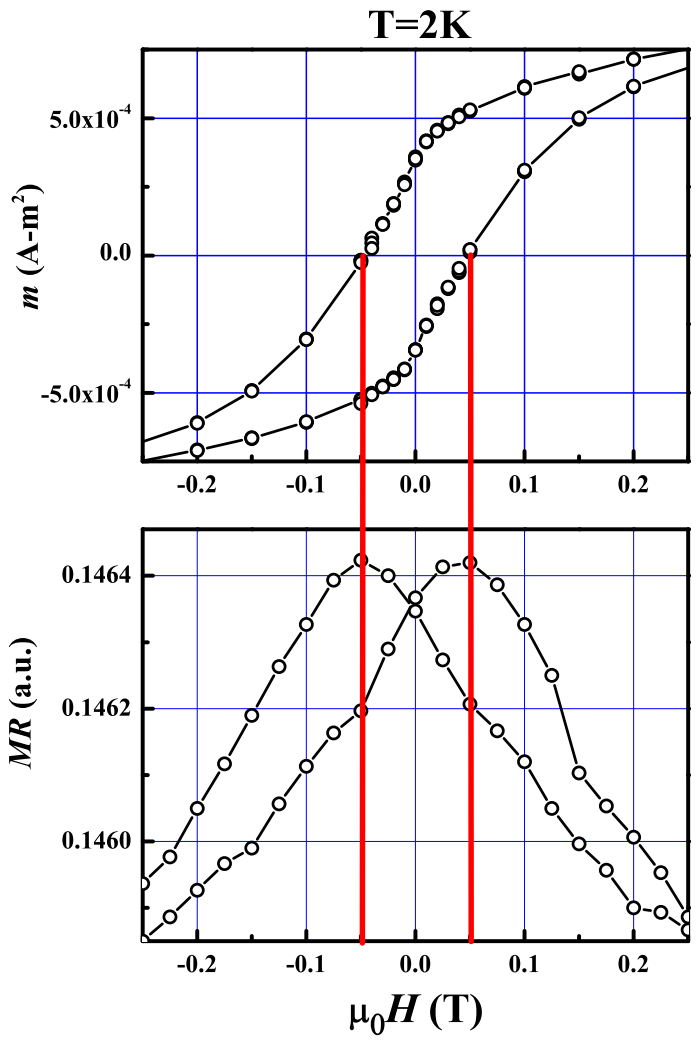

FIG. 71: *Magnetization cycles and magnetoresistance measurements at 2 K for the sample of 0.5% of concentration.*

With the purpose of studying the superparamagnetic state at high temperature we plot the MR in function of H/T. The curves overlap nicely showing the *classical scaling law of superparamagnetism* in the case of the sample of 0.5%. For the sample of 2.5% there are small variations indicating a deviation from the superparamagnetic behavior. The results for the sample of 0.5% and 2.5% are displayed in **Fig. 72**.

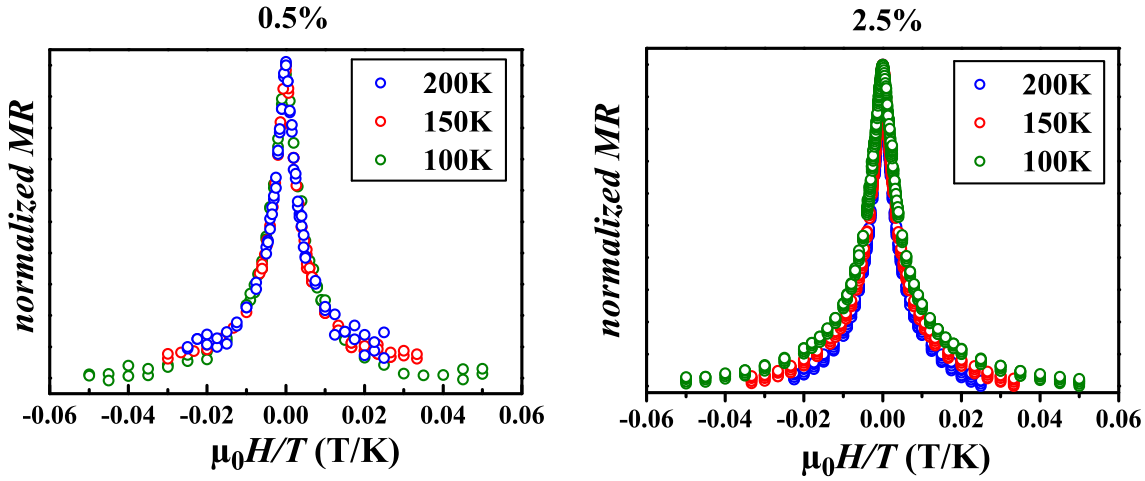

FIG. 72: *Magnetoresistance curves as function of H/T. The curves overlap nicely showing the classical scaling law of superparamagnetism in the case of the sample of 0.5%. For the sample of 2.5% there are small variations indicating a deviation from the superparamagnetic behavior.*

Now if we compare the three magnetization curves and the MR curves at 200 K for the three samples we cannot distinguish any significant difference in function of the cluster concentration, and the curves overlap.

The magnetoresistance results do not exhibit any deviation as a function of the cluster concentration, in the same way as magnetization cycles, both measurement are **not sensitive** to deviations from superparamagnetism due to magnetic interactions at the concentrations discussed here.

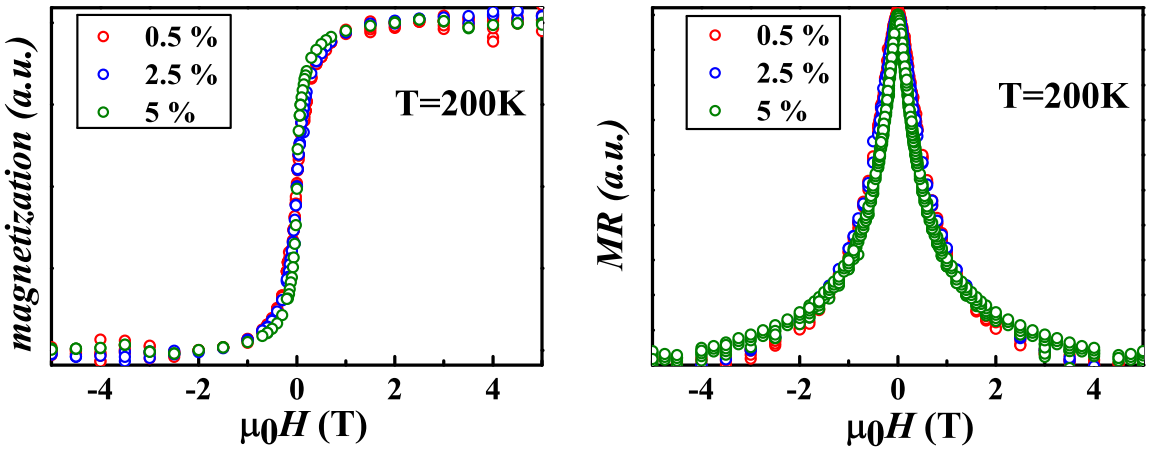

FIG. 73: *Normalized magnetization and magnetoresistance curves for samples with different concentration at 200 K. The magnetoresistance results do not exhibit any deviation as a function of the cluster concentration, in the same way as magnetization cycles, both measurement are* **not sensitive** *to deviations from superparamagnetism due to magnetic interactions.*

IV.8 DISCUSSION

IV.8.1 Zhang and Levy Model

The model developed by Zhang and Levy [83] describes the dependence of the conductivity on the magnetic field in a system where magnetic *granules* or magnetic impurities with a size distribution are immersed in a non magnetic matrix. The magnetoresistance is derived by adapting a formalism developed for thin films, where the current is perpendicular to the plane of the film [84, 85].

The nanoparticles are considered as single ferromagnetic domains and the resistivity comes from the spin-dependent impurity scattering at the interface between the magnetic cluster and the non magnetic matrix and in a minor grade from the spin-dependent scattering within the magnetic cluster.

The current at zero magnetic field is equally shared in the spin-up and spin-down channels and the probability to be scattered will be identical. The presence of a magnetic field defines a quantization axis and each macrospin will try to align parallel to the magnetic field. A macrospin in the electron path will polarize the electron current parallel or antiparallel to the particle magnetic moment. Now an electron scatters from a second magnetic particle oriented in a different direction with respect to the first one, for one spin-channel will more *easy* to pass than the other, and the resistivity decreases. The variation in the resistivity will depend on the relative orientation of the magnetization axes of the nanoparticles.

The conductivity assuming a two current model is expressed by:

$$\sigma = \frac{nq^2}{2m} \sum_{\sigma} \frac{1}{\Delta^{\sigma}} \tag{50}$$

Where n represents the number of conduction electron per unit volume, q is the electron charge, m is the electron mass and Δ^{σ} corresponds to the imaginary part of the self-energy of the conduction electrons due the impurity scattering.

The total scattering potential that gives rise to the resistivity is composed of the impurity scattering in the matrix (nm), the spin dependent scattering at the interface (s) and the spin dependent scattering within magnetic nanoparticle (m) and it is expressed by:

$$
\begin{aligned}
V(\vec{r},\hat{\sigma}) = &\sum_i V_i^{(mn)}\delta(\vec{r}-\vec{R}_i) \\
&+\sum_\alpha\sum_{i\in\alpha} V_i^{(m)}(1+p_b\hat{\sigma}\cdot\hat{S}_i)\delta(\vec{r}-\vec{R}_i^\alpha) \\
&+\sum_\alpha\sum_{s\in\alpha} V_s(1+p_s\hat{\sigma}\cdot\hat{S}_s)\delta(\vec{r}-\vec{R}_s^\alpha)
\end{aligned}
\tag{51}
$$

Where R_i and R_s are the impurities position, α corresponds to index of the magnetic *granule*, p_s and p_b represent the ratios of the spin dependent potentials to spin independent process for the interface and the volume of the nanoparticles, these values are between 0 and 1. $\hat{\sigma}$ corresponds to the Pauli matrices and $\hat{S}_i$, $\hat{S}_s$ are unit vectors for the spin of the magnetic moment of the impurities within the volume and at the surface.

The scattering matrix is obtained using Fermi's "Golden Rule":

$$
\Delta^\sigma = \pi\sum_{k'}|V^\sigma_{k,k'}|\delta(\epsilon_{k'}-\epsilon_k) \tag{52}
$$

and yields:

$$
\begin{aligned}
\Delta^\sigma = &\frac{\pi}{N}\Big(\sum_i |V_i^{mn}|^2 \\
&+\sum_\alpha\sum_{i\in\alpha}|V_i^m|^2(1+p_b^2+2p_b\hat{\sigma}\cdot\hat{M}_\alpha) \\
&+\sum_\alpha\sum_{s\in\alpha}|V_s|^2(1+p_s^2+2p_s\hat{\sigma}\cdot\hat{M}_\alpha)\Big)\rho(\epsilon_F)
\end{aligned}
\tag{53}
$$

Where $\hat{M}_\alpha$ is the direction of the total magnetic moment of each particle, assuming that each particle acts like a monodomain and $\rho(\epsilon_F)$ is the density of states at the Fermi level.

We can express the mean free path by:

$$
\lambda_t = \frac{\epsilon_F N_t}{\pi k_F\sum_{i\in t}|V_i^{(t)}|^2\rho(\epsilon_F)} \tag{54}
$$

Here $t = nm$ represent the matrix and m and s correspond to the nanoparticles and

the interfaces, respectively. $N_{t=nm,m,s}$ are the numbers of the lattice sites for the matrix, the nanoparticles and the interface. The relation between the number of lattice sites between the surface and the volume of the nanoparticles is given by:

$$\begin{aligned} N_m &= \frac{V_m}{L^3} & N_s &= \frac{S_m}{L^2} \\ N_m &= \frac{\frac{4}{3}\pi r_m^3}{L^3} & N_s &= \frac{4\pi r_m^2}{L^2} \\ & & N_s &= (36\pi)^{1/3} N_m^{2/3} \end{aligned} \tag{55}$$

Replacing the values for the mean free path for each contribution gives an expression for Δ^σ expressed by:

$$\Delta^\sigma = \frac{\epsilon_F}{k_F}(\xi_0 + \sigma\xi_1) \tag{56}$$

where

$$\xi_0 = \frac{1-c}{\lambda_{nm}} + \frac{c}{\lambda_m}(1+p_b^2) + \frac{a_0(36\pi)^{1/3}c(1+p_s^2)}{\lambda_s}\frac{\int V_\alpha^{2/3} f(V_\alpha)dV_\alpha}{\int V_\alpha f(V_\alpha)dV_\alpha} \tag{57}$$

$$\xi_1 = \frac{2cp_b}{\lambda_m}\frac{\int V_\alpha f(V_\alpha)m_\alpha(V_\alpha)dV_\alpha}{\int V_\alpha f(V_\alpha)dV_\alpha} + \frac{a_0 2(36\pi)^{1/3}cp_s}{\lambda_s}\frac{\int V_\alpha^{2/3} f(V_\alpha)m_\alpha(V_\alpha)dV_\alpha}{\int V_\alpha f(V_\alpha)dV_\alpha} \tag{58}$$

In the previous expression ξ_0 represents the contribution to the resistivity at zero field, c is the nanoparticle concentration and a_0 is the lattice constant of the nanoparticles, $f(V_\alpha)$ is the size distribution function.

It was assumed that each nanoparticle acts like a mono-domain with superparamagnetic behavior, without interactions between then. The magnetic moment as a function of the magnetic field H at a determined temperature T is described by the Langevin function $\mathcal{L}(x)$.

Finally we can expressed the conductivity by:

$$\sigma = \frac{nq^2 k_F}{m\epsilon_F}\frac{\xi_0}{\xi_0^2 - \xi_1^2} \tag{59}$$

And the magnetoresistance by:

$$\frac{\Delta\rho}{\rho} = -\frac{\xi_1^2}{\xi_0^2} \tag{60}$$

The result shows a quadratic dependence of the magnetoresistance with respect to magnetization, in the same way as the qualitative previews studies as the geometric representation described in section IV.1.6.

In order to quantify the magnetoresistance in our measurements we used the Zhang and Levy model to describe the experimental data. We used **Eq. 59** for the resistivity ρ as a function of the magnetic field at different temperatures.

The theoretical expression for the resistivity can be divided into two main parts that contribute as scattering sources; the spin dependent scattering at the interface and within of the nanoparticles. The contribution of the interface is characterized by the factor $V_\alpha^{2/3}$ that depends of the number of the atoms at the cluster surface whereas the factor V_α characterizes the scattering in the particle.

The theoretical model has not incorporated the effect of the temperature in the electronic transport and the contribution of the temperature is only used as the thermal agitation for the magnetic moment. In order to take account the electron-phonon scattering we measured the resistivity as function of the temperature of a pure copper sample at zero magnetic field and we determined the mean free path as a function of the temperature for the non-magnetic matrix λ_{nm} using the expressions **46** and **47**.

IV.8.2 Zhang and Levy fit

In this section we test the model for samples with different cluster concentration (0.5%, 2.5% and 5%) and at different temperatures (50 K, 100 K, 150 K and 200 K). Using the Zhang and Levy model, we try to evaluate the contribution of the two scattering mechanisms to the transport properties by fitting the experimental data using only the contribution of the volume ($p_s = 0$) or only the surface ($p_b = 0$). We describe the size distribution $f(V_\alpha)$ with a log-normal function (**Eq. 32**) represented by the median size D_{MR} and the size dispersion w_{MR}. We analyzed independently which spin scattering source determines the magnetoresistance in order to elucidate the role of the interface or the volume of the particle in the electronic transport properties.

The model presents a large number of free parameters, thus the first step was to analyze each contribution independently using the scattering ratio $p_b = 0$, for the case where the diffusion is only at the interface and $p_s = 0$ where the scattering within the particle is dominant.

Using these two parameters (p_b, p_s) equal to zero at the same time allows to determine the resistivity at zero magnetic field determined by ξ_0 which is composed by the diffusion in the copper matrix λ_{nm}, the interface λ_s and within the particle λ_m as independent scattering mechanisms.

The adjustable parameters are p_s, p_b, λ_s, λ_m, the diameter D_{MR}, and the dispersion w_{MR}.

We started by fitting the MR curves at high temperatures (200 K, 150 K and 100 K) where it is possible to describe the experimental data for all samples. In the case of the temperature of 50 K it is not possible to reproduce our data by using the m.f.p obtained from the test sample.

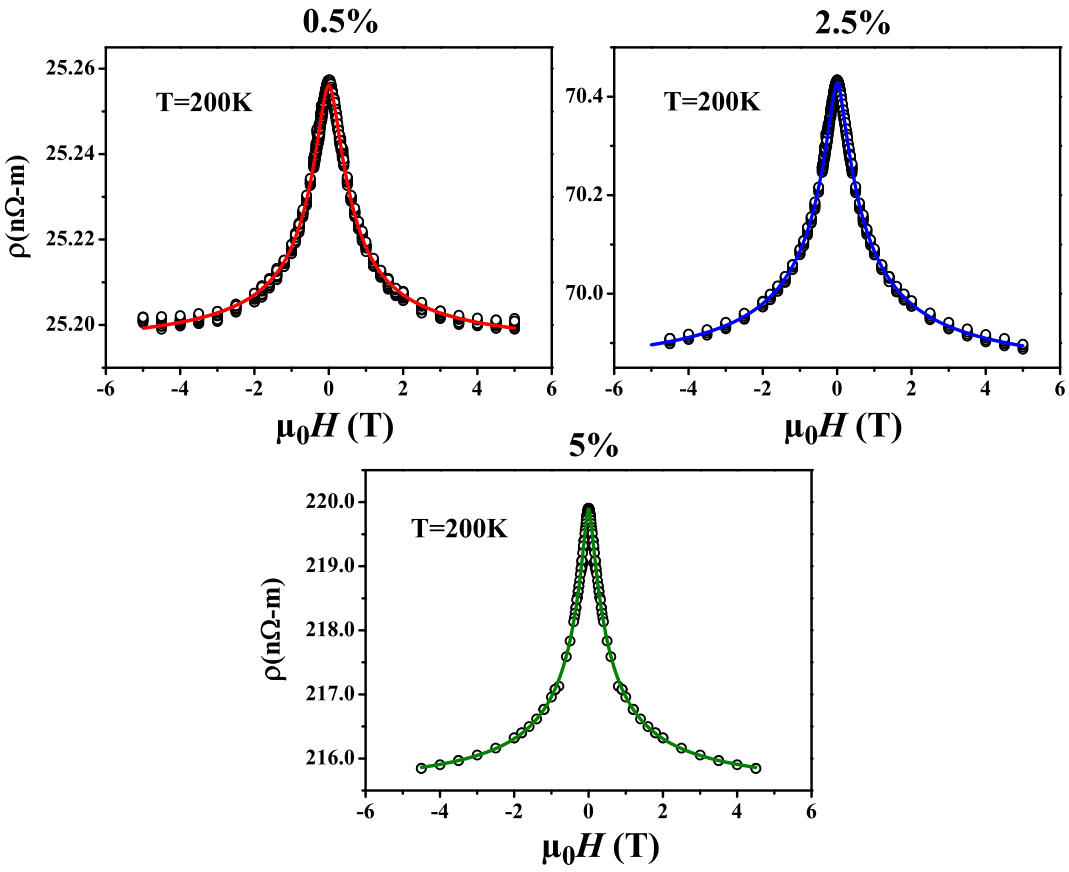

FIG. 74: *Experimental data (circles) and fit (line) of the MR curves using the Zhang and Levy model at 200 K. The resistivity data as function of the magnetic field can be reproduced nicely and independently using only the contribution of the interface ($p_b = 0$) or only the volume ($p_s = 0$) for all the samples.*

TABLE XIV: *Parameters obtained by using the Zhang and Levy model for samples with different cluster concentration at 200 K.*

Parameters	200 K & λ_{nm}=28 nm					
	0.5%		2.5%		5%	
	Interface	Volume	Interface	Volume	Interface	Volume
p_s	0.5	0	0.3	0	0.5	0
p_b	0	0.7	0	0.2	0	1
λ_s (nm)	1.4	3.8	0.7	0.3	0.1	0.9
λ_m (nm)	20	3.6	0.5	0.9	0.4	0.2
D_{MR} (nm)	2.4	2.4	2.4	2.1	2.3	2.5
w_{MR} (nm)	0.22	0.18	0.27	0.28	0.31	0.31

The resistivity data as function of the magnetic field at $T = 200$ K and $T = 150$ K and 100 K can be reproduced nicely and independently using only the contribution of the interface ($p_b = 0$) or only the volume ($p_s = 0$) for the sample of 0.5%. The median size D_{MR} obtained from the fit for the sample of 0.5% is in agreement with the value obtained from the triple fit where the system does not show evidence of cluster interactions. The values obtained for the diameter for the all the samples is almost the same and it is in agreement with the fact that the MR curves overlap at 200 K **Fig. 74**.

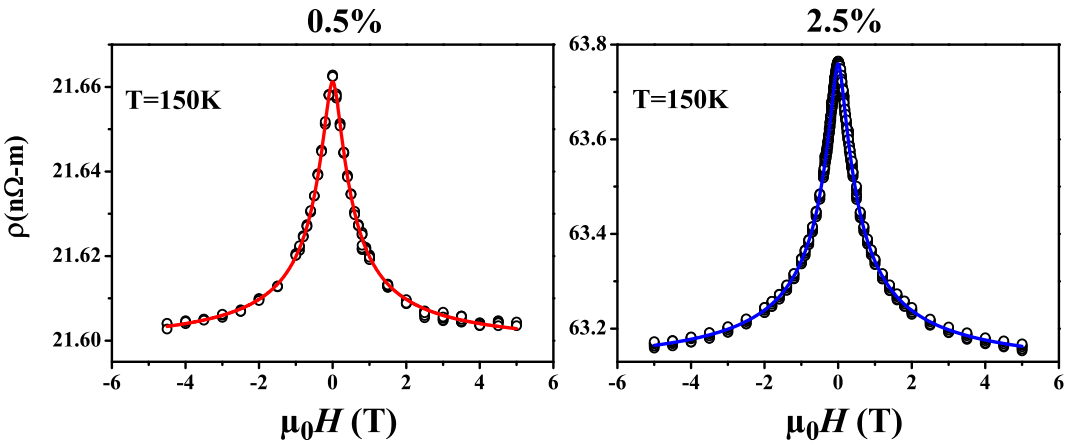

FIG. 75: *Experimental data (circles) and fit (line) of the MR curves by using the Zhang and Levy model at 150 K. The resistivity data as function of the magnetic field can be reproduced nicely and independently using only the contribution of the interface ($p_b = 0$) or only the volume ($p_s = 0$) for the samples of 0.5% and 2.5% of concentration.*

TABLE XV: *Parameters obtained by using the Zhang and Levy model for samples with different cluster concentration at 150 K.*

Parameters	150 K & λ_{nm}=33 nm			
	0.5%		2.5%	
	Interface	Volume	Interface	Volume
p_s	0.4	0	0.3	0
p_b	0	0.7	0	0.2
λ_s (nm)	1.4	3.0	0.7	0.4
λ_m (nm)	18	3.7	0.5	0.9
D_{MR} (nm)	2.4	2.4	2.3	2.2
w_{MR} (nm)	0.18	0.19	0.27	0.26

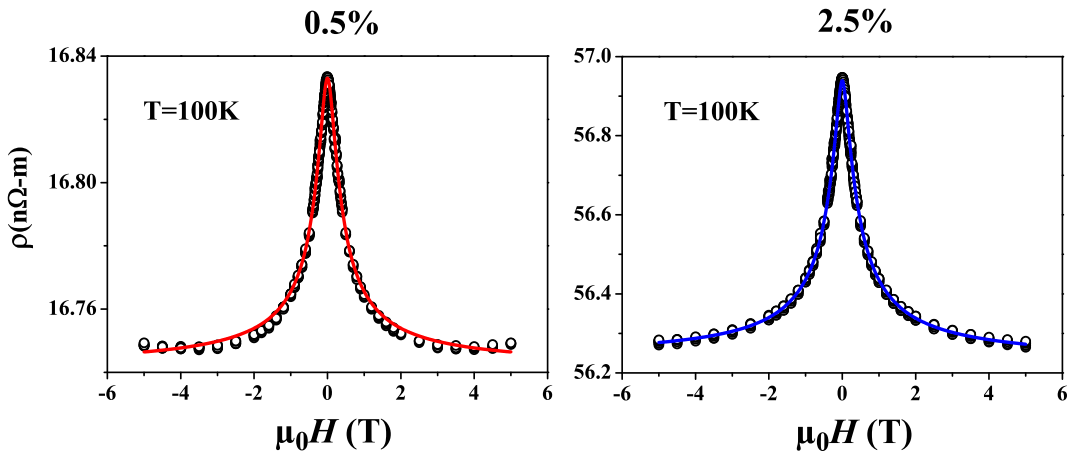

FIG. 76: *Experimental data (circles) and fit (line) by using the Zhang and Levy model at $T = 100$ K. The resistivity data as function of the magnetic field can be reproduced nicely and independently using only the contribution of the interface ($p_b = 0$) or only the volume ($p_s = 0$) for the sample of 0.5%. For the sample of 2.5% the resistivity data cannot be reproduced using only the volume, in order to adjust the data it is necessary to increase the concentration by a factor 2 using the value for the m.f.p. from the test sample.*

TABLE XVI: *Parameters obtained by using the Zhang and Levy model for samples with different cluster concentration at 100 K.*

Parameters	100 K & λ_{nm}=40 nm			
	0.5%		2.5%	
	Interface	Volume	Interface	Volume
p_s	0.5	0	0.3	0
p_b	0	0.6	0	0.2
λ_s (nm)	1.5	6.3	1.1	0.8
λ_m (nm)	19	3.1	5.4	2.3
D_{MR} (nm)	2.3	2.3	2.2	2.1
w_{MR} (nm)	0.18	0.19	0.23	0.23

The resistivity data at $T = 50$ K for the sample of 0.5% of concentration cannot be reproduced using the value for the m.f.p from the test sample ($\lambda_{nm} = 49$ nm at 50 K). The resistivity data can only described by increasing the m.p.f value ($\lambda_{nm} = 53$ nm), which corresponds to a value of resistivity below of the bulk value and furthermore the obtained value for the median size is ($\sim$2 nm), which is smaller than the value obtained at high temperatures.

Now for the sample of 2.5% the resistivity data as function of the magnetic field at $T = 200$ K and $T = 150$ K can be reproduced nicely and independently using only the contribution of the interface ($p_b = 0$) or only the volume ($p_s = 0$). The resistivity data at $T = 100$ K cannot be reproduced using only the volume, in order to adjust the data it is necessary to increase the concentration by a factor 2. In the case of the interface the data can be reproduced nicely but the mean size obtained is smaller than from the fit at 200 K. At $T = 50$K the experimental data is reproduced in both cases, but the median size obtained is smaller than the value obtained at high temperatures.

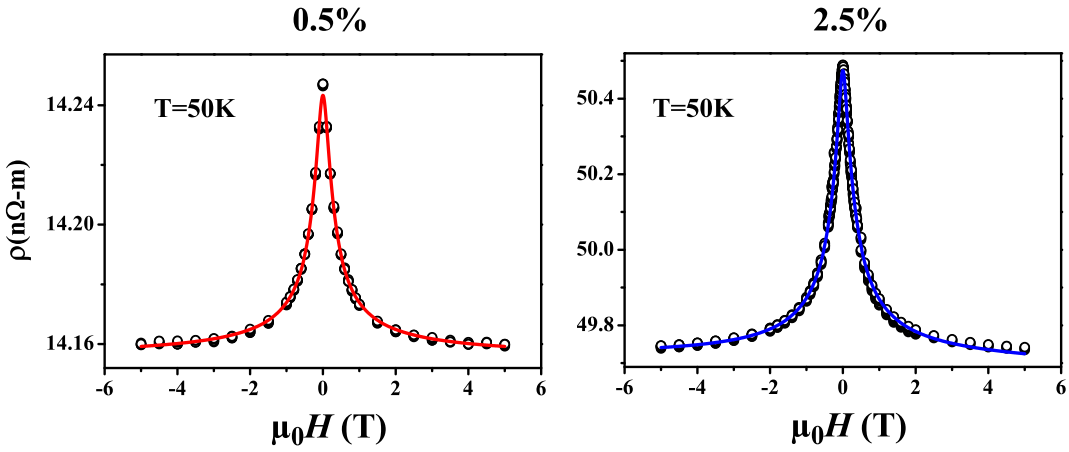

FIG. 77: *Experimental data (circles) and fit (line) by using the Zhang and Levy model at $T = 50$ K. The experimental data cannot be reproduced using the value for the m.f.p from the test sample. In order to reproduce the experimental data it is necessary to increase the m.f.p. that means reducing the resistivity of the sample, even below the bulk value.*

TABLE XVII: *Parameters obtained by using the Zhang and Levy model for samples with different cluster concentration at 50 K.*

Parameters	50 K & λ_{nm}=49 nm			
	0.5%		2.5%	
	Interface	Volume	Interface	Volume
p_s	0.8	0	0.3	0
p_b	0	0.9	0	0.1
λ_s (nm)	3.2	3.4	1.2	1.1
λ_m (nm)	5.3	5.2	0.6	0.6
D_{MR} (nm)	2.0	2.0	2.0	1.9
w_{MR} (nm)	0.15	0.15	0.23	0.23

We analyzed the quality of the theory as a function of the temperature. For the sample of 0.5%, where the system does not show evidence of magnetic interactions, the Zhang and Levy model reproduces nicely the MR between 200 K and 100 K and we obtain a value for the median diameter in agreement with the value obtained from the triple fit.

In the case of 50 K, to fit the data it is necessary to use a λ_{nm} value larger than the value corresponding to this temperature and the median determined size starts to deviate from the correct value of 2.3 nm. This disagreement can be explained by two ways, first the fact that the theoretical model uses the effect of the temperature in an independent way for transport and magnetism. Second at 50 K the superparamagnetic assumption is no longer valid since a fraction of the ensemble is already blocked.

Finally it is not possible to determine which spin-dependent scattering dominates in the transport properties. This can be explained by the high number of free parameters that the theoretical model uses. Using independently either scattering mechanism we can reproduce the experimental data in contrast with prior studies where it was necessary to take account both contribution [22] but whose samples are more concentrated (10%). Is important to remark that the parameters obtained by the model to describe the MR are in the order of magnitude of typical expected values. The values obtained in this work for the different parameters are in agreement with the values obtained for cobalt nanoparticles in silver matrices [55] but for more concentrated samples (5-35%).

IV.9 CONCLUSIONS

We prepared samples at different cluster concentrations where the increase of the cluster concentration determines the value of the resistivity over the rest of scattering mechanisms present in the copper film, such as the surface or grain boundaries. The magnetization cycles and MR curves do not exhibit any deviation as a function of the cluster concentration and both measurements are **not enough sensitive** to deviations from superparamagnetism due to magnetic interactions. The variation in the T_{max} for the ZFC/FC curves is the first indication of the influence of the cluster interaction and confirmed with the IRM/DcD measurements.

We have verified the commonly used description of magnetoresistance in granular media using a truly superparamagnetic sample with cobalt clusters in a copper matrix of 0.5% concentration. None of the possible and redundant checks in both magnetometry and magnetoresistance showed evidence of interparticle interactions and all the derived results are consistent. This is, to our knowledge, the first time that such complete experiments have been performed on a sample that rigorously satisfies the prerequisite of absence of correlations between neighboring macrospins, mandatory in the commonly used model by Zhang and Levy [83] . The necessity of this precondition is underlined in the comparison with two more concentrated samples (2.5 % and 5% of concentration), which yield ambiguous results and only at close inspection reveal deviations from superparamagnetism. Our results demonstrate the necessary precautions and constitute a solid basis for further studies of the spintronic properties of granular systems. A continuative study of samples with embedded nanoparticles of varying size is scheduled in order to resolve the role of interface and volume scattering in cluster-assembled magnetic nanostructures.

General Conclusions

In order to study the nature of the magnetic anisotropy as a function of the cluster size we analyzed two contributions that determine the magnetic anisotropy; the shape of the cluster and the influence of the cluster surface. Using two models to describe the magnetic anisotropy we separated each contribution depending on the cluster size. We demonstrated that for bigger clusters (5.5 nm in diameter) the shape of the particles is enough to describe the magnetic anisotropy and for smaller clusters of $\sim$2 nm, where the aspect ratio is close to 1, the magnetic anisotropy is dominated by the surface anisotropy.

We have verified the commonly used description of magnetoresistance in granular media using a truly superparamagnetic sample with cobalt clusters in a copper matrix of 0.5% concentration. None of the possible and redundant checks in both magnetometry and magnetoresistance showed evidence of interparticle interactions and all the derived results are consistent. Our results demonstrate the necessary precautions and constitute a solid basis for further studies of the spintronic properties of granular systems.

Publications During this Work

1. *Giant Magnetoresistance in Cluster-Assembled Nanostructures: on the influence of inter-particle interactions.* **J. Nanopart. Res. (2013) 15:1968**

   Simón Oyarzún, Artur Domingues Tavares de Sá, Juliette Tuaillon-Combes, Alexandre Tamion, Arnaud Hillion, Olivier Boisron, Alexis Mosset, Michel Pellarin, Véronique Dupuis, and Matthias Hillenkamp.

2. *Transverse magnetoresistance induced by electron-surface scattering on thin gold films: Experiment and theory.* **Applied Surface Science 289 (2014) 167-172** .

   Simón Oyarzún, Ricardo Henríquez, Marco Antonio Suárez, Luis Moraga , Germán Kremer, and Raúl C. Munoz.

3. *Giant magnetoresistance in cluster-assembled nanostructures: a quantitative approach.* (submitted)

   Simón Oyarzún, Artur Domingues Tavares de Sá, Véronique Dupuis, and Matthias Hillenkamp.

4. *Size effects in the magnetic anisotropy of embedded cobalt nanoparticles: from shape to surface.* (In preparation)

   Simón Oyarzún, Alexandre Tamion, Florent Tournus, Véronique Dupuis, and Matthias Hillenkamp.

BIBLIOGRAPHY

[1] R. Alayan, L. Arnaud, M. Broyer, E. Cottancin, J. Lermé, J. Vialle, and M. Pellarin. Morphology and growth of metal clusters in the gas phase: A transition from spherical to ramified structures. *Physical Review B*, 73(12):125444, Mar. 2006. 75

[2] P. Allia, M. Knobel, P. Tiberto, and F. Vinai. Magnetic properties and giant magnetoresistance of melt-spun granular Cu_{100-x}-Co_x alloys. *Physical Review B*, 52(21):15398–15411, 1995. 96, 97

[3] D. Alloyeau, C. Mottet, and C. Ricolleau. *Nanoalloys: Synthesis, Structure and Properties*. Springer, 2012. 39

[4] C. Andersson, B. Sanyal, O. Eriksson, L. Nordström, O. Karis, D. Arvanitis, T. Konishi, E. Holub-Krappe, and J. Dunn. Influence of Ligand States on the Relationship between Orbital Moment and Magnetocrystalline Anisotropy. *Physical Review Letters*, 99(17):177207, Oct. 2007. 60

[5] M. N. Baibich, J. M. Broto, A. Fert, F. N. Van Dau, F. Petroff, P. Etienne, G. Creuzet, A. Friederich, and J. Chazelas. Giant magnetoresistance of (001) Fe/(001) Cr magnetic superlattices. *Physical Review Letters*, 61(21):2472–2475, 1988. 93, 97

[6] J. Bartolomé, L. García, F. Bartolomé, F. Luis, R. López-Ruiz, F. Petroff, C. Deranlot, F. Wilhelm, A. Rogalev, P. Bencok, N. Brookes, L. Ruiz, and J. González-Calbet. Magnetic polarization of noble metals by Co nanoparticles in M-capped granular multilayers (M=Cu, Ag, and Au): An x-ray magnetic circular dichroism study. *Physical Review B*, 77(18):184420, May 2008. 60

[7] G. E. W. Bauer, E. Saitoh, and B. J. van Wees. Spin caloritronics. *Nature Materials*, 11(5):391–399, May 2012. 98

[8] C. P. Bean and J. D. Livingston. Superparamagnetism. *Journal of Applied Physics*, 30(4):S120, 1959. 40, 41, 59, 97

[9] A. E. Berkowitz, J. R. Mitchell, M. J. Carey, A. P. Young, S. Zhang, F. E. Spada, F. T. Parker, A. Hutten, and G. Thomas. Giant magnetoresistance in heterogeneous Cu-Co alloys. *Physical Review Letters*, 68(25):3745–3748, 1992. 97

[10] G. Binasch, P. Grünberg, F. Saurenbach, and W. Zinn. Enhanced magnetoresistance in layered magnetic structures with antiferromagnetic interlayer exchange. *Physical Review B*, Jan. 1989. 93, 97

[11] K. Binder and A. P. Young. Spin glasses: Experimental facts, theoretical concepts, and open questions. *Reviews of modern physics*, 58(4):801–976, Oct. 1986. 109

[12] F. J. Blatt. Theory of mobility of electrons in solids. *Solid state physics*, 4:199–366, 1957. 90, 91

[13] K. Bromann, C. Félix, H. Brune, W. Harbich, R. Monot, J. Buttet, and K. Kern. Controlled deposition of size-selected silver nanoclusters. *Science*, 274(5289):956–958, 1996. 30

[14] W. F. Brown Jr. Thermal fluctuations of a single-domain particle. *Physical Review*, 130(5):1677, 1963. 41

[15] P. Bruno. Tight-binding approach to the orbital magnetic moment and magnetocrystalline anisotropy of transition-metal monolayers. *Physical Review B*, 39(1):865–868, Jan. 1989. 60

[16] J. M. D. Coey. *Magnetism and Magnetic Materials*. Cambridge University Press, Mar. 2010. 64

[17] W. A. de Heer and P. Milani. Large ion volume time-of-flight mass spectrometer with position and velocity-sensitive detection capabilities for cluster beams. *Review of Scientific Instruments*, 62(3):670–677, 1991. 14

[18] E. de Hoffmann. *Mass Spectrometry*. John Wiley & Sons Ltd, Mar. 2007. 16

[19] J. L. Dormann, D. Fiorani, and E. Tronc. Magnetic relaxation in fineparticle systems. *Advances in Chemical Physics, Volume 98*, pages 283–494, 1997. 40

[20] D. Eastham, Y. Qiang, T. Maddock, J. Kraft, J. Schille, G. Thompson, and H. Haberland. Quenching of ferromagnetism in cobalt clusters embedded in copper. *Journal of Physics: Condensed Matter*, 9(37):L497, 1997. 60

[21] M. El Ouali. Development of an ion funnel and application to a cluster source. Technical report, ÉCOLE POLYTECHNIQUE FÉDÉRALE DE LAUSANNE, Feb. 2003. 30

[22] E. Ferrari, F. Da Silva, and M. Knobel. Influence of the distribution of magnetic moments on the magnetization and magnetoresistance in granular alloys. *Physical Review B*, 56(10):6086–6093, 1997. 98, 131

[23] A. Fert and I. Campbell. Electrical resistivity of ferromagnetic nickel and iron based alloys. *Journal of Physics F: Metal Physics*, 6(5):849, 1976. 94

[24] A. Fert and I. A. Campbell. Two-current conduction in nickel. *Physical Review Letters*, 1968. 94

[25] E. E. Fullerton and I. K. Schuller. The 2007 Nobel Prize in physics: magnetism and transport at the nanoscale. *ACS nano*, 1(5):384–389, 2007. 93

[26] L. Gan, R. D. Gomez, C. J. Powell, R. D. McMichael, P. J. Chen, and W. F. Egelhoff. Thin Al, Au, Cu, Ni, Fe, and Ta films as oxidation barriers for Co in air. *Journal of Applied Physics*, 93(10):8731, 2003. 30

[27] L. García, F. Bartolomé, J. Bartolomé, F. Luis, F. Petroff, C. Deranlot, F. Wilhelm, A. Rogalev, P. Bencok, and N. Brookes. Anisotropy enhancement in co granular multilayers by capping. In *Materials Science Forum*, volume 570, pages 1–9. Trans Tech Publ, 2008. 60

[28] W. Gil, D. Görlitz, M. Horisberger, and J. Kötzler. Magnetoresistance anisotropy of polycrystalline cobalt films: Geometrical-size and domain effects. *Physical Review B*, 72(13):134401, Oct. 2005. 93

[29] J. I. Gittleman, Y. Goldstein, and S. Bozowski. Magnetic properties of granular nickel films. *Physical Review B*, 5(9):3609, 1972. 96, 97

[30] J. H. Gross. *Mass Spectrometry*. Textbook. Springer, 2004. 16, 29

[31] R. Guirado-López. Magnetic anisotropy of fcc transition-metal clusters: Role of surface relaxation. *Physical Review B*, 63(17):174420, Apr. 2001. 60

[32] H. Haberland, M. Mall, M. Moseler, Y. Qiang, T. Reiners, and Y. Thurner. Filling of micron-sized contact holes with copper by energetic cluster impact. *Journal of Vacuum Science & Technology A: Vacuum, Surfaces, and Films*, 12(5):2925–2930, 1994. 8

[33] R. Henríquez, S. Cancino, A. Espinosa, M. Flores, T. Hoffmann, G. Kremer, J. G. Lisoni, L. Moraga, R. Morales, and S. Oyarzún. Electron grain boundary scattering and the resistivity of nanometric metallic structures. *Physical Review B*, 82(11):113409, 2010. 89, 92, 115

[34] R. Henríquez, L. Moraga, G. Kremer, M. Flores, A. Espinosa, and R. C. Munoz. Size effects in thin gold films: Discrimination between electron-surface and electron-grain boundary scattering by measuring the Hall effect at 4K. *Applied Physics Letters*, 102(5):051608, 2013. 89

[35] R. Henríquez, S. Oyarzún, M. Flores, M. A. Suárez, L. Moraga, G. Kremer, C. A. Gonzalez-Fuentes, M. Robles, and R. C. Munoz. Size effects on the Hall constant in thin gold films. *Journal of Applied Physics*, 108(12):123704, 2010. 91

[36] M. Hillenkamp, G. Di Domenicantonio, and C. Félix. Monodispersed metal clusters in solid matrices: A new experimental setup. *Review of Scientific Instruments*, 77:025104, 2006. 6

[37] A. Hillion. *Étude des propriétés magnétiques d'assemblées de nanoparticules de Co, FeRh et FeAu.* PhD thesis, Université Claude Bernard-Lyon I, 2012. 100, 105, 111, 112

[38] A. Hillion, A. Tamion, F. Tournus, J. Flament, M. Hillenkamp, E. Bonet, and V. Dupuis. Magnetic Interactions Effects on Magnetic Measurements for Nanoparticle Assemblies. *Magnetics, IEEE Transactions on*, 47(10):3154–3156, 2011. 98, 111

[39] A. Hillion, A. Tamion, F. Tournus, O. Gaier, and E. Bonet. Advanced magnetic anisotropy determination through isothermal remanent magnetization of nanoparticles. *Physical Review B*, 2013. 55

[40] M. Jamet, W. Wernsdorfer, C. Thirion, V. Dupuis, P. Mélinon, A. Pérez, and D. Mailly. Magnetic anisotropy in single clusters. *Physical Review B*, 69(2):024401, Jan. 2004. 59, 60, 74, 81, 82, 83

[41] M. Jamet, W. Wernsdorfer, C. Thirion, D. Mailly, V. Dupuis, P. Melinon, and A. Perez. Magnetic anisotropy of a single cobalt nanocluster. *Physical Review Letters*, 86(20):4676–4679, Jan. 2001. 56, 59, 60, 74, 82

[42] R. L. Johnston. *Atomic and molecular clusters.* Masters series in physics and astronomy. Taylor and Francis, London, 2002. 9

[43] P. E. Kelly, K. O'GRADY, P. I. Mayo, and R. W. Chantrell. Switching mechanisms in cobalt-phosphorus thin films. *Magnetics, IEEE Transactions on*, 25(5):3881–3883, 1989. 50, 51, 110

[44] T. Kingetsu and K. Sakai. Perpendicular magnetic anisotropy and structures of epitaxial Co/Ag and Co/Au metallic superlattices. *Journal of Applied Physics*, 73(11):7622, 1993. 60

[45] M. Knobel, W. C. Nunes, L. M. Socolovsky, E. De Biasi, J. M. Vargas, and J. C. Denardin. Superparamagnetism and other magnetic features in granular materials: a review on ideal and real systems. *Journal of nanoscience and nanotechnology*, 8(6):2836–2857, 2008. 40, 59, 97

[46] F. Luis, F. Bartolomé, F. Petroff, J. Bartolomé, L. M. García, C. Deranlot, H. Jaffrès, M. J. Martínez, P. Bencok, F. Wilhelm, A. Rogalev, and N. B. Brookes. Tuning the magnetic anisotropy of Co nanoparticles by metal capping. *Europhysics Letters (EPL)*, 76(1):142–148, Jan. 2007. 60

[47] R. Morel, A. Brenac, C. Portemont, T. Deutsch, and L. Notin. Magnetic anisotropy in icosahedral cobalt clusters. *Journal Of Magnetism And Magnetic Materials*, 308(2):296–304, Jan. 2007. 60, 84

[48] N. F. Mott. The Electrical Conductivity of Transition Metals. *Proceedings of the Royal Society A: Mathematical, Physical and Engineering Sciences*, 153(880):699–717, Feb. 1936. 93

[49] R. Munoz, J. García, R. Henríquez, A. Moncada, A. Espinosa, M. Robles, G. Kremer, L. Moraga, S. Cancino, J. Morales, A. Ramírez, S. Oyarzún, M. Suárez, D. Chen, E. Zumelzu, and C. Lizama. Size Effects under a Strong Magnetic Field: Hall Effect Induced by Electron-Surface Scattering on Thin Gold Films Deposited onto Mica Substrates under High Vacuum. *Physical Review Letters*, 96(20):206803, May 2006. 89, 92

[50] R. Munoz, R. Henríquez, J. García, A. Moncada, A. Espinosa, M. Robles, G. Kremer, L. Moraga, S. Cancino, J. Morales, A. Ramírez, S. Oyarzún, M. A. Suárez, D. Chen, E. Zumelzu, and C. Lizama. Size effects under a strong magnetic field: transverse magnetoresistance of thin gold films deposited on mica. *Journal of Physics Condensed Matter*, 18:3401–3408, 2006. 92

[51] N. Nagaosa, S. Onoda, A. H. Macdonald, and N. P. Ong. Anomalous Hall effect. *Reviews of modern physics*, 82(2):1539–1592, May 2010. 98

[52] L. Néel. Theory of magnetic viscosity of fine grained ferromagnetics with application to baked clays. *Ann. Geophys*, 5:99–136, 1949. 41

[53] Neel, Louis. L'approche à la saturation de la magnétostriction. *J. Phys. Radium*, 15(5):376–378, 1954. 60, 81

[54] J. A. Osborn. Demagnetizing factors of the general ellipsoid. *Physical Review*, 1945. 61, 79

[55] F. Parent, J. Tuaillon, L. Stern, V. Dupuis, B. Prevel, A. Perez, P. Melinon, G. Guiraud, R. Morel, A. Barthelemy, and A. Fert. Giant magnetoresistance in Co-Ag granular films prepared by low-energy cluster beam deposition. *Physical Review B*, 55(6):3683–3687, Jan. 1997. 98, 131

[56] G. Pastor, J. Dorantes-Dávila, S. Pick, and H. Dreyssé. Magnetic Anisotropy of 3d Transition-Metal Clusters. *Physical Review Letters*, 75(2):326–329, July 1995. 60

[57] A. Perez, V. Dupuis, J. Tuaillon Combes, L. Bardotti, B. Prevel, E. Bernstein, P. Mélinon, L. Favre, A. Hannour, and M. Jamet. Functionalized ClusterAssembled Magnetic Nanostructures for Applications to high IntegrationDensity Devices. *Advanced Engineering Materials*, 7(6):475–485, 2005. 99

[58] M. M. L. Plumer, J. Van Elk, and D. Weller. *The Physics of Ultrahigh-Density Magnetic Recording.*, volume 41. Springer, 2001. 59, 97

[59] D. Ralph and M. Stiles. Spin transfer torques. *Journal Of Magnetism And Magnetic Materials*, 320(7):1190–1216, 2008. 98

[60] S. Rubin, M. Holdenried, and H. Micklitz. Well-defined Co clusters embedded in an Ag matrix: A model system for the giant magnetoresistance in granular films. *The European Physical Journal B-Condensed Matter and Complex Systems*, 5(1):23–28, 1998. 98

[61] D. J. Sellmyer, M. Yu, and R. D. Kirby. Nanostructured magnetic films for extremely high density recording. *Nanostructured Materials*, 12(5-8):1021–1026, Jan. 1999. 59, 97

[62] R. Smith. Semiconductors. *Cambridge University Press, Chapter V*, 1961. 90

[63] J. Stöhr. Exploring the microscopic origin of magnetic anisotropies with x-ray magnetic circular dichroism (xmcd) spectroscopy. *Journal of Magnetism and Magnetic Materials*, 200(1):470–497, 1999. 60

[64] E. C. Stoner and E. Wohlfarth. A mechanism of magnetic hysteresis in heterogeneous alloys. *Philosophical Transactions of the Royal Society of London. Series A. Mathematical and Physical Sciences*, pages 599–642, 1948. 43

[65] A. Tamion, E. Bonet, F. Tournus, C. Raufast, A. Hillion, O. Gaier, and V. Dupuis. Efficient hysteresis loop simulations of nanoparticle assemblies beyond the uniaxial anisotropy. *Physical Review B*, 85(13):134430, Apr. 2012. 56

[66] A. Tamion, M. Hillenkamp, F. Tournus, E. Bonet, and V. Dupuis. Accurate determination of the magnetic anisotropy in cluster-assembled nanostructures. *Applied Physics Letters*, 95(6):062503, Aug. 2009. 52, 53, 54, 66

[67] A. Tamion, C. Raufast, M. Hillenkamp, E. Bonet, J. Jouanguy, B. Canut, E. Bernstein, O. Boisron, W. Wernsdorfer, and V. Dupuis. Magnetic anisotropy of embedded Co nanoparticles: Influence of the surrounding matrix. *Physical Review B*, 81(14):144403, Apr. 2010. 100

[68] C. Tannous and J. Gieraltowski. The Stoner-Wohlfarth model of ferromagnetism. *European Journal of Physics*, 29(3):475–487, Mar. 2008. 43

[69] W. Thomson. On the Electro-Dynamic Qualities of Metals:–Effects of Magnetization on the Electric Conductivity of Nickel and of Iron. *Proceedings of the Royal Society of London*, 8:546–550, 1856. 93

[70] F. Tournus and E. Bonet. Magnetic susceptibility curves of a nanoparticle assembly, I Theoretical model and analytical expressions for a single magnetic anisotropy energy. *Journal Of Magnetism And Magnetic Materials*, 323(9):1109–1117, May 2011. 41, 53

[71] F. Tournus and A. Tamion. Comment on "Determining magnetic nanoparticle size distributions from thermomagnetic measurements"[Appl. Phys. Lett. 96, 222506 (2010)]. *Applied Physics Letters*, 98(21):216102–216102–1, 2011. 53

[72] F. Tournus and A. Tamion. Magnetic susceptibility curves of a nanoparticle assembly II. Simulation and analysis of ZFC/FC curves in the case of a magnetic anisotropy energy distribution. *Journal Of Magnetism And Magnetic Materials*, 323(9):1118–1127, May 2011. 53

[73] N. A. Usov and J. M. Barandiarán. Magnetic nanoparticles with combined anisotropy. *Journal of Applied Physics*, 112(5):053915, 2012. 61

[74] J. van Vleck. On the Anisotropy of Cubic Ferromagnetic Crystals. *Physical Review*, 52(11):1178–1198, Dec. 1937. 59

[75] X. J. Wang, H. Zou, and Y. Ji. Spin transfer torque switching of cobalt nanoparticles. *Applied Physics Letters*, 93(16):162501, Jan. 2008. 98

[76] W. Wernsdorfer, D. Mailly, and A. Benoit. Single nanoparticle measurement techniques. *Journal of Applied Physics*, 87(9):5094–5096, 2000. 60

[77] W. C. Wiley and I. H. McLaren. Time-of-Flight Mass Spectrometer with Improved Resolution. *Review of Scientific Instruments*, 26(12):1150, 1955. 14

[78] J. L. WIZA. Microchannel plate detectors. *Nucl. Instrum. Methods*, 162(1-3):587–601, 1979. 16

[79] S. A. Wolf, D. D. Awschalom, R. A. Buhrman, J. M. Daughton, S. Von Molnar, M. L. Roukes, A. Y. Chtchelkanova, and D. M. Treger. Spintronics: A spin-based electronics vision for the future. *Science*, 294(5546):1488–1495, 2001. 97

[80] J. Q. Xiao, J. S. Jiang, and C. L. Chien. Giant magnetoresistance in nonmultilayer magnetic systems. *Physical Review Letters*, 68(25):3749–3752, 1992. 97

[81] Y. Xie and J. A. Blackman. Magnetic anisotropy of nanoscale cobalt particles. *Journal of Physics Condensed Matter*, 16(18):3163–3172, Apr. 2004. 60, 84

[82] R. Yanes, O. Chubykalo-Fesenko, H. Kachkachi, D. Garanin, R. Evans, and R. Chantrell. Effective anisotropies and energy barriers of magnetic nanoparticles with Néel surface anisotropy. *Physical Review B*, 76(6):064416, Aug. 2007. 60

[83] S. Zhang and P. Levy. Conductivity and magnetoresistance in magnetic granular films. *Journal of Applied Physics*, 73(10):5315–5319, Jan. 1993. 87, 97, 122, 132

[84] S. Zhang, P. M. Levy, and A. Fert. Conductivity and magnetoresistance of magnetic multilayered structures. *Physical Review B*, 45(15):8689, 1992. 122

[85] S. Zhang and L. PM. Conductivity Perpendicular to the Plane of Multilayered Structures. In *Journal of Applied Physics*, pages 4786–4788, 1991. 122

[86] J. M. Ziman. Electrons and phonons: the theory of transport phenomena in solids. *Oxford University Press, Chapter XII*, 1960. 90, 91